
Force sensing with nanowires

INAUGURALDISSERTATION

zur Erlangung der Würde eines Doktors der Philosophie

vorgelegt der
Philosophisch-Naturwissenschaftlichen Fakultät
der Universität Basel

von

Nicola Rossi

aus Sestri Levante, Italien

Basel, 2019

Original document stored on the publication server of the University of Basel edoc.unibas.ch

This work is licensed under a [Creative Commons Attribution-NonCommercial-NoDerivatives 4.0 International License](https://creativecommons.org/licenses/by-nc-nd/4.0/)



Genehmigt von der Philosophisch-Naturwissenschaftlichen Fakultät auf Antrag von

Prof. Dr. Martino Poggio
Fakultätsverantwortlicher

Prof. Dr. Adrian Bachtold
Korreferent

Basel, den 25.06.2019

Prof. Dr. Martin Spiess
Dekan der Fakultät

Contents

| | |
|--|-------------|
| Introduction | viii |
| 1 Force detection with nanowires | 1 |
| 1.1 Mechanics of nanowires | 1 |
| 1.1.1 Flexural vibration of a beam | 1 |
| Orthogonality of modes and normal equations of motion | 5 |
| 1.1.2 Mechanical polarizations | 8 |
| 1.2 Force Detection | 11 |
| 1.2.1 Mechanical susceptibility | 11 |
| Bi-dimensional sensing | 12 |
| 1.2.2 Thermal noise | 13 |
| 1.2.3 Force Sensitivity | 18 |
| 1.3 Light-nanowire interaction | 18 |
| 1.3.1 Scattering of an infinitely long cylinder | 19 |
| 1.4 Nanowires fabrication | 25 |
| 1.4.1 Self-catalyzed MBE grown GaAs nanowires | 26 |
| 2 Experimental setup | 28 |
| 2.1 Instrumentation | 28 |
| 2.2 Motion detection of a nanowire | 31 |
| 2.2.1 Fiber-based confocal reflection microscope | 31 |
| 2.2.2 Fiber-optic interferometer | 34 |
| 2.2.3 Displacement calibration and 2D angular mapping | 37 |
| 3 Vectorial scanning force microscopy using a nanowire sensor | 43 |
| 3.1 Introduction | 43 |
| 3.2 Nanowire sensor and setup | 44 |
| 3.3 Nanowire-sample interaction | 46 |
| 3.3.1 Bi-modal scanning probe microscopy | 46 |
| 3.3.2 Nanowire dynamics in a bi-dimensional force field | 48 |
| 3.4 Imaging of static in-plane force derivatives and dissipation | 51 |
| 3.5 Dynamic measurement of 2D force fields | 54 |
| 3.6 Coherent Two-Mode Dynamics | 57 |
| 3.7 Discussion and outlook | 61 |
| 4 Magnetic Force Sensing Using a Self-Assembled Nanowire | 62 |
| 4.1 Introduction | 62 |
| 4.2 GaAs nanowires with a ferromagnetic MnAs tip | 63 |
| 4.2.1 Magnetic properties of MnAs(0001)/GaAs(111) | 63 |
| 4.2.2 Mechanical properties | 66 |
| 4.3 Nanowire dynamic torque magnetometry | 68 |
| 4.3.1 Basic principles of dynamic cantilever magnetometry | 69 |

| | | |
|----------|---|------------|
| 4.3.2 | Magnetic energy and numerical simulations | 70 |
| | Analytical model | 70 |
| | Numerical model | 71 |
| 4.3.3 | MnAs tips DCM: experimental results and analysis | 72 |
| 4.4 | Dynamical current sensing | 77 |
| 4.4.1 | Current sensitivity | 79 |
| 4.5 | Discussion and outlooks | 81 |
| 5 | Conclusions and future directions | 83 |
| A | Low temperature nanowire microscope | 86 |
| B | NWs sample fabrication procedure | 88 |
| C | Micromagnetic simulations for NW magnetometry | 90 |
| D | Microwire's magnetic field | 92 |
| E | Sensitivity to different types of magnetic field sources | 93 |
| F | Magnetometry of GaAs NW with FIBbed MnAs tips | 96 |
| G | Room temperature NW MFM | 98 |
| | Bibliography | 100 |
| | Curriculum vitæ | 110 |
| | Acknowledgements | 112 |

List of Figures

| | | |
|------|---|----|
| 1 | Top-down vs. bottom-up scanning force sensors. | x |
| 1.1 | Singly-clamped beam in pure bending. | 2 |
| 1.2 | Flexural modes of vibration for a single-clamped beam. | 5 |
| 1.3 | Fundamental mode splitting for an asymmetric hexagonal NW. | 10 |
| 1.4 | Mechanical susceptibility | 12 |
| 1.5 | Power spectral density and autocorrelation of a resonator driven by Gaussian white noise. | 15 |
| 1.6 | Thermal noise spectral density of a GaAs NW | 17 |
| 1.7 | Scheme for the Mie scattering problem. | 20 |
| 1.8 | Mie scattering modes. | 21 |
| 1.9 | Scattering efficiencies of a transparent dielectric NW. | 23 |
| 1.10 | Effective scattering efficiency of a lossy dielectric NW | 24 |
| 1.11 | Angular scattering efficiency for a GaAs NW | 25 |
| 1.12 | VLS mechanism for self-catalyzed NWs growth | 26 |
| 2.1 | Schematic representation of the measurement setup. | 29 |
| 2.2 | Low temperature nanowire scanning probe microscope. | 30 |
| 2.3 | Fiber-based confocal reflection microscopy setup. | 32 |
| 2.4 | Optical microscope characterization at $\lambda = 1550$ nm | 33 |
| 2.5 | Scattered Gaussian beam by a nanowire | 35 |
| 2.6 | Wavelength/temperature cavity scan | 37 |
| 2.7 | Measurement vectors and displacement sensitivity maps | 38 |
| 2.8 | Tip displacement calibration | 39 |
| 2.9 | Static and dynamic optical gradient measurement | 40 |
| 2.10 | Angular displacement power map | 42 |
| 3.1 | Array of GaAs/AlGaAs core-shell nanowires. | 44 |
| 3.2 | Displacement noise spectrum of core/shell GaAs/AlGaAs NW1. | 45 |
| 3.3 | Displacement noise spectrum of core/shell GaAs/AlGaAs NW2. | 46 |
| 3.4 | 2D lateral force microscopy. | 47 |
| 3.5 | NW immersed in a tip-sample force field and eigenvectors rotation. | 49 |
| 3.6 | In-plane force gradients of tip-sample interaction. | 52 |
| 3.7 | Dissipation maps. | 53 |
| 3.8 | In-plane tip-sample force field. | 53 |
| 3.9 | Operating scheme for the dynamic measurement of 2D force fields. | 54 |
| 3.10 | Vector plots of electrostatic force fields. | 56 |
| 3.11 | Shear force gradient vs. gate voltage mapping | 58 |
| 3.12 | Vibrational modes evolution at an anti-crossing point. | 59 |
| 3.13 | Rabi oscillations. | 60 |
| 4.1 | Composition and crystal structure of MnAs-tipped nanowires. | 64 |
| 4.2 | MnAs/GaAs crystalline configurations and epitaxial relations. | 65 |

| | | |
|------|---|----|
| 4.3 | SEM micrographs of GaAs NWs with MnAs tip. | 66 |
| 4.4 | Displacement noise spectrum of a MnAs-tipped GaAs NW. | 67 |
| 4.5 | Sketch for NW magnetometry measurement and simulation | 71 |
| 4.6 | NW1 - MnAs tip magnetometry: zero-field vortex state. | 73 |
| 4.7 | NW2 - MnAs tip magnetometry: zero field in-plane dipole. | 75 |
| 4.8 | NW3 - MnAs tip magnetometry: anomalous hard axis tilt. | 76 |
| 4.9 | Sketch of the setup for dynamical current sensing | 78 |
| 4.10 | Characterization of NW2 as magnetic scanning probe. | 79 |
| 4.11 | NW2 sensitivity to a resonant current drive at distance $d_z = 250$ nm. | 80 |
| | | |
| A.1 | Photograph of the actual microscope. | 86 |
| A.2 | Zoom on the central sample region | 87 |
| | | |
| B.1 | Scanning NWs sample preparation under an optical microscope. | 88 |
| | | |
| C.1 | Geometry of MnAs tip's simulation parameters | 90 |
| | | |
| D.1 | Simulated magnetic stray field of the current carrying wire. | 92 |
| | | |
| E.1 | In-plane magnetic field gradient due to different sources | 94 |
| | | |
| F.1 | Dynamic torque magnetometry of a FIBbed MnAs tip. | 96 |
| | | |
| G.1 | Permalloy disks scanned with a magnetic-vortex tipped NW. | 98 |
| G.2 | Micromagnetic simulation of a MnAs tip over Py disk. | 99 |

List of Tables

| | | |
|-----|--|----|
| 1.1 | Solutions of the dispersive equation | 4 |
| 1.2 | Frequency split and aspect ratio statistics on measured NW samples . . | 10 |
| 4.1 | MnAs/GaAs(111) magnetic parameters. | 65 |
| C.1 | Angles giving the best fit to data for each NW. | 90 |

List of Abbreviations

| | |
|--------|---|
| AFM | Atomic Force Microscopy |
| UHV | Ultra High Vacuum |
| NW | NanoWire |
| CNT | Carbon NanoTube |
| AR | Aspect Ratio |
| RT | Room Temperature |
| MBE | Molecular Beam Epitaxy |
| CVD | Chemical Vapor Deposition |
| PSD | Power Spectral Density |
| FWHM | Full Width Half Maximum |
| SNR | Signal to Noise Ratio |
| BW | Resolution BandWidth |
| PM | Polarization Maintaining |
| NA | Numerical Aperture |
| MFD | Mode Field Diameter |
| PLL | Phase-Locked Loop |
| PID | Proportional Integral Derivative controller |
| SEM | Scanning Electron Microspe |
| MFM | Magnetic Force Microscopy |
| ZB | Zinc-Blende crystal structure |
| WZ | WurZite crystal structure |
| STEM | Scanning Transmission Electron Microscope |
| EDX | Energy Dispersive X-ray spectroscopy |
| DCM | Dynamic Cantilever Magnetometry |
| FIB | Focus Ion Beam |
| FEBCID | Focus Electron Beam Induced Deposition |

Introduction

A mechanical force transducer converts a force into a displacement. The simplest formulation of a proportional relation between force and displacement is represented by Hooke's law for an ideal spring, and it is extended to solid bodies by the theory of elasticity. However, the behavior of homogeneous beams with regular geometry can still be modeled as mass loaded spring system, and therefore as a simple harmonic oscillator, as long as it remains in the linear-elastic regime (i.e. small enough displacement). Depending on the mechanical oscillator design, its torsional or flexural modes can couple with great efficiency to external forces, offering a simple and effective interface for interacting and measuring forces of different physical nature.

Historically, the torsion pendulum became one of the most popular scientific instruments for the measurement of weak forces, in the late 18th century and throughout the following century. Such apparatus consists of a bar suspended from its middle by a thin fiber, which acts as a very weak torsion spring $\kappa = \omega_0^2 I$, where I is the moment of inertia and ω_0 is the pendulum's natural frequency. Any external force F , acting normally on the end of one bar's arm, produces a torque $\tau = Fl$, where $2l$ is the bar's length, and induces a pendulum's rotation by an angle θ , proportional to it by a factor κ . Taking advantage of the high force sensitivity of this technique, the first prominent experimental results were the definition of the inverse-square law of electrostatics by *C. A. Coulomb* [1], followed up by the first measurement of the gravity force between masses in a laboratory setup with a force sensitivity of ~ 100 nN, which allowed *H. Cavendish* to precisely estimate the gravitational constant [2].

Despite the pendulum was mainly used in the 'static' mode evaluating the displacement at equilibrium, the dynamics of such mass-spring harmonic oscillator were already considered to precisely derive the device's spring constant (i.e. the transduction factor from a force to a linear/angular displacement), by measuring the period of oscillation and the mass/inertia.

Only lately, starting with the measurement of radiation pressure by *E. F. Nichols* [3] at the beginning of the 20th century, the 'dynamic' force sensing mode was introduced, by studying the effects of the external force on the resonator's oscillation amplitude and frequency, when the system is on resonance rather than at the static equilibrium position. Faster oscillation frequencies obtained by reducing the resonator's mass (decreasing its size) allowed to average out and decouple the measurement from quasi-static sources of noise affecting the displacement's detection, while opening up a wide spectrum of possibilities for force modulation and detection schemes.

The invention of atomic force microscope (AFM) in 1986 by *G. Binnig*, *C.F. Quate* and *C. Gerber* [4] showed the first application of the concepts of mechanical force sensing to the framework of scanning probe microscopy. In AFM, a micro-machined cantilever with an 'atomically' sharp tip is driven on resonance and approached to a distance of few nanometers or less from the sample's surface. The tip interacts locally with the surface's local 'atomic' forces (i.e. Van der Waals and other type of electrostatic forces), modifying the cantilever's resonance frequency and oscillation amplitude. Thanks to the generality of its working principle, which does not

depend either on the sample's nature or on the operating conditions, this technique is nowadays one of the most powerful imaging tools with a broad spectrum of applications from biological samples in liquid to atomic lattices in ultra-high vacuum (UHV) environment. Great efforts have been devoted to push the spatial resolution to unprecedented levels, allowing to achieve subatomic resolution [5] and to image the chemical structure of a single molecule [6]. However, for such goals, the force sensitivity provided by conventional batch fabricated cantilevers or even by quartz-tuning forks is usually enough to detect the strong short-range forces, which dominate at sub-nanometric tip-sample separation.

Nevertheless, sensitivity to small forces is crucial for other applications. These range from mass detection [7], to cantilever magnetometry [8, 9], to observation of fundamental phenomena such as persistent current in normal metal rings [10], to scanning measurements of friction forces [11, 12] and force-detected magnetic resonance (MRFM) [13, 14]. In the last 20 years, improvements in micro- and nano-fabrication and in optical [15] and electromechanical detection of motion, allowed for refined designs and size (mass) reduction of mechanical resonators leading to a dramatic increase of their force sensitivity [16], down to the mechanical detection of a single electron's spin resonance [13] and nanoscale magnetic resonance imaging [14], with ultra-soft silicon cantilevers (similar to Fig. 1(b)).

More recently, with the rise of nano-technologies, this push towards higher sensitivity has generated interest in using even smaller mechanical forces transducers, especially those made by 'bottom-up' techniques. These very light nanometer-scale structures such as nanowires (NWs) and carbon nanotubes (CNTs) displayed unprecedented mechanical properties: CNTs resonators in doubly-clamped geometry reached a record force sensitivity in the order of $1 \text{ zN}/\sqrt{\text{Hz}}$ ¹ [17, 18] enabling mass detection with a resolution of 1.7 yg ² corresponding to the mass of one proton [19].

The trend towards decreasing the size of mechanical transducers is based on fundamental principles. For a thermally limited mechanical force transducer, the fluctuation-dissipation theorem implies that the minimum detectable force is limited by the force noise spectral density $S_F = 4k_B T \Gamma$ associated with the Brownian fluctuations of the oscillator's position at finite temperatures, where k_B is the Boltzmann constant, T is the resonator's temperature, and Γ its mechanical dissipation (friction coefficient). In particular, the transducer's force sensitivity, intended for a nominal measurement bandwidth of 1 Hz (not indicated), is given by

$$F_{min} = \sqrt{4k_B T \Gamma} = \sqrt{4k_B T \frac{M\omega_0}{Q}}$$

where $\Gamma = M\omega_0/Q$ is expressed in terms of the resonator's parameters: the motional mass M , the angular resonance frequency ω_0 , and the quality factor Q . In practice, this means that at a given temperature, a well-designed cantilever force transducer must simultaneously have low $M\omega_0$ and large Q .

For a cylindrical cantilever (e.g. a NW) – of length l and diameter d – we can apply Euler-Bernoulli beam theory to relate its dimensions to force sensitivity, finding that $M\omega_0 \propto d^3/l$. Moreover, for sensitive transducers, experiments show that Q is limited by surface-related losses [20], which lead to a linear decrease of Q with increasing

¹ 1 zeptoNewton = 10^{-21} N

² 1 yoctogram = $10^{-24} \text{ g} = 10^{-27} \text{ kg}$

surface-to-volume ratio, i.e. $Q \propto d$. As a result, we see that $\Gamma \propto d^2/l$, meaning that long and thin cantilevers should be the most sensitive. Furthermore, if we fix the aspect ratio (AR) and scale each dimension of the cantilever uniformly by a factor α , we find that $\Gamma \propto \alpha$ and therefore $F_{min} \propto \sqrt{\alpha}$. This implies that given a constant AR, smaller structures will be sensitive to smaller forces.

High AR and small mass are peculiar features of ‘bottom-up’ cantilevers – reviewed in Fig. 1 – and they both contribute to enhance the force sensitivity. However, a reduction of the cantilever’s size guaranties also higher mechanical resonance frequencies ($\omega_0 \propto d/l^2 \propto 1/\alpha$), which are attractive for force transducers, since they allow for the measurement of fast dynamics and they decouple the sensor from common sources of noise. A prominent example is the additional noise experienced by a cantilever as its tip approaches a surface [27, 28]. This so-called *non-contact friction* is largely due to electronic fluctuators on the surface and typically has a $1/f$ -like frequency dependence. This effect is crucial in scanning probe applications, since the total dissipation Γ increases as the tip-sample distance is reduced, degrading the measurement force resolution. In this context, the use of silicon NWs – in Fig. 1(d) – by *Nichol et al.* [29] has shown not only ultralow intrinsic dissipation down to 2×10^{-15} kg/s, unaltered within 10 nm tip-sample spacing, but also a reduced interaction with the surface yielding a factor of 80 less surface dissipation and a factor of 250 less total dissipation compared to audio frequency cantilevers (similar to Fig. 1(b)) under similar conditions.

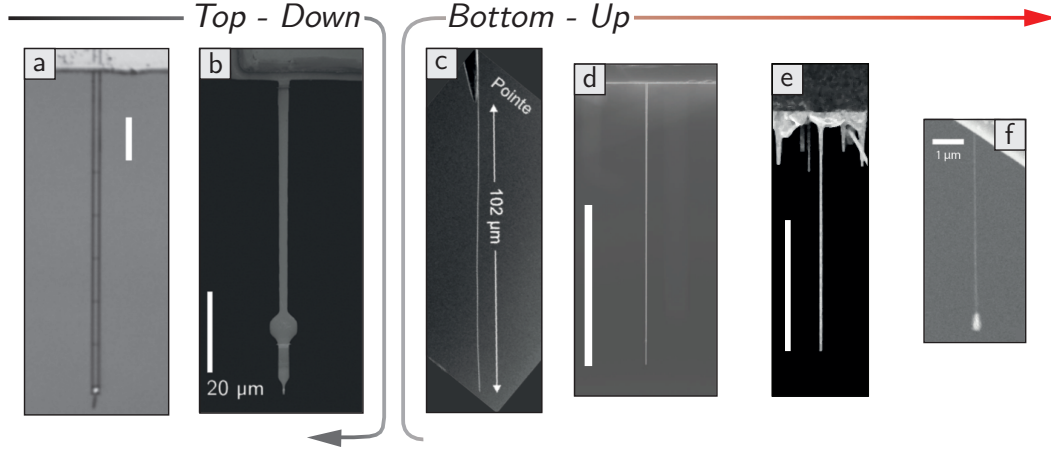


FIGURE 1 | **Top-down vs. bottom-up scanning force sensors.**

(a) Diamond ‘nanoladder’ as an improved design for rectangular cantilevers, with 2 orders of magnitude mass and stiffness reduction ($M \sim 5$ pg), thanks to the high AR given by the two parallel beams with $d = 200$ nm. $F_{min} = 13$ aN/ $\sqrt{\text{Hz}}$ at RT [21]. Scale bar 20 μm . (b) ‘State-of-the-art’ ultrasensitive silicon cantilever. $F_{min} = 3.8$ aN/ $\sqrt{\text{Hz}}$ at 3 K [20]. (c) CVD grown SiC NW mounted on a sharp W support. The larger motional mass is compensated by a very high AR $= l/d \sim 850$. $F_{min} = 30$ aN/ $\sqrt{\text{Hz}}$ at RT [22, 23]. (d) Au-catalyzed VLS grown Si NW. $F_{min} \sim 10$ aN/ $\sqrt{\text{Hz}}$ at RT [24]. Scale bar 10 μm . (e) MBE grown self-catalyzed GaAs NW [25]. $M = 780$ fg and $F_{min} \sim 3.5$ aN/ $\sqrt{\text{Hz}}$ at 4.2 K. Scale bar 10 μm . (f) Singly clamped CNT ($d \sim 2$ nm) with Pt nanoparticle at the tip for optical motion detection. Such devices feature extreme AR $\gtrsim 2000$, while $M = 7.9 \times 10^{-19}$ kg is for 80% given by the Pt scatterer. $F_{min} = 0.7$ aN/ $\sqrt{\text{Hz}}$ at RT [26].

Hence, in order to simultaneously maximize ω_0 and minimize F_{min} , the entire structure should be scaled down. This necessity for further reduction in cantilever size has positioned ‘bottom-up’ techniques as the fabrication methods of the future.

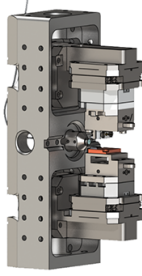
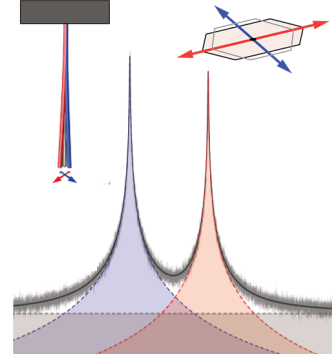
In this dissertation, we aim to explore the potential of ‘bottom-up’ fabricated devices, such as semiconductor NWs, as scanning force sensors. Their singly clamped structure makes them ‘easy’ to scan over a sample in the pendulum geometry enabling the measurement of very weak lateral force gradients, thanks to their remarkable mechanical properties [30].

Notably, NWs present spatially nearly degenerate flexural modes, due to their quasi-symmetrical cross section, resulting into the polarization of each mode along two orthogonal oscillation directions, with minimal frequency splitting and almost equal mechanical characteristics. This peculiar ‘bimodal’ feature, unlike multifrequency force microscopy with conventional AFM cantilevers [31], enables the detection of in-plane forces along two orthogonal oscillation directions and gives access to the full vectorial character of force fields. The rotation of the two modes’ orientation in a Si NW (similar to Fig. 1(d)) has been initially studied by *Gil-Santos et al.* [32] to radially locate the position of a carbon adsorbate for mass detection applications. Lately, in the context of force sensing, a formal description of the evolution of the two modes in an external force field has been derived by *Gloppe et al.* [22] and used to measure the bi-dimensional vectorial map of an optical force field interacting with a SiC NW (Fig. 1(c)). In Chapter 3, we demonstrate the integration of a self-assembled NW vectorial force sensor in a cryogenic scanning probe microscope setup with fiber-based interferometric optical motion detection. By monitoring the frequency shift and direction of oscillation of both modes as we scan above the sample’s surface, we construct a map of all spatial static tip-sample force derivatives in the plane. Moreover, we dynamically probe electric force fields distinguishing between forces arising from the NW charge and polarizability [33]. Similar measurements of in-plane electrostatic force fields have been reported by *de Lepinay et al.* with a SiC NW [23].

Our research is focussed on *as-grown* self-catalyzed NWs, produced with molecular beam epitaxy (MBE) techniques, which ensure the highest growth control for almost defect-free structures on the atomic-scale with perfectly terminated surfaces. Furthermore, epitaxial growth allows the realization of NWs from a number of materials as well as their combination to form heterostructures, offering the possibility of functionalizing the mechanical resonator ‘in-situ’, for example with quantum emitters [34] or with magnetic crystalline tips [35]. The scanning magnetic force sensor based on a magnet-tipped GaAs NW, presented in Chapter 4, clearly exemplifies the potential of such growth methods. In addition, the high mechanical force sensitivity of these compact probes, makes possible the characterization of the nano-metric tip’s magnetic properties via dynamic torque magnetometry as well as the resonant detection of electric currents with a resolution of $63 \text{ nA}/\sqrt{\text{Hz}}$ [25].

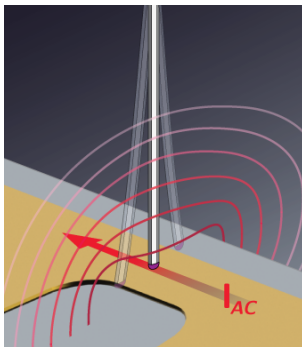
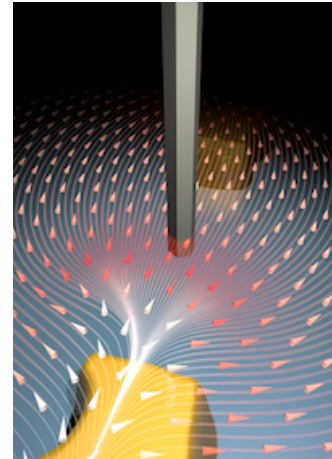
Thesis Outline

Chapter 1 overviews general background notions in the context of mechanical force detection using NWs as sensors. Starting by deriving the normal equations of motion for the flexural modes, the origin of their spacial orthogonal polarization is discussed in the context thermal noise limited force sensitivity. Then, the Mie scattering theory, underlying the optical motion detection of sub-wavelength cantilevers, is briefly presented. Finally, the growth technique for the NWs used in our experiments is concisely illustrated.



Chapter 2 describes the main functional parts and instrumentation constituting our scanning NW system. In particular, are shown the main capabilities of the fiber-based confocal microscope and interferometer, adopted for the motion detection of the NW. Principal techniques for displacement calibration and 2D motion mapping of the NW are also introduced.

Chapter 3 reports on the use of an individual as-grown NW to realize a vectorial scanning force microscopy over a patterned sample. By monitoring the thermally driven vibrations of the NW's fundamental modes, the static tip-sample force derivatives are mapped in the 2D scanning plane. Moreover, electrostatic tip-sample interactions are dynamically probed by measuring the NW's response to a driving force generated by an AC voltage on the sample's patterned electrodes, revealing the distinct contributions of NW's spurious surface charge and polarizability. In conclusion, such electrostatic interactions are exploited to strongly couple the NW's mechanical modes and to study their coherent dynamic.



In **Chapter 4** we demonstrate the use of as-grown NWs with crystalline magnetic tips as a magnetic sensor for scanning probe applications. Taking advantage of the excellent force sensitivity, the magnetic properties of such tips are studied via dynamic torque magnetometry and precisely fitted by micro-magnetic simulations, showing vortex and dipole-like configurations. Finally, we perform dynamic measurements over a patterned current-carrying wire, characterizing their behavior as current sensors and estimating their sensitivity.

Chapter 5, in conclusion, summarizes the main results presented in this thesis, giving an outlook on possible future developments and challenges, inspired by the reported experiments.

Chapter 1

Force detection with nanowires

This chapter aims to provide a general background of theoretical notions and methods involved in the experiments presented later on in this thesis. In the main framework of force detection using a nanowire (NW) as mechanical resonator, we first provide an analytical model for vibrations of singly-clamped beams, deriving the normal equations of motion to model the NW's dynamics and introducing their bi-dimensional character. We discuss the main limitation to mechanical force sensing and their origin. Thereafter, the light-nanowire interaction, which allows the optical detection of NWs, is presented. Finally, we briefly describe the fabrication method of the GaAs NWs used in our force sensing applications.

1.1 Mechanics of nanowires

In this thesis we will focus only on the flexural (transverse) vibrational modes, and specifically on the *fundamental transverse mode*, which is the mechanical mode with the lowest frequency and stiffness, ideal for force sensing applications. In fact, a NW is highly sensitive to the lateral components of a force, specially when on resonance. In beams with high aspect ratio, resonances of bending modes are much more accessible and force sensitive than the other mechanical modes. Specifically, torsional modes and longitudinal (axial or 'breathing') modes related to axial forces causing a compression/extension of the NW.

1.1.1 Flexural vibration of a beam

The mechanics and governing equation of a NW in pure bending are accurately described by the Euler-Bernoulli beam theory, formulated in the mid-18th century. Also known as thin beam theory, it is applicable to beams for which the length L is much larger than the depth (at least by a factor 10) and for small deflections compared to the latter. Under these conditions, the following assumptions are valid and simplify the physical description:

1. the rotation of cross sections of the beam is negligible in relation to their translation (i.e. the effects of the rotatory inertia are neglected compared with those of the linear inertia);
2. the angular distortion due to shear is considered insignificant compared to the bending deformation. The rotation is such that the cross-sections do not deform and remain orthogonal to the center axis (pure bending). Hence, shear force is only produced by the bending moment.

Constitutive and kinematical relations By choosing a proper coordinate system, it is possible to reduce the problem of a three-dimensional body under bending

to the a 1-D representation. The origin of the reference has to be placed at the center of mass of the cross-section¹ with the so-called *neutral axis* being orthogonal to it; in this way, a normal force N causes only strain² and no curvature (i.e. no moment). The stress applied to the side of the structure causes a linear variation of the axial strain ϵ_{zz} , which is statically equivalent to a moment and it is null at the neutral axis. The normal stress acting on a cross-section is in turn equivalent to a resultant normal force N along z and a moment M in the xy -plane [36]. Moreover, by arbitrarily orienting the xy reference axes on the cross-section, the *constitutive equation for bending* relates the moment M to the beam's curvature κ via the bending stiffness tensor as:

$$\begin{bmatrix} M_x \\ M_y \end{bmatrix} = - \begin{bmatrix} E_Y I_x & E_Y I_{xy} \\ E_Y I_{yx} & E_Y I_y \end{bmatrix} \begin{bmatrix} \kappa_x \\ \kappa_y \end{bmatrix} \quad (1.1)$$

where E_Y is Young's elastic modulus for the beam, I_x and I_y are the cross-sectional area moment of inertia³ and $I_{xy} = I_{yx}$ is the product moment of area⁴. For any geometry, it is possible to diagonalize the system and obtain two directions for x and y which are *principal axes* of the second moment of area and in respect of which the bending moments are fully uncoupled.

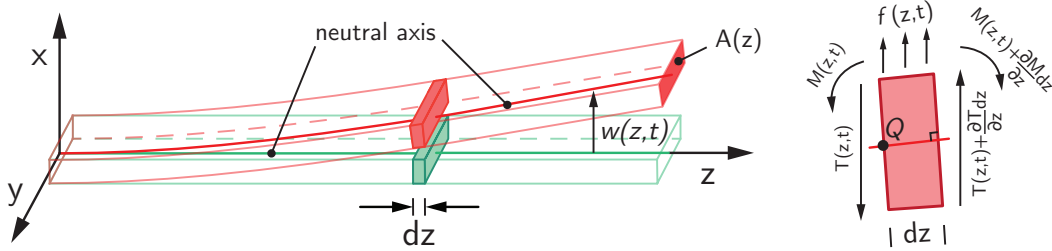


FIGURE 1.1 | **Singly-clamped beam in pure bending.**

On the left: a beam of length L and cross-sectional area $A(z) \ll L^2$. It is oriented along its principal axes x and y with the neutral axis coincident with the z -axis, at rest (in green). In red, bent beam under an homogeneous load along x , with displacement amplitude $w(z, t) \ll L$. On the right: a force and momentum balance for an infinitesimal section $dz \times A(z)$ at the point Q on the neutral axis.

With a beam in such coordinate system sketched in Fig. 1.1, we derive the beam equation for a bending moment M_y along the y -axis causing a transverse displacement $w(z, t)$ of the neutral axis in the x direction.

For pure bending we just have

$$M_y(z, t) = -E_Y I_y \kappa_y \simeq -E_Y I_y(z) \frac{\partial^2 w(z, t)}{\partial z^2} \quad (1.2)$$

where the curvature κ_y can be approximated by the second derivative of the displacement for small and smooth deflections.

¹ $(x_0, y_0) = \frac{1}{\int_A dA} (\int_A x dA, \int_A y dA)$

² $N = E_Y A \epsilon_{zz}$

³ $I_x = \int_A y^2 dA, I_y = \int_A x^2 dA$

⁴ $I_{xy} = I_{yx} = \int_A xy dA$

It is intuitive to derive the equation of motion through the expression of the local equilibrium in terms of the bending and shear resultants $M(z, t)$ and $T(z, t)$, respectively, on an infinitesimal beam's segment subjected to a distributed vertical load $f(z, t)$.

In the limit of $dz \rightarrow 0$, the moment balance – neglecting rotatory inertia under Bernoulli's beam assumptions – gives

$$T(z, t) = -\frac{\partial M_y(z, t)}{\partial z}, \quad (1.3)$$

while the transverse force balance has to be equal to the element's inertial force gives $f(z, t) - \partial T(z, t)/\partial z = \rho A(z)\ddot{w}(z, t)$. The latter, by means of Eqs. (1.2) and (1.3), is expressed in terms of the displacement and applied load

$$\rho A(z)\frac{\partial^2 w(z, t)}{\partial t^2} + \frac{\partial^2}{\partial z^2} \left[E_Y I_y(z) \frac{\partial^2 w(z, t)}{\partial z^2} \right] = f(z, t) \quad (1.4)$$

where $\rho A(z)$ is mass per unit length. The beam's density ρ as well as the Young's modulus E_Y are assumed constant under the hypothesis of homogeneous beam.

Free vibration of the beam To calculate the characteristic modes of vibration of the beam, we need to study the free evolution of the system in absence of an applied external force, i.e. $f(z, t) = 0$. Assuming that the cross-section shape and area $A(z)$ remain constant over the beam length, also the bending stiffness $E_Y I_y$ will be constant and the equation of motion reduces to

$$\rho A \frac{\partial^2 w(z, t)}{\partial t^2} + E_Y I_y \frac{\partial^4 w(z, t)}{\partial z^4} = 0 \quad (1.5)$$

This equation can be solved by separation of variables using a Fourier decomposition of the displacement $w(z, t)$ into the sum of harmonic vibrations:

$$w(z, t) = \sum_{n=0}^{\infty} \mathbb{R}(w_n(z) e^{-i\omega_n t}) \quad (1.6)$$

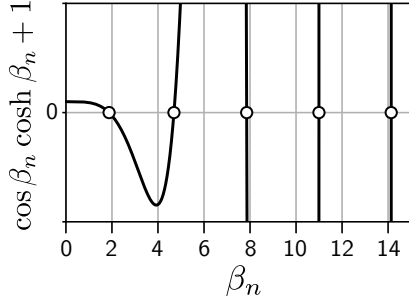
where $\mathbb{R}(\dots)$ refers to the real part of the quantity in parentheses, $w_n(z)$ describes the shape and amplitude of the bending and $e^{-i\omega_n t}$ accounts for the oscillatory temporal evolution. Being NWs highly under-damped resonators, the motion damping term $\Gamma_n \dot{w}$ is neglected for the moment. The separation ansatz leads to a spatial equation in the form of

$$\frac{d^4 w_n(z)}{dz^4} - \frac{\beta_n^4}{L^4} w_n(z) = 0 \quad \text{with} \quad \beta_n = L \left(\omega_n^2 \frac{\rho A}{E_Y I_y} \right)^{\frac{1}{4}} \quad (1.7)$$

which admits an infinite number of solutions $w_n(z)$ (i.e. n^{th} flexural mode), each of them vibrating at a distinct eigenfrequency ω_n of the system. We expressed the parameter β_n as a dimensionless quantity to simplify and clarify the calculations. The dispersion relation for β_n in equation (1.7), relates the geometrical and structural properties of the cantilever to its eigenfrequencies, which can be calculated as:

$$f_n = \frac{\omega_n}{2\pi} = \frac{1}{2\pi} \frac{\beta_n^2}{L^2} \sqrt{\frac{E_Y I_y}{\rho A}} \quad (1.8)$$

| Mode n | β_n | ω_n/ω_0 |
|------------|----------------|----------------------------|
| 0 | 1.875 | 1 |
| 1 | 4.694 | 6.267 |
| 2 | 7.855 | 17.547 |
| 3 | 10.996 | 34.386 |
| $n \geq 3$ | $(n + 1/2)\pi$ | $[(n + 1/2)\pi/\beta_0]^2$ |


TABLE 1.1 | **Solutions of the dispersive equation**

Values of β_n and of the eigenfrequencies normalized to the fundamental ω_0 . For $n \geq 3$, the asymptotic values can be expressed in closed form [37].

The lowest frequency f_0 is referred to as the *fundamental frequency*.

The differential equation (1.7) has a general solution expressed as:

$$w_n(z) = A_n \cos\left(\beta_n \frac{z}{L}\right) + B_n \cosh\left(\beta_n \frac{z}{L}\right) + C_n \sin\left(\beta_n \frac{z}{L}\right) + D_n \sinh\left(\beta_n \frac{z}{L}\right) \quad (1.9)$$

with β_n and 3 out of the 4 coefficients (A_n, B_n, C_n, D_n) defined through the boundary conditions of the physical problem, up to an arbitrary scaling factor of the eigenfunction's amplitude.

In our case, the NW is fixed at one end ($z = 0$) and free to vibrate at the other ($z = L$). This cantilever configuration implies that the deflection and slope must vanish at $z = 0$, while at the free end ($z = L$) the bending moment and shear force must be zero. That is, respectively:

$$w_n(0) = 0, \quad \left. \frac{dw_n}{dz} \right|_{z=0} = 0, \quad E_Y I_y \left. \frac{d^2 w_n}{dz^2} \right|_{z=L} = 0, \quad \left. \frac{d}{dz} \left[E_Y I_y \frac{d^2 w_n}{dz^2} \right] \right|_{z=L} = 0 \quad (1.10)$$

Applying these mathematical constraints to equation (1.9), allows to define the values of (A_n, B_n, C_n, D_n) up to one global parameter and to obtain the characteristic equation for the single-camped beam problem:

$$\cos \beta_n \cosh \beta_n + 1 = 0 \quad (1.11)$$

The infinite countable set of roots (i.e. eigenvalues) of the transcendental expression (1.11) are summarized in Table (1.1). Each root β_n is associated to the mode shape $w_n(z)$ of the n^{th} flexural mode, which is solution of the spatial equation (1.9) and is determined to be

$$w_n(z) = \frac{1}{K_n} \left\{ (\cos \beta_n + \cosh \beta_n) \left[\sin\left(\beta_n \frac{z}{L}\right) - \sinh\left(\beta_n \frac{z}{L}\right) \right] - (\sin \beta_n + \sinh \beta_n) \left[\cos\left(\beta_n \frac{z}{L}\right) - \cosh\left(\beta_n \frac{z}{L}\right) \right] \right\} \quad (1.12)$$

Following a common form of normalization [36, 37], we choose solutions $u_n(z)$ with $K_n = 2(\sin \beta_n \cosh \beta_n - \cos \beta_n \sinh \beta_n)$ in order to ensure the condition $|w_n(z)|_{\max} = 1$, which for a cantilever corresponds to $w_n(L) = 1$. Such normalized vibration profiles $u_n(z)$ are dimensionless and just describe the mode's shape, leaving the amplitude information (and physical unit of distance) to the time-dependent part of the general

solution. In Fig. 1.2 are shown the mode shapes correspondent to the first five flexural modes.

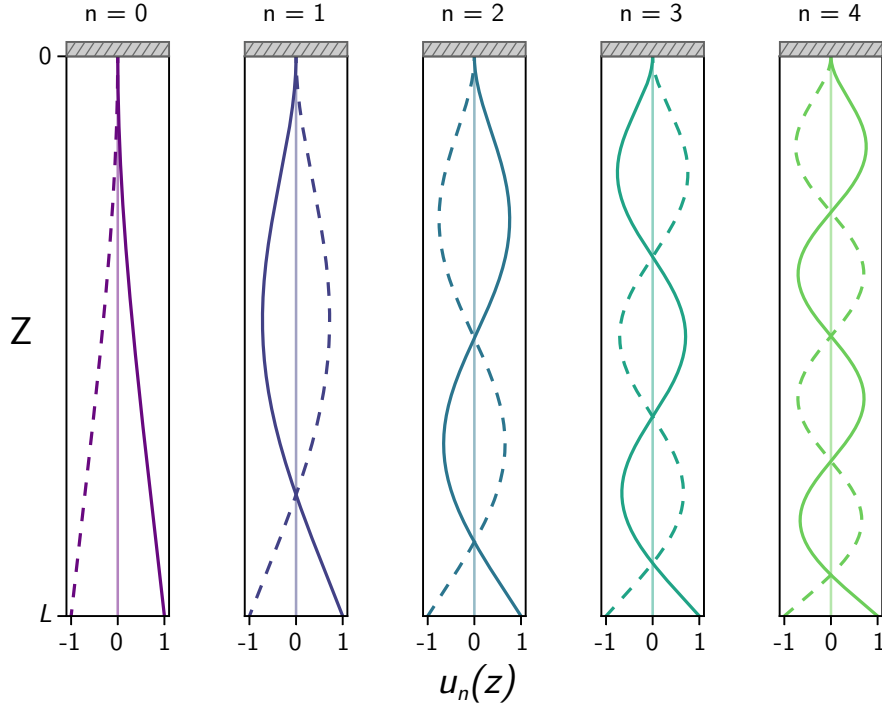


FIGURE 1.2 | **Flexural modes of vibration for a single-clamped beam.** Normalized vibrational profiles $u_n(z)$ for the first five flexural modes of a singly-clamped beam. The curves are described by Eq.(1.12).

Orthogonality of modes and normal equations of motion

The eigenvalue problem for beams under bending can be written in compact form by introducing two linear differential operators; specifically: the inertial operator $\mathfrak{m} = \rho A(z)$ and the stiffness operator $\mathfrak{k} = \frac{\partial^2}{\partial z^2} E_Y I_y(z) \frac{\partial^2}{\partial z^2}$. In doing so, equation (1.5) resembles the expression describing lumped-mass systems, where each natural frequency ω_n and modal function u_n satisfies the relation

$$(\mathfrak{k} - \omega_n^2 \mathfrak{m})u_n = 0 \quad (1.13)$$

By introducing the scalar product defined for continuous functions on $[0, L]$ ⁵, it is possible to demonstrate that the natural modes $u_n(z)$ are mutually orthogonal⁶ [38, 39]. In particular, the orthogonality relations are carried out in terms of the weighted inner product with respect to the inertial operator \mathfrak{m} :

$$\langle u_n, u_p \rangle_{\mathfrak{m}} = \int_0^L \rho A(z) u_n(z) u_p(z) dz = M_n \delta_{np} \quad (1.14)$$

⁵ $\langle u_n, u_p \rangle = \int_0^L u_n(z) u_p(z) dz$

⁶but not orthonormal since $\langle u_n, u_p \rangle = \frac{L}{4}$

where δ_{np} is the Kronecker delta⁷ and $M_n = \int_0^L \rho A(z) u_n^2(z) dz$ is the generalized mass of the n^{th} mode. A dual expression for orthogonality can be derived respect to the stiffness operator \mathbb{k} :

$$\langle u_n, u_p \rangle_{\mathbb{k}} = \int_0^L \frac{d^2}{dz^2} \left[E_Y I_y(z) \frac{d^2 u_n(z)}{dz^2} \right] u_p(z) dz = M_n \omega_n^2 \delta_{np} \quad (1.15)$$

Since the mutually orthogonal and complete set of modal functions $\{u_n\}$ is linearly independent, any transverse vibration of the beam $w(z, t)$, which satisfies the boundary conditions, can be represented as a linear combination of these functions. That is the convergent series

$$w(z, t) = \sum_{n=0}^{\infty} u_n(z) r_n(t) \quad (1.16)$$

where $r_n(t) = a_n \sin(\omega_n t + \phi_n)$ are time-dependent harmonic functions at the natural frequencies of the beam⁸, with amplitude a_n and phase ϕ_n determined by the initial conditions on $w(z, 0)$ and $\dot{w}(z, 0)$. Note that, as a consequence of the expansion theorem, any deformation $w(z)$ of the cantilever is represented as a weighted combination of the normalized modes of the unforced cantilever $w(z) = \sum_{n=0}^{\infty} a_n u_n(z)$.

These are key concepts that allow to decompose the continuous vibrational problem into an infinite system of equations of motion with single degree of freedom, whose displacements correspond to the modal coordinates $r_n(t)$ [36]. Replacing the expression (1.16) into the generic governing equation (1.4), multiplying both sides by u_p and integrating over $[0, L]$, then results in the identity

$$\int_0^L \sum_{n=0}^{\infty} \left\{ \ddot{r}_n(t) \rho A u_n u_p + r_n(t) \frac{d^2}{dz^2} \left[E_Y I_y \frac{d^2 u_n}{dz^2} \right] u_p \right\} dz = \int_0^L u_p f(z, t) dz \quad (1.17)$$

Interchanging the order of integration and summation and applying the orthogonality relations (1.14) and (1.15) reduces equation (1.17) to a set of uncoupled differential equations in $r_n(t)$ called *normal equations of motion*:

$$M_n \ddot{r}_n(t) + M_n \omega_n^2 r_n(t) = F_n(t) \quad \text{for } n = 0, \dots, \infty \quad (1.18)$$

Each equation describes the amplitude of an individual mode and is equivalent to the one of a mass-spring lumped system. To each degree of freedom corresponds a *modal mass* $M_n = \langle u_n(z), u_n(z) \rangle_{\text{m}}$ and a *modal stiffness* $k_n = M_n \omega_n^2 = \langle u_n(z), u_n(z) \rangle_{\mathbb{k}}$. The *modal forces* $F_n(t) = \langle u_n(z), f(z, t) \rangle$ (i.e. the forces acting on the modal masses M_n) account for the portion of the applied force distributed to each mode.

Effective mass The *modal mass* or *effective mass* M_n is a fundamental quantity in describing the dynamical behavior of a continuum system with position-dependent inertia. In fact, each volume element of the beam reacts to a transverse load with increasing inertia the closest it is to the free-end point.

By virtue of our normalization condition $|u_n(L)| = 1$, the equations of motion (1.18) describe the time evolution of the displacement $r_n(t)$ at the tip and the

$${}^7 \delta_{np} := \begin{cases} 1 & \text{for } n = p \\ 0 & \text{for } n \neq p \end{cases}$$

⁸Can be seen as a generalized Fourier Series

effective mass are measured at the position of maximum displacement $z = L$. From equation (1.14) it follows that:

$$\frac{M_n}{M_{tot}} = \frac{1}{L} \int_0^L |u_n(z)|^2 dz = \frac{1}{4} \quad \forall n \quad (1.19)$$

Given the total potential energy of the mode $\mathcal{E}_P = \frac{1}{2} M_n \omega_n^2 |r_n(t)|^2$, it is important to underline that, if the displacement is probed at another position $z = z_0 \neq L$, the correspondent effective mass value renormalized by a factor $|u_n(z_0)|^2$ as [37]:

$$M_n(z_0) = \frac{M_n}{|u_n(z_0)|^2} \geq \frac{1}{4} \quad \text{for } 0 \leq z_0 \leq L \quad (1.20)$$

This follows from the fact that, for the same energy, the modal displacement scales as $r_n(z_0, t) = r_n(t) u_n(z_0)$.

Since the modal mass is constant and equal to 1/4 of the total mass – independently of the mode n –, in the following will be indicated as M .

Mechanical dissipation The equations of motion in (1.18) describe the ideal case of a non-dissipative perfectly elastic cantilever. However, real resonators are non conservative systems and dissipate energy with consequent damping of their motion.

A common framework to introduce dissipation is to account for the internal damping of a viscoelastic material [40, 41]. Using Hooke's law for solids, the strain ϵ is linearly related to the applied stress σ via the Young modulus $E_Y = \frac{\sigma}{\epsilon}$. While for elastic material (i.e. conservative case) E_Y is constant and real, in the viscoelastic case the relation depends on the excitation's frequency and the strain is phase-lagged with respect to stress as

$$E_Y(\omega) = E_{Y,eff}(\omega)[1 + i\phi(\omega)] \quad (1.21)$$

The loss angle $\phi(\omega)$ represents a rate of energy loss meaning that a fraction $2\pi\phi$ of energy stored in the oscillatory motion \mathcal{E}_{tot} is being dissipated during each cycle. $E_{Y,eff}$ and ϕ are assumed to be constant over the frequency range of interest $\omega \geq \omega_0$. We also introduce the quality factor Q as a figure of merit of the resonator according to its standard definition:

$$Q^{-1} = \phi = \frac{\Delta \mathcal{E}_{loss}}{2\pi \mathcal{E}_{tot}} = \frac{\text{Im}(E_Y)}{\text{Re}(E_Y)} \quad (1.22)$$

By replacing the complex Young modulus (1.21) in equation (1.7), the eigenfrequencies ω_n of the system are determined by a complex-valued dispersion relation for β_n . For good resonators such NW cantilevers, operating in the low dissipation regime (i.e. $\phi \ll 1$ and $Q \gg 1$), it is possible to approximate the complex expression (1.8) as $\omega_n^{diss} \propto \sqrt{E_{Y,eff}(1 + i\phi)} \approx \sqrt{E_{Y,eff}}(1 + i\frac{\phi}{2})$ and define the eigenfrequencies for an under-damped resonator

$$\omega_n^{diss} \approx \left(1 + i\frac{1}{2Q}\right) \omega_n \quad (1.23)$$

As a consequence, the full displacement solution for a free vibrating beam with very

low damping maintains the mode shapes and the oscillating frequencies of the undamped case with the only addition of a characteristic exponential decay term

$$w(z, t) = \sum_{n=0}^{\infty} u_n(z) r_n(t) e^{-\frac{\omega_n}{2Q} t} \quad (1.24)$$

Finally, the expression of the normal equations of motion can be rederived by using the complex frequencies ⁹ in (1.23) and expressed as:

$$M\ddot{r}_n(t) + \Gamma_n \dot{r}_n(t) + M\omega_n^2 r_n(t) = F_n(t) \quad \text{for } n = 0, \dots, \infty \quad (1.25)$$

where $\Gamma_n = \frac{M\omega_n}{Q}$ is the resonator's *mechanical dissipation*. This equation, corresponding to a damped harmonic oscillator (mass-damper-spring system), will be used in the following to describe the linear response of each flexural mode of the NW.

Note that, since M is identical for all the modes and we assumed the quality factor $Q^{-1} = \phi$ constant, Γ_n appears to increase proportionally to the mode's frequency. This is not generally true because Q is function of ω_n and higher order modes tend to have higher quality factors. In reality, the sources of mechanical dissipation are multiple, difficult to model individually and they all add up as $Q^{-1} = \sum_i Q_i^{-1}$ [41]. In our case, since the NWs are operated in vacuum at 10^{-6} mbar, the acoustic dissipation is negligible ¹⁰ and Q is limited by intrinsic dissipation mechanisms. Mainly, vibrational energy can be dissipated by internal friction and via coupling to the substrate (clamping losses), due to the time-varying strain radiating elastic energy into the substrate at the clamping (i.e. point of maximum strain). Internal friction is associated with the viscoelastic model we adopted previously, and accounts for defects in the crystalline NW bulk (e.g. stacking faults) [42] and surface losses [20, 43]. The latter are related to the high surface-to-volume ratio of nano-mechanical resonators which amplifies the role of surface defects and impurities over the bulk's properties.

1.1.2 Mechanical polarizations

Up to this point, we gave the description of the flexural normal modes $\{u_n\}$ of a NW and its natural frequencies $\{\omega_n\}$ along one of the two *centroidal principal axes* of the generic NW's cross-section (i.e. x -axis) – concept we introduced at the beginning of subsection 1.1.1. The same equations apply to the NW bending along the other principal axis (i.e. y -axis): its displacement is still described by the same set of mode shapes $\{u_n\}$, while the natural frequencies might differ. In fact, from the eigenfrequency expression (1.8) follows that $\omega_{n,x} \propto \sqrt{I_y}$ with the second moment of area being the only parameter responsible – in case of if $I_y \neq I_x$ – for a difference of the natural frequencies sets $\{\omega_{n,x}\} \neq \{\omega_{n,y}\}$. Note that the eigenfrequency spacing is conserved since it depends on β_n , which is set by the mode shape's solution.

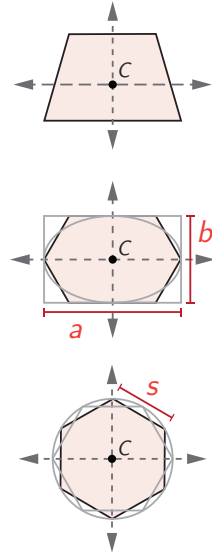
In general, the natural response of a NW to a transverse displacement in the xy -plane is oriented along the centroidal principal axes for which the bending moments result uncoupled. These two directions correspond to the axis of minimum and maximum moment of inertia for the cross-section.

⁹ $\langle u_n, u_n \rangle_k = M\omega_n^2(1 + i/2Q)^2 \approx M\omega_n^2(1 - i/Q) = M\omega_n^2 + \frac{M\omega_n}{Q} \frac{d}{dt}$

¹⁰Below 10^{-3} mbar Q is not pressure limited

If the NW's cross-section shows any symmetry, the natural directions of vibration can be determined by simple geometrical considerations [44]:

- *Singly symmetric* cross-section: the axis of symmetry is one of the centroidal principal axes of the cross section; the other principal axis is perpendicular to the axis of symmetry at the centroid.
- *Doubly symmetric* cross-section: the two axes of symmetry are centroidal principal axes (e.g. rectangle, ellipse, elongated hexagon).
- *Multiple non-orthogonal symmetry axes*: the moments of area are invariant respect to rotation around the centroid. The modes are degenerate and the NW will vibrate without preference in all planes of flexural vibration with the same eigenfrequencies $\{\omega_n\}$ (e.g. n -sided regular convex polygon, circle).



The III-V semiconductor NWs studied in this thesis are grown by Molecular Beam Epitaxy (MBE) – as will be discussed later in section 1.4.1 – along the [111] direction of a Si or GaAs substrate, which ideally leads to regular *hexagonal* cross-sections. However, due to unavoidable asymmetries, a non degenerate set of orthogonal modes is commonly observed, with consequent splitting of the frequencies [25, 33, 45–49]. An analogous behavior has been reported for circular cross-sections in NWs [22, 24, 32, 50] and carbon nanotubes (CNT) [26, 51].

For the rest of the manuscript, we will focus exclusively on the two polarizations of the fundamental flexural mode, directed along the unitary vectors $\hat{\mathbf{r}}_i$ for $i = 1, 2$, as sketched in Fig. 1.3. For the sake of brevity, we will refer to them as ‘modes’ and where needed, the subscripts $i, 1, 2$ will be used to refer to them. The axis $\hat{\mathbf{r}}_1$ is always assigned to the slowest mode with frequency $f_1 < f_2$.

The vibration spectrum of all the investigated as-grown NWs has shown a well defined frequency splitting $\Delta f = f_2 - f_1$. The lifting of the mode degeneracy can be attributed to several kinds of inhomogeneities (e.g. material and clamping anisotropies) and the effect of a slight cross-sectional asymmetry is very effective and plausible for a self-assembled growth process [47, 48]. Fig. 1.3 shows the result of such asymmetry, parametrized by the aspect ratio (AR) between the major axis a and the minor axis b . Assuming all the other quantities homogeneous and constant, follows from equation (1.8) that the relative frequency split can be expressed as:

$$\frac{\Delta f}{f_1} = \frac{f_2}{f_1} - 1 = \frac{\sqrt{I_1}}{\sqrt{I_2}} - 1 \quad (1.26)$$

where I_1 and I_2 are the moments of area¹¹ calculated with respect to the principal axis r_1 and r_2 , respectively.

¹¹For a regular hexagon of side $s = \frac{a}{2}$:
 $I_1 = I_2 = \frac{5\sqrt{3}}{16} s^4$

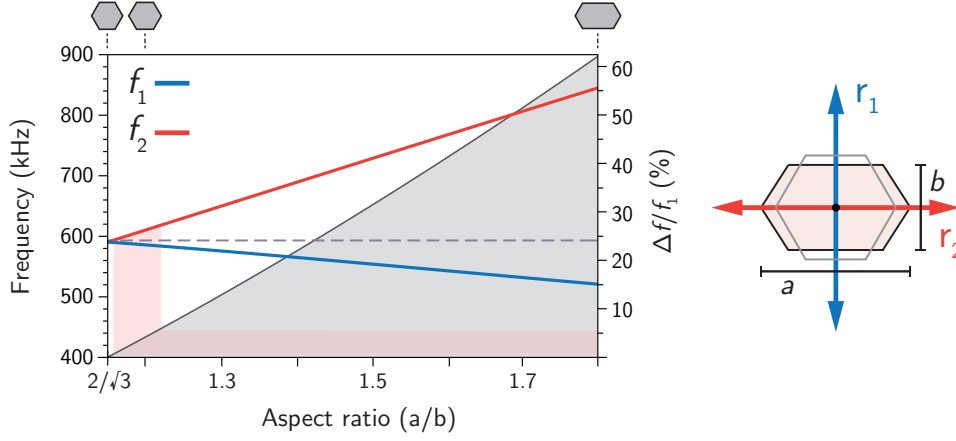


FIGURE 1.3 | **Fundamental mode splitting for an asymmetric hexagonal NW.**

The relative frequency split $\Delta f/f_1 = (f_2 - f_1)/f_1$ (grey filled line) is calculated analytically as a function of the increasing hexagon aspect ratio keeping a constant area $A = \frac{3}{4}ab$ (i.e. elongation along r_2 and shrinking along r_1). For a regular hexagon $\frac{a}{b} = 2/\sqrt{3}$. As an example, the corresponding evolution of the first mode frequencies (blue and red line) are calculated using equation (1.8) for a typical GaAs NW with starting major diagonal $a = 240$ nm, $L = 16$ μm , $\rho = 5320$ kg/m³ and $E_Y = 141$ GPa [52]. Typical splitting values are indicated by the red shaded area.

In Table 1.2 are reported the frequency split and aspect ratio statistics for the NWs studied in the next chapters. Note that – in general – the frequency difference is enhanced for shorter beams since $\Delta f \propto L^{-2}$.

| NW sample: GaAs | # tot. | $L \times a$ (μm) | $\overline{\Delta f}$ (kHz) | $\overline{\Delta f}/f_1$ (%) | AR |
|-------------------------|--------|--------------------------------|-----------------------------|-------------------------------|------|
| w/ AlGaAs shell (Ch. 3) | 4 | 25×0.35 | 9 | 2.3 ± 0.7 | 1.17 |
| w/ MnAs tip (Ch. 4) | 52 | 17×0.23 | 20 | 5 ± 4.3 | 1.2 |

TABLE 1.2 | **Frequency split and aspect ratio statistics on measured NW samples**

Finally, we want to remark that such slight asymmetries entail the orthogonality of the flexural modes and separate their frequencies by few percentage points, which in turn keeps their modal stiffnesses $k_i = M\omega_i^2$ almost identical ($k_1 \approx k_2$). These are the essential features that enable the use of NWs as bi-dimensional force sensor. Since the NWs are driven at very small deflection angles, the vertical component of the displacement at the tip $\Delta h \approx r_i^2/l_e$ results a thousand times smaller than the transversal oscillation amplitude r_i . Therefore, only the 2-D motion of the NW in the r_1r_2 -plane is considered. In the small deflection limit, effective length l_e is a frequently used quantity to describe the cantilever motion. In fact, the tangent to the end of the NW is tilted by an angle θ and always intersects the same point along the rest axis. The effective length is defined to be the distance from this point to the end of the NW and for the first order flexural modes $l_e = L/1.38$. As described in Section 4.3, in

dynamic torque magnetometry, the cantilever motion is often expressed as a function of the tilt angle $\theta \approx r_i/l_e$.

1.2 Force Detection

1.2.1 Mechanical susceptibility

The modal decomposition reduces the mechanical problem to the evaluation of independent equations of motion in the form of damped harmonic oscillators. Linear response theory provides powerful mathematical tools to describe the input/output (i.e. force/displacement) relation of each mode. The time dependent solution given in (1.25) in response to an impulsive force $F(t) = \delta(t)$, with $\delta(t)$ being the Dirac delta function¹², corresponds to the free evolution of the system $h(t)$. In the linear regime, for any driving force $F(t)$, the resulting displacement can be calculated as $r(t) = h(t) * F(t)$, where the symbol $*$ denotes the convolution operation.

Fourier analysis greatly simplifies the characterization of linear systems such as the damped harmonic oscillator: by Fourier transforming Eq. (1.25), the input/output relation is expressed as the system's transfer function or *mechanical susceptibility*

$$\chi(\omega) = \frac{\hat{r}(\omega)}{\hat{F}(\omega)} = \frac{1}{M(\omega_n^2 - \omega^2) - i\omega\Gamma} \quad (1.27)$$

where $\hat{\cdot}$ indicates the Fourier transformed¹³ function and $\chi(\omega) = \hat{h}(\omega)$.

The temporal convolution is replaced by a multiplication in the frequency domain and the resonator's response can be simply expressed using the polar representation¹⁴

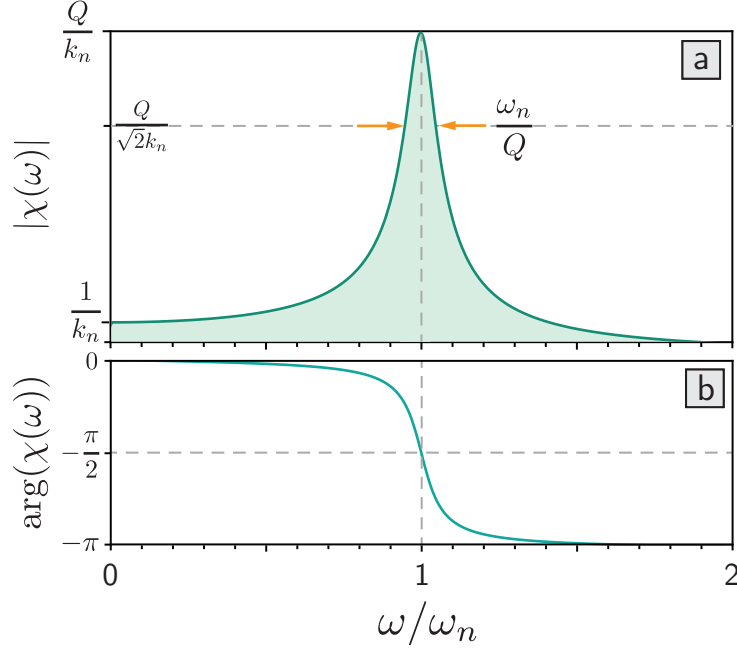
$$\hat{r}(\omega) = \chi(\omega)\hat{F}(\omega) = |\chi(\omega)| \left| \hat{F}(\omega) \right| e^{i[\arg(\chi(\omega)) + \arg(\hat{F}(\omega))]} \quad (1.28)$$

When the oscillator is driven with a monochromatic force $F(t) = F_d \cos(\omega_d t + \phi_d)$ – equivalent to an impulse in frequency $\hat{F}(\omega) = F_d e^{i\phi_d} \delta(\omega - \omega_d)$ – it responds at the same frequency of the drive with amplitude and phase modified by its transfer function according to equation (1.28): $\hat{r}(\omega) = F_d |\chi(\omega_d)| e^{i[\phi_d + \arg(\chi(\omega_d))]} \delta(\omega - \omega_d)$.

From the transfer function plotted in Fig. 1.4 it is possible to highlight the ‘amplification’ characteristic of a resonator used as a *force transducer*: in the *non-resonant* case $\omega_d \ll \omega_n$ the oscillation follows adiabatically the driving force with almost zero lag (i.e. $\arg(\chi(\omega)) \rightarrow 0$) and the amplification factor drops to the inverse of the spring-constant k_n (Hooke's law) for a constant force ($\omega_d \rightarrow 0$). Conversely, in case of *resonant* driving at $\omega_d = \omega_n$, the displacement gets enhanced by a factor Q and lags the driving force by $-\pi/2$.

A high- Q oscillator is therefore an extremely sensitive force sensor when operated close to resonance and acts like a very narrow band-pass filter at ω_n with bandwidth $\Delta\omega = \omega_n/Q$.

¹² $\delta(t) := \begin{cases} \infty & \text{for } t = 0 \\ 0 & \text{for } t \neq 0 \end{cases}$ ¹³ $\hat{r}(\omega) = \mathcal{F}\{r(t)\} = \int_{-\infty}^{+\infty} r(t)e^{i\omega t} dt$
 $\int_{-\infty}^{+\infty} \delta(t) dt = 1$ and $r(t) = \mathcal{F}^{-1}\{\hat{r}(\omega)\} = \frac{1}{2\pi} \int_{-\infty}^{+\infty} \hat{r}(\omega)e^{-i\omega t} d\omega$
¹⁴ $|\chi(\omega)| = \sqrt{\chi(\omega)\chi^*(\omega)}$
 $\arg(\chi(\omega)) = \frac{\text{Im}(\chi(\omega))}{\text{Re}(\chi(\omega))}$

FIGURE 1.4 | **Mechanical susceptibility**

Mechanical transfer function for a damped harmonic oscillator for a $Q = 10$. (a) Amplitude response with a -3dB bandwidth $\Delta\omega = \omega_n/Q$. (b) Phase response with characteristic $-\pi/2$ phase shift on resonance. At $\omega \gg \omega_n$ the system does not respond anymore, being in anti-phase to the driving force.

As a concluding remark, linear response theory has been adopted throughout this work since the vibration of the NWs has been always found proportional to the magnitude of the applied driving force, with a frequency dependence entirely described by $|\chi(\omega)|$. For stronger driving, the small angle assumption for NWs in pure bending breaks down and more complex geometrical nonlinearities rise from large deformations. The motion of GaAs NWs in the nonlinear regime has been extensively studied [47, 48] and requires the extension of Eq. (1.25) with an additional cubic term (Duffing term) αr_1^3 and a non-linear coupling term $\alpha r_1 r_2^2$, where r_2 is the displacement of a flexural modes oscillating in the orthogonal direction.

Bi-dimensional sensing

Taking advantage of the two mechanical polarizations featured by quasi-symmetrical beams, we can expand the in-plane dynamics of the NW $\mathbf{r}(t)$ subjected to a force $\mathbf{F}(t)$ on the modes' basis $(\hat{\mathbf{r}}_1, \hat{\mathbf{r}}_2)$. Therefore, the general equation of motion for $\mathbf{r}(t) \equiv [r_1(t), r_2(t)]^T$ can be written in vectorial form in terms of two independent damped harmonic oscillators (Eq. (1.25)):

$$M\ddot{\mathbf{r}}(t) + \begin{bmatrix} \Gamma_1 & 0 \\ 0 & \Gamma_2 \end{bmatrix} \dot{\mathbf{r}}(t) + \begin{bmatrix} M\omega_1^2 & 0 \\ 0 & M\omega_2^2 \end{bmatrix} \mathbf{r}(t) = \mathbf{F}(t) \quad (1.29)$$

In the frequency domain, the equation takes a more compact form $\mathbf{r}(\omega) = \boldsymbol{\chi}(\omega) \cdot \mathbf{F}(\omega)$ by defining the bi-dimensional mechanical susceptibility as

$$\boldsymbol{\chi}^{-1}(\omega) = \begin{bmatrix} M(\omega_1^2 - \omega^2) - \Gamma_1\omega & 0 \\ 0 & M(\omega_2^2 - \omega^2) - \Gamma_2\omega \end{bmatrix} \quad (1.30)$$

1.2.2 Thermal noise

A mechanical oscillator is not an isolated system, but it interacts with the environment. The sources of such interaction are mainly random collisions with gas molecules and the phonons of the substrate coupled via the clamping point. The cumulative action of these random processes can be statistically modeled as a heat bath with many microscopic degrees of freedom, coupled to the resonator and in thermal equilibrium with it.

Therefore, even in absence of an external drive, a linear resonator (i.e. n^{th} flexural mode) in equilibrium at temperature $T > 0$ experiences displacement fluctuations $r_n = \delta r_n$ about its rest position and equation (1.25) can be written in form of the so-called *Langevin equation*:

$$M\ddot{\delta r}_n + M\omega_n^2\delta r_n = -\Gamma_n\dot{\delta r}_n + \delta F \quad (1.31)$$

which describes the *Brownian motion* of a particle (i.e. effective mass along the normal coordinate) subject to a stochastic force $\delta F(t)$ in a harmonic potential $\mathcal{E}_P = \frac{1}{2}M\omega_n^2 r_n^2$. The presence of a damping Γ_n in the system suggests that any oscillation would continue to decrease in amplitude endlessly. The inclusion of the fluctuating force δF essentially prevents the system temperature from dropping below that of the system's surrounding [53].

On the time scale of the oscillator's dynamics, the randomly fluctuating force δF is modeled as an uncorrelated Gaussian process with zero mean¹⁵. This assumption is reasonable since the mass of the mode has a much larger inertia compared to the single excitations (e.g. colliding gas molecules) and its motion is a result of a great number of events separated on a time scale much shorter than the Brownian motion itself [54, 55]. Hence, δF has a memoryless autocorrelation function

$$R_{\delta F}(\tau) \equiv \langle \delta F(t), \delta F(t - \tau) \rangle = \lim_{T \rightarrow \infty} \frac{1}{T} \int_{-T/2}^{T/2} \delta F(t) \delta F(t - \tau) dt = N_{th} \delta(\tau) \quad (1.32)$$

where $\langle \dots \rangle$ indicates a time average (i.e. equivalent to the expectation $\mathbb{E}[\dots]$ for an ergodic process) and $\delta(t)$ is the Dirac delta function.

For convenience, we consider the Fourier transformed thermal fluctuations $\hat{\delta F}(\omega) = \mathcal{F}\{\delta F(t)\}$ and we analyze such stationary process in terms of its double-sided *power spectral density* (PSD) defined as

$$\overline{S}_{\delta F}(\omega) \equiv \langle \hat{\delta F}(\omega)^2 \rangle \quad (1.33)$$

which is related by the *Wiener-Khinchin theorem* to the autocorrelation function in the time domain as

$$\overline{S}_{\delta F}(\omega) = \mathcal{F}\{R_{\delta F}(\tau)\} = \int_{-\infty}^{+\infty} R_{\delta F}(\tau) e^{i\omega\tau} d\tau = \hat{R}_{\delta F}(\omega) \quad (1.34)$$

¹⁵Additive Gaussian White Noise (AGWN)

Taking $\tau = 0$ in equation (1.34) yields *Parseval's theorem*^[56]:

$$R_{\delta F}(0) = \langle \delta F(t)^2 \rangle = \mathcal{F}^{-1}\{\bar{S}_{\delta F}(\omega)\}|_{\tau=0} = \frac{1}{2\pi} \int_{-\infty}^{+\infty} \langle \delta \hat{F}(\omega)^2 \rangle d\omega \quad (1.35)$$

that demonstrates the equivalence of the total energy for the two dual representations, whereas the square signal averaged over time is equal to the integral of the PSD. Since the thermal force has been modeled as white noise, it has zero mean¹⁶ and its mean-square value corresponds to an infinite variance¹⁷ $\langle \delta F^2 \rangle = N_{th} \delta(0) = \sigma_{\delta F}^2$ (i.e. infinite noise power). In a reciprocal way, relation (1.34) shows that the noise PSD has a constant power density $\bar{S}_{\delta F}(\omega) = \mathcal{F}\{N_{th} \delta(\tau)\} = N_{th}$ over the entire frequency spectrum. Note that, despite an infinite variance in the time domain, the finite bandwidth of any real resonator will roll off the frequency response, and hence determine the variance of the measured signal.

At thermal equilibrium¹⁸, the *equipartition theorem* provides an elegant result to quantify the magnitude of the thermal fluctuations associated with energy storage in independent degrees of freedom of the resonator $\{r_n\}$. Each mode splits off additively in energy due their mutual orthogonality and has an average energy equal to

$$\langle \mathcal{E}_n \rangle = \langle \mathcal{E}_{n,K} \rangle + \langle \mathcal{E}_{n,P} \rangle = \frac{1}{2} M \langle \dot{r}_n^2 \rangle + \frac{1}{2} M \omega_n^2 \langle r_n^2 \rangle = \frac{1}{2} k_B T + \frac{1}{2} k_B T = k_B T \quad (1.36)$$

where k_B is the Boltzmann's constant and T is the absolute temperature. Accordingly to the previous relation and to (1.35), the displacement variance of an oscillator's mode in equilibrium with a heat bath at finite temperature T is

$$\sigma_{\delta r}^2 = \langle \delta r_n^2 \rangle \equiv \frac{1}{2\pi} \int_{-\infty}^{+\infty} \bar{S}_{\delta r}(\omega) d\omega = \frac{k_B T}{M \omega_n^2} \quad (1.37)$$

By recalling the linear relation between force and displacement in the frequency domain $\hat{r}_n(\omega) = \chi_n(\omega) \hat{F}_n(\omega)$ introduced previously, we can use the theorem in (1.34) to express the mean-square vibrations as the integral over all frequencies of the force noise spectral density multiplied by the square of the mechanical transfer function

$$\langle \delta r_n^2 \rangle = \frac{1}{2\pi} \int_{-\infty}^{+\infty} |\chi_n(\omega)|^2 \bar{S}_{\delta F}(\omega) d\omega = \frac{N_{th}}{2\pi} \int_{-\infty}^{+\infty} |\chi_n(\omega)|^2 d\omega \quad (1.38)$$

where – from definition (1.27) – the mechanical power transfer function¹⁹ is

$$|\chi_n(\omega)|^2 = \chi_n(\omega) \chi_n^*(\omega) = \frac{1/M^2}{(\omega_n^2 - \omega^2)^2 + \omega_n^2 \omega^2 / Q^2} \quad (1.39)$$

and its integral admits a closed form solution for under-damped resonators²⁰ [57] equal to

$$\int_{-\infty}^{+\infty} |\chi_n(\omega)|^2 d\omega = \frac{\pi}{\omega_n^2 \Gamma_n M} = \frac{\pi Q}{\omega_n^3 M^2} \quad (1.40)$$

¹⁶ $\lim_{|\tau| \rightarrow \infty} R_{\delta F}(\tau) = \langle \delta F \rangle^2 = 0$

¹⁷ $\sigma_{\delta F}^2 = \langle \delta F^2 \rangle - \langle \delta F \rangle^2$

¹⁸ For $k_B T \gg \hbar \omega_n$

¹⁹ $S_r = |\chi(\omega)|^2 S_F$

²⁰ For cantilevers: $Q^{-1} < \beta_n^2 \sqrt{E_Y I \rho A}$

Finally, by equating expressions (1.38) and (1.37), a relation between the force noise PSD and the properties of the resonator is found:

$$S_{\delta F}(\omega) = 4k_B T \Gamma_n = 4k_B T \frac{\omega_n M}{Q} \quad (1.41)$$

where $S_{\delta F}$ is the *single-sided* PSD of the force noise. Although the double-sided PSD $\bar{S}_{\delta F}$ used so far has best use for mathematical analysis involving Fourier transformations, the single-sided PSD is preferable for experimental measurements where the power is integrated only on the positive frequencies' semi-axis. For real-valued quantities, the PSD is an even function i.e. $\bar{S}_{\delta F}(-\omega) = \bar{S}_{\delta F}(\omega)$, and therefore $\sigma^2 = \int_{-\infty}^{+\infty} \bar{S}_{\delta F} d\omega = 2 \int_0^{+\infty} \bar{S}_{\delta F} d\omega = \int_0^{+\infty} S_{\delta F} d\omega$.

Displacement noise The displacement spectral density $S_{\delta r}$ for a resonator in pure Brownian motion shown in Fig. 1.5(a) can be calculated as the product between the power transfer function (1.38) and the force noise PSD (1.41)

$$S_{\delta r}(\omega) = |\chi_n(\omega)|^2 S_{\delta F}(\omega) = \frac{4k_B T \omega_n}{M Q [(\omega_n^2 - \omega^2)^2 + \omega_n^2 \omega^2 / Q^2]} \quad (1.42)$$

The correspondent autocorrelation function (Fig. 1.5(b)) is obtained by applying the inverse Fourier transform to the PSD [54]

$$R_{\delta r} \equiv \mathcal{F}^{-1}\{S_{\delta r}(\omega)\} = \frac{k_B T}{M \omega_n^2} e^{-\frac{\omega_n}{2Q} \tau} \left(\cos \omega_R \tau + \frac{\omega_n}{2Q \omega_R} \sin \omega_R \tau \right) \quad (1.43)$$

with $\omega_R^2 \equiv \omega_n^2 \left(1 - \frac{1}{4Q^2}\right)$.

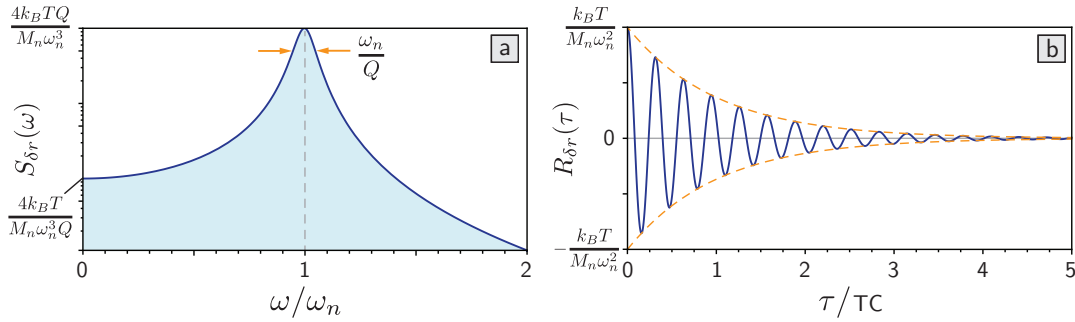


FIGURE 1.5 | **Power spectral density and autocorrelation of a resonator driven by Gaussian white noise.**

(a) Displacement noise PSD for $Q = 10$. The area under the curve equals to the variance of the displacement. The -3dB bandwidth corresponds to the Full Width Half Maximum (FWHM) of the peak. (b) Corresponding auto-correlation function. The correlation of the displacement noise in a resonator decays exponentially with a time constant $TC = 2Q/\omega_n$. On a time scale of $\tau = 5TC$ the noise results uncorrelated.

The important relations obtained for the thermal force and displacement power densities may be found using the *fluctuation-dissipation theorem* of Callen *et al.* [58],

formulated as a generalization of Nyquist-Johnson noise²¹ [59] for linear dissipative systems. In case of a viscous force, it is possible to define for the system a mechanical impedance as

$$Z(\omega) \equiv \mathcal{F} \left\{ \frac{F(t)}{\dot{r}(t)} \right\} = \frac{\hat{F}}{-i\omega\hat{r}} = \frac{i}{\omega\chi(\omega)} = \Gamma + iM\omega \left(1 - \frac{\omega_n^2}{\omega^2} \right) \quad (1.44)$$

Then, the PSD in (1.41) and (1.42) can be calculated respectively in terms of the mechanical resistance $R = \Re(Z(\omega))$ and conductance $\sigma = \Re(Z^{-1}(\omega))$ [60]:

$$S_{\delta F}(\omega) = 4k_B T R(\omega) = -\frac{4k_B T}{\omega} \Im(\chi^{-1}(\omega)) \quad (1.45)$$

$$S_{\delta r}(\omega) = 4k_B T \frac{\sigma(\omega)}{\omega^2} = \frac{4k_B T}{\omega} \Im(\chi(\omega)) \quad (1.46)$$

The intrinsic relation between fluctuations and dissipation, is guaranteed by the presence of damping, which provides both the path for mechanical energy loss and the coupling to the environment. Ultimately, an ideal undamped resonator would result in an inoperable isolated system.

According to the modal description of NW cantilevers given previously, it is possible to extend formula (1.42) to the total three-dimensional displacement fluctuation. In analogy with equation (1.24), the noise spectra add in quadrature along each mechanical polarization direction $\hat{\mathbf{r}}_i$ (for $i = 1, 2$) and are rescaled along the axial z -direction by the mode shape squared

$$S_{\delta r}(r_1, r_2, z, \omega) = \sum_{i=1,2} \left(\sum_{n=0}^{\infty} S_{\delta r_{in}}(\omega) u_n^2(z) \right) \hat{\mathbf{r}}_i \quad (1.47)$$

For the scope of this thesis, only the fundamental mode is taken into account (i.e. $n = 0$ and the subscript is dropped); by measuring the displacement at the tip (i.e. $z = L$ and $u_0(L) = 1$), the former expression reduces to

$$S_{\delta r}(r_1, r_2, \omega) = S_{\delta r_1}(\omega) \hat{\mathbf{r}}_1 + S_{\delta r_2}(\omega) \hat{\mathbf{r}}_2 \quad (1.48)$$

Despite the pronounced bi-dimensional nature of the NW displacement noise, in our setup the motion is optically detected by laser interferometry, which probes the component of the NW's trajectory collinear to the direction of the local optical gradient, as illustrated in Section 2.2.3. Therefore, the measured displacement consists of a projection of the vibrations onto a *measurement vector* \mathbf{e}_β and is equal to $\mathbf{r}_\beta(t) = \mathbf{r}(t) \cdot \mathbf{e}_\beta = \cos \beta r_1(t) \hat{\mathbf{r}}_1 + \sin \beta r_2(t) \hat{\mathbf{r}}_2$.

The correspondent PSD, in absence of coupling between the modes, is a sum of the single noise spectrum in Eq. (1.42) for each polarization, weighted by their overlap on the measurement vector \mathbf{e}_β

$$\begin{aligned} S_{\delta r_\beta}(\omega) &= \cos^2 \beta S_{\delta r_1}(\omega) + \sin^2 \beta S_{\delta r_2}(\omega) = \\ &= \frac{4k_B T}{M} \left[\frac{\cos^2 \beta \omega_1}{Q_1 [(\omega_1^2 - \omega^2)^2 + \omega_1^2 \omega^2 / Q_1^2]} + \frac{\sin^2 \beta \omega_2}{Q_2 [(\omega_2^2 - \omega^2)^2 + \omega_2^2 \omega^2 / Q_2^2]} \right] \end{aligned} \quad (1.49)$$

²¹ $\langle \delta V_{th}^2 \rangle = S_{\delta V}(\omega) = 4k_B T R$

Such expression fits the calibrated displacement noise spectrum of a GaAs NW shown in Fig. 1.6.

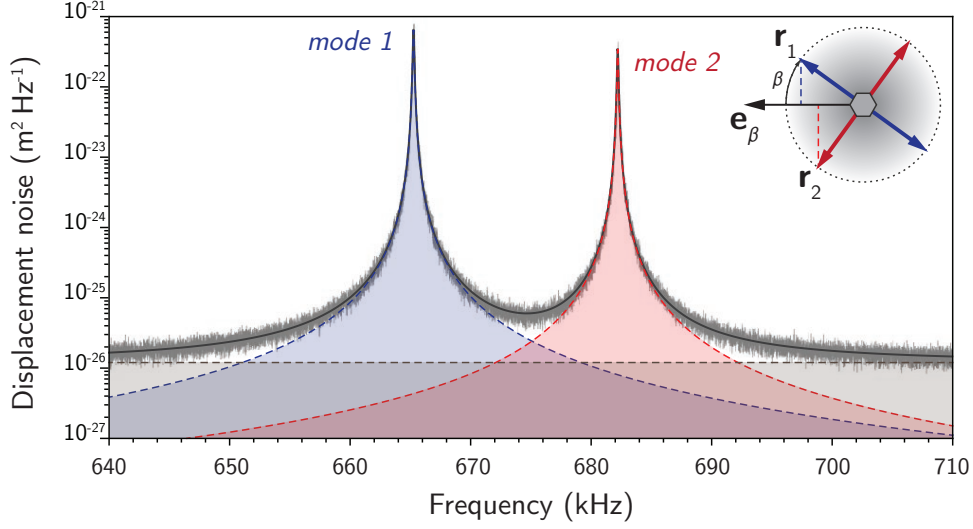


FIGURE 1.6 | **Thermal noise spectral density of a GaAs NW**

Measured thermal displacement noise (light gray) at room temperature in the frequency region of the two orthogonal polarizations of the fundamental flexural mode. The fitted line (black) is given by an incoherent sum of two Lorentian peaks (blue and red dashed lines) and the detection noise floor $S_n = 1.2 \times 10^{-26} \text{ m}^2/\text{Hz}$ (dashed gray line). According to Eq. (1.42), the extracted parameters are $M = 1 \times 10^{-16} \text{ kg}$, $f_1 = 665 \text{ kHz}$, $Q_1 = 5425$, $f_2 = 682 \text{ kHz}$, $Q_2 = 5705$. The inset in the top-right corner shows the orientation of the modes respect to the measurement direction \mathbf{e}_β . The fit returns an angle $\beta = 36^\circ$.

Effective temperature At equilibrium, the temperature of the resonator is proportional to the variance of its Brownian motion as indicated by Eq. (1.37). However, out of equilibrium the force noise expression given in Eq. (1.41) is no longer valid and the resonator temperature can differ from the bath temperature T . The effective resonator temperature T_n can still be quantified as:

$$T_n \equiv \frac{M\omega_n^2}{k_B} \langle r_n^2 \rangle = \frac{M\omega_n^2}{k_B} \frac{1}{2\pi} \int_0^{+\infty} S_{\delta r}(\omega) d\omega \quad (1.50)$$

where the actual displacement variance is proportional to T_n and is experimentally determined by calculating the area between the spectral density $S_{\delta r}(\omega)$ and the measurement noise floor [61]. Note that, from a practical point of view, a correct mode temperature estimation is linked to a correct estimation of the modal mass.

The presence of additional mechanical noise in the system at the mode's frequency or local heating due to the optical laser power used for the NW motion's readout, can be responsible of a NW's temperature higher than the environment ($T_n > T$).

Conversely, cooling techniques can be applied to reduce the resonator's mode temperature below the one of the bath by active feedback cooling [62] or more elaborated schemes – namely, back-action and sideband cooling – requiring an optomechanical coupling to an optical cavity [61, 63].

1.2.3 Force Sensitivity

We have shown that the fundamental limit to the detection of small forces is imposed by thermomechanical force noise – the mechanical analog of Nyquist-Johnson noise – which is governed by temperature and dissipation of mechanical energy.

If we consider our signal to be a monochromatic force $\hat{F}_d(\omega) = F_d\delta(\omega - \omega_d)$, taking into account the force noise $\delta\hat{F}(\omega)$, the oscillator's displacement can be expressed according to (1.27)

$$\hat{r}_i(\omega) = \chi_i(\omega)(\delta\hat{F}(\omega) + \hat{F}_d(\omega)) \quad (1.51)$$

The associated motional spectral power is obtained as $P_r(\omega) = \frac{1}{2\pi} \int_{\text{BW}} S_r(\omega) d\omega$ by integrating the PSD over a bandwidth of interest, called resolution bandwidth (BW). By choosing a BW centered around ω_d , the total power results a sum of the signal and noise power

$$P_r(\omega_d) = |\chi_i(\omega_d)|^2 S_{\delta F} \times \text{BW} + |\chi_i(\omega_d)|^2 F_d^2 \quad (1.52)$$

Following the standard definition, we can define the signal-to-noise ratio (SNR) for a force signal as the ratio of signal to the noise power $\text{SNR} = F_d^2 / (S_{\delta F} \times \text{BW})$.

The limit condition for the detection of force signal is conventionally referred to a $\text{SNR} = 1$. Since the force SNR is independent of the driving frequency, the *minimum detectable force* is equal to

$$F_{d,\min} = \sqrt{S_{\delta F} \times \text{BW}} = \sqrt{4k_b T \Gamma_i \times \text{BW}} = \sqrt{4k_b T \frac{M\omega_i}{Q_i} \times \text{BW}} \quad (1.53)$$

The resonator's *force sensitivity* is the main figure of merit in sensing applications and is usually expressed in units of $\text{N}/\sqrt{\text{Hz}}$ as $F_{\min} = \sqrt{S_{\delta F}}$. In this way, it is independent from the specific resolution bandwidth, or, conversely, from the adopted integration time.

1.3 Light-nanowire interaction

The displacement detection of a NW is performed by fiber-optic interferometry as will be illustrated in Section 2.2.2. We measure the interference between the light back-reflected by the vibrating NW and a fixed reference given by the reflection at the fiber/vacuum interface.

Therefore, we want to briefly discuss the theoretical background behind the light-NW scattering mechanism. Light-matter interaction for objects of size R comparable to the wavelength of the incident light ($R \approx \lambda$) cannot be simplified by applying the so called dipole approximation (Rayleigh) for point-like scatterers ($R \ll \lambda$), but require the more general treatment provided by Lorenz-Mie theory.

Conversely to sub-wavelength spherical particles, the optical response of one-dimensional structures like NWs is strongly polarization dependent, offering an additional degree of freedom, supplementary to their material and geometrical features [64].

The Mie scattering theory has also been applied to optimize the motion detection of SiNWs by coupling the resonant leaky modes to a Fabry-Perot cavity [65] or to tailor absorption properties for optoelectronic applications [66].

We present in the following the standard formalism for a cylindrical NW, which represents a very good approximation of a hexagonal NW, specially infrared wavelengths

and under normal illumination [64, 67]. To be more quantitative, the scattering problem for a NW with hexagonal cross-section can be approximated by Discretized Mie Formalism [68] or solved numerically.

1.3.1 Scattering of an infinitely long cylinder

In Mie theory, the Maxwell's equations are used for the mathematical derivation of the incident, scattered and internal fields. The analytical solution is expressed in form of an infinite series expansion of vector spherical or cylindrical harmonics.

Due the high aspect ratio of NWs, i.e. $L \gg 2R$, it is possible to follow the formal solution developed by Mie for infinitely long cylinders. Such solution does not apply when detecting the motion at the base and at the tip of the NW.

We consider an infinite cylindrical NW of homogenous dielectric material, with complex relative refractive index²² \bar{m} ; centered in the origin and aligned along the z -direction.

Assuming the light waves to be periodic with time dependence $e^{-i\omega t}$ and propagating in a linear, isotropic and homogeneous medium, the electromagnetic field (\mathbf{E}, \mathbf{H}) must satisfy Helmholtz wave equation (e.g. $\nabla^2 \mathbf{E} + k^2 \mathbf{E} = \mathbf{0}$), together with the boundary conditions at the vacuum/NW interface (i.e. conservation of the tangential component). If ψ_n is solution of the correspondent scalar wave equation²³, then it can be the generating function of vector harmonics

$$\mathbf{M}_n = \nabla \times (\mathbf{e}_z \psi_n) \quad \text{and} \quad \mathbf{N}_n = \nabla \times \mathbf{M}_n / k \quad (1.54)$$

which are orthogonal basis of solutions of the vector wave equation; \mathbf{e}_z is called pilot vector and k is the wave vector²⁴. For an infinite cylinder, the solutions of the scalar wave equation²⁵ are separable in the cylindrical coordinates, $\psi_n(\rho, \phi, z)$. The scalar problem is then written in form of a Bessel equation whose linearly independent solutions are the Bessel functions of first and second kind, J_n and Y_n (order n), and their linear combination $H_n = J_n + iY_n$ (Hankel functions) [69].

Given the geometry of our detection scheme, using a laser beam focused on the side of the NW, we consider the case – sketched in Fig. 1.7 – of an incident planar wave polarized orthogonally respect to the NW axis (i.e. $\mathbf{E}_i \perp \mathbf{H}_i \perp \mathbf{e}_\rho$):

$$\mathbf{E}_i(\rho, \phi) = \mathbf{E}_i e^{-ik\rho \cos \phi} \quad (1.55)$$

The incident electromagnetic field can be decomposed in cylindrical harmonics and resolved into two main components:

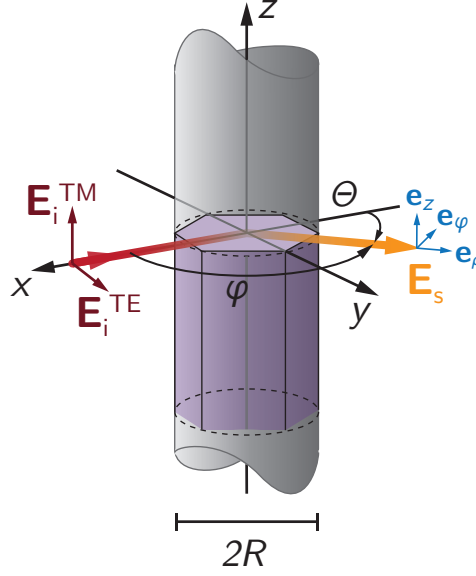
- I - *Transverse Magnetic* (TM) mode. The magnetic field of the incident wave is perpendicular to the cylinder axis. This implies that, in general, the electric field lies in the ρz -plane. In our case, $\mathbf{E}_i^{TM} = E_i \mathbf{e}_z$.
- II - *Transverse Electric* (TE) mode. The electric field is perpendicular to the cylinder axis, $\mathbf{E}_i^{TE} = E_i \mathbf{e}_\phi$.

²² $\bar{\epsilon}_r = \epsilon_r + i\tilde{\epsilon}_r \equiv \bar{m}^2 = (m - i\kappa)^2$

²³ $\nabla^2 \psi_n + k^2 \psi_n = 0$

²⁴ $k = k_0 m = \frac{2\pi}{\lambda} = \omega \sqrt{\epsilon \mu}$

²⁵ $\frac{1}{\rho} \frac{\partial}{\partial \rho} \left(\rho \frac{\partial \psi_n}{\partial \rho} \right) + \frac{1}{\rho^2} \frac{\partial^2 \psi_n}{\partial \phi^2} + \frac{\partial^2 \psi_n}{\partial z^2} + k^2 \psi = 0$

FIGURE 1.7 | **Scheme for the Mie scattering problem.**

For an arbitrary elliptically polarized incident wave the solutions can be found by an appropriate superposition of the two polarizations $\mathbf{E}_i = \sum_{-\infty}^{+\infty} [A_n \mathbf{M}_n^i + B_n \mathbf{N}_n^i]$, with coefficients A_n and B_n obtained projecting \mathbf{E}_i on the vectors of the basis.

For this configuration, the incident wave (1.55) can be expanded in vector harmonics ($\mathbf{M}_n^i, \mathbf{N}_n^i$) in the form of Eqs.(1.54) and generated by $\psi_n^i(\rho, \phi) = J_n(k\rho)e^{in\phi}$ as

$$\begin{aligned} \mathbf{M}_n^i(\rho, \phi) &\equiv k e^{in\phi} \left(i n \frac{J_n(k\rho)}{k\rho} \mathbf{e}_\rho - J'_n(k\rho) \mathbf{e}_\phi \right) \\ \mathbf{N}_n^i(\rho, \phi) &\equiv -k e^{in\phi} J_n(k\rho) \mathbf{e}_z \end{aligned} \quad (1.56)$$

On this basis the incident field²⁶ can be expanded for both polarizations as [69]

$$\text{I:} \quad \mathbf{E}_i^{TM}(\rho, \phi) = \sum_{n=-\infty}^{\infty} E_n \mathbf{N}_n^i, \quad \mathbf{H}_i^{TM}(\rho, \phi) = -i \frac{k}{\omega\mu} \sum_{n=-\infty}^{\infty} E_n \mathbf{M}_n^i \quad (1.57)$$

$$\text{II:} \quad \mathbf{E}_i^{TE}(\rho, \phi) = -i \sum_{n=-\infty}^{\infty} E_n \mathbf{M}_n^i, \quad \mathbf{H}_i^{TE}(\rho, \phi) = -\frac{k}{\omega\mu} \sum_{n=-\infty}^{\infty} E_n \mathbf{N}_n^i \quad (1.58)$$

where $E_n = E_0(-i)^n/k$.

The full solution to the Maxwell equation requires an additional field (scattered field) to satisfy the tangential component continuity of the external and internal field²⁷ at the cylinder surface (NW's conductivity is supposed to be zero).

The scattered field ($\mathbf{E}_s, \mathbf{H}_s$) needs to be expanded on a basis ($\mathbf{M}_n^s, \mathbf{N}_n^s$) calculated as in (1.54), with a generating function $\psi_n^s(\rho, \phi) = H_n(k\rho)e^{in\phi}$.

²⁶ $\mathbf{H} = -\frac{i}{\omega\mu} \nabla \times \mathbf{E}$

²⁷Internal generating function is $\psi_n = J_n(mk\rho)e^{in\phi}$

Under our simplifying assumption of normal incidence, is found

$$\text{I:} \quad \mathbf{E}_s^{TM}(\rho, \phi) = - \sum_{n=-\infty}^{\infty} E_n b_n \mathbf{N}_n^s, \quad \mathbf{H}_s^{TM}(\rho, \phi) = i \frac{k}{\omega \mu} \sum_{n=-\infty}^{\infty} E_n b_n \mathbf{M}_n^s \quad (1.59)$$

$$\text{II:} \quad \mathbf{E}_s^{TE}(\rho, \phi) = i \sum_{n=-\infty}^{\infty} E_n a_n \mathbf{M}_n^s, \quad \mathbf{H}_s^{TE}(\rho, \phi) = \frac{k}{\omega \mu} \sum_{n=-\infty}^{\infty} E_n a_n \mathbf{N}_n^s \quad (1.60)$$

with the Mie scattering coefficients b_n and a_n obtained by imposing the boundary conditions at $\rho = R$

$$b_n = b_{-n} = \frac{J_n(mkR)J'_n(kR) - mJ'_n(mkR)J_n(kR)}{J_n(mkR)H'_n(kR) - mJ'_n(mkR)H_n(kR)} \quad (1.61)$$

$$a_n = a_{-n} = \frac{mJ_n(mkR)J'(kR) - J'_n(mkR)J_n(kR)}{mJ_n(mkR)H'_n(kR) - J'_n(mkR)H_n(kR)} \quad (1.62)$$

Each coefficient sets the contribution of the respective mode n to the total field. Since $H_n = H_{-n}$, the basis functions are usually considered as $(N_n^s + N_{-n}^s)$ to obtain to eigenfunctions of increasing order $n \geq 0$. From the normalized modulus of the first five modes shown in Fig. 1.8, is possible to recognize a progression in the spatial profiles similar to a multipolar expansion (i.e. monopole, dipole, quadrupole etc.). The complexity and confinement in the near-field of the modes increases with n , with the number of lobes scaling up as $2n$.

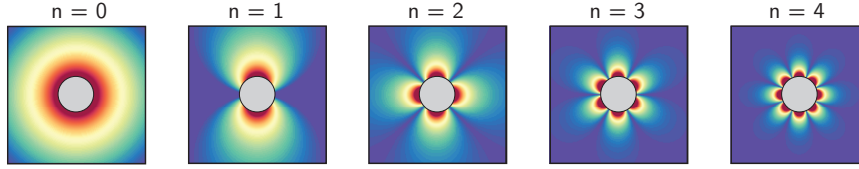


FIGURE 1.8 | **Mie scattering modes.**

Rescaled modulus of the first five modes $(N_n^s + N_{-n}^s)$ for a cylinder of radius $R = 115$ nm. Domain size is $1\mu\text{m} \times 1\mu\text{m}$.

Far-field scattering The light back-scattered by the NW is detected at large distance ($k\rho \gg 1$), therefore we are interested in an asymptotic expression for the scattered field.

The relation between the incident field in Eq. (1.55) with $\mathbf{E}_i = E_i^{TM} \mathbf{e}_z + E_i^{TE} \mathbf{e}_\rho$ and the correspondent scattered field $\mathbf{E}_s = E_s^{TM} \mathbf{e}_z + E_s^{TE} \mathbf{e}_\rho$ is given by the *amplitude scattering matrix* \mathbf{T} [69]:

$$\begin{bmatrix} E_s^{TM} \\ E_s^{TE} \end{bmatrix} = e^{i3\pi/4} \sqrt{\frac{2}{\pi k \rho}} e^{ik\rho} \begin{bmatrix} T_1 & 0 \\ 0 & T_2 \end{bmatrix} \begin{bmatrix} E_i^{TM} \\ E_i^{TE} \end{bmatrix} \quad (1.63)$$

with $T_1 = b_0 + 2 \sum_{n=1}^{\infty} b_n \cos(n\Theta)$ and $T_2 = a_0 + 2 \sum_{n=1}^{\infty} a_n \cos(n\Theta)$.

The scattering angle $\Theta = \pi - \phi$ is the deviation with respect to the incident wave, e.g. forward scattering for $\Theta = 0$ (see Fig. 1.7). In far-field, the scattered wave has

an ideal cylindrical front (surface of constant phase). Note that, if the NW is not normally illuminated, the T-matrix is not diagonal.

Poynting vector and scattering efficiency One of the most important properties of electromagnetic waves is the flux of energy through a certain area. The Poynting vector $\mathbf{S} = \frac{1}{2}\text{Re}(\mathbf{E} \times \mathbf{H}^*)$, defines the magnitude and direction of the time-averaged flux of energy crossing a unit area (Wm^{-2}). As a consequence, the rate of energy W crossing a surface A with normal unit vector $\hat{\mathbf{n}}$ is equal to $\int_A \mathbf{S} \cdot \hat{\mathbf{n}} dA$. At any point outside the cylinder the total energy flux can be expressed as

$$\mathbf{S} = \frac{1}{2}\text{Re}\{(\mathbf{E}_i + \mathbf{E}_s) \times (\mathbf{H}_i^* + \mathbf{H}_s^*)\} = \mathbf{S}_i + \mathbf{S}_s + \mathbf{S}_{ext} \quad (1.64)$$

The extinction term $\mathbf{S}_{ext} = \frac{1}{2}\text{Re}\{\mathbf{E}_i \times \mathbf{H}_s^* + \mathbf{E}_s \times \mathbf{H}_i^*\}$ arises from the interference between the incident and scattered waves.

In case of an infinite cylinder, the rate of energy flow per length, enclosed (absorbed) in a cylindrical surface around the NW of height L and radius $R' > R$, is equal to $W_{abs} = -L \int_0^{2\pi} \mathbf{S}(R', \phi) R' d\phi = W_i - W_s + W_{ext}$. For a non-absorbing medium (vacuum) $W_i = 0$, and the extinction is therefore the sum of energy scattering rate and absorbing rate $W_{ext} = W_s + W_{abs}$. Note that, as expected, W_{abs} does not depend on R' since the far-field solution in Eq. (1.63) scales with $\sqrt{\rho}$.

A more common quantity in scattering theory is the *scattering efficiency factor* Q which represents the energy rate normalized by the power of the incident wave on the NW's vertical cross-section $2RL$. In case of a planar wave the intensity is $I_i = \frac{1}{2} \frac{|E_i|^2}{\eta}$, where η is the characteristic impedance²⁸ of the medium.

The scattering efficiency factor $Q_s = W_s/(2RLI_i)$ can be derived integrating Eq. (1.63) for both polarizations [69] and are valid in far-field:

$$Q_s^{TM} = \frac{2}{kR} \left(|b_0|^2 + 2 \sum_{n=1}^{\infty} |b_n|^2 \right) \quad \text{and} \quad Q_s^{TE} = \frac{2}{kR} \left(|a_0|^2 + 2 \sum_{n=1}^{\infty} |a_n|^2 \right) \quad (1.65)$$

Fig. 1.9 shows Q_s in the case of GaAs NW for both polarizations, as a function of the NW radius and wavelength. For the sake of generality, the imaginary part of \bar{m} (i.e. absorption index k) is momentarily neglected to show the richness of the features provided by high order Mie resonances at shorter wavelengths.

The spectra show a series of optical resonances where strong scattering of light takes place. The resonances arise from light trapped in circulating orbits by multiple internal reflections as it occurs in whispering-gallery micro-resonators.

For TM polarized light, the NW exhibits better scattering characteristics, as clearly stated in [24]. Hence, such polarization is adopted in our detection setup using an infrared laser at $\lambda = 1550$ nm into a polarization maintaining (PM) fiber (as described in Section 2.2.2). At this wavelength, the scattered signal is given by the first two terms of the expansion (see Fig.1.9(c)). The resonant modes arise due to the wavelengths in the cross section of the cylinder match their circumference.

The complete scattering efficiency map of a GaAs NW is shown in Fig. 1.10(b) and accounts for the high absorption index of the direct band-gap semiconductor in the visible range.

²⁸ $\eta = \sqrt{\frac{\mu}{\epsilon}} \simeq \frac{1}{m\sqrt{\epsilon_0}}$

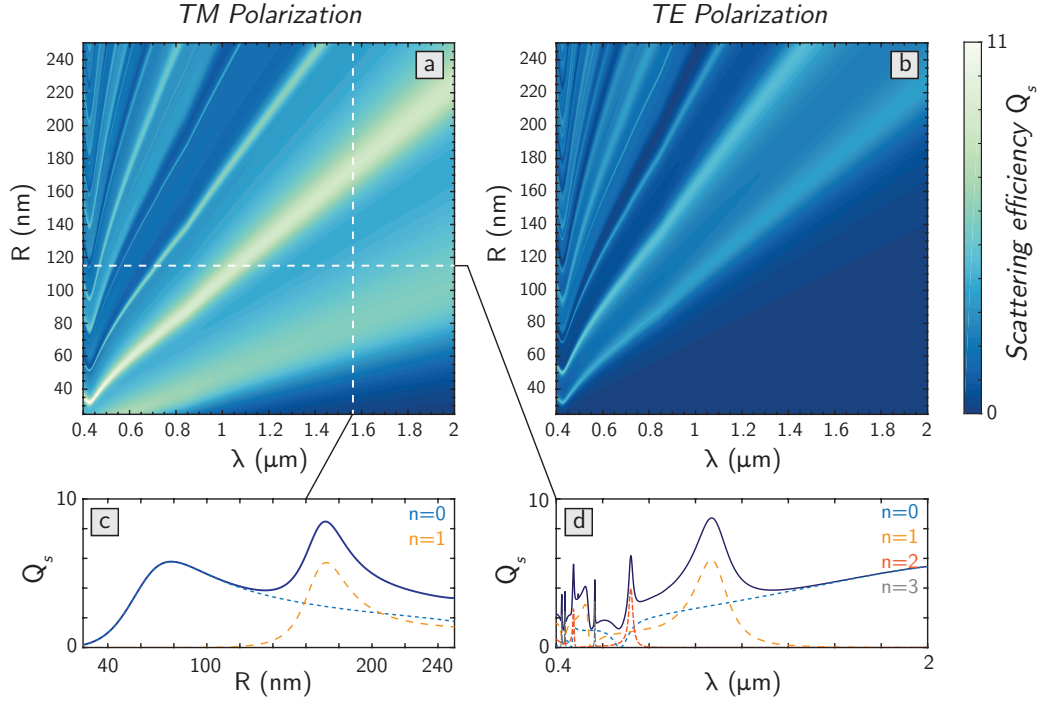


FIGURE 1.9 | **Scattering efficiencies of a transparent dielectric NW.**

(a,b) Scattering efficiency for the two main polarization under normal illumination. At low wavelength the resonance lines bend upwards due to the non-monotonic refractive index of GaAs (see m in Fig. 1.10(a)). Note that in case of unpolarized incident light, the scattering efficiency is the average of the two maps $Q_s^{unp} = \frac{1}{2}(Q_s^{TM} + Q_s^{TE})$. (c) dependence of Q_s^{TM} on NW radius at typical wavelength value $\lambda = 1550$ nm. For sufficiently small NWs and/or high enough wavelength only the the first two orders of the Mie expansion contribute significantly to the scattering. (d) Q_s^{TM} wavelength dependence at typical radius $R = 115$ nm. Each colored dashed line is associated with the m -order Mie resonance contribution ($\propto |b_m|^2$).

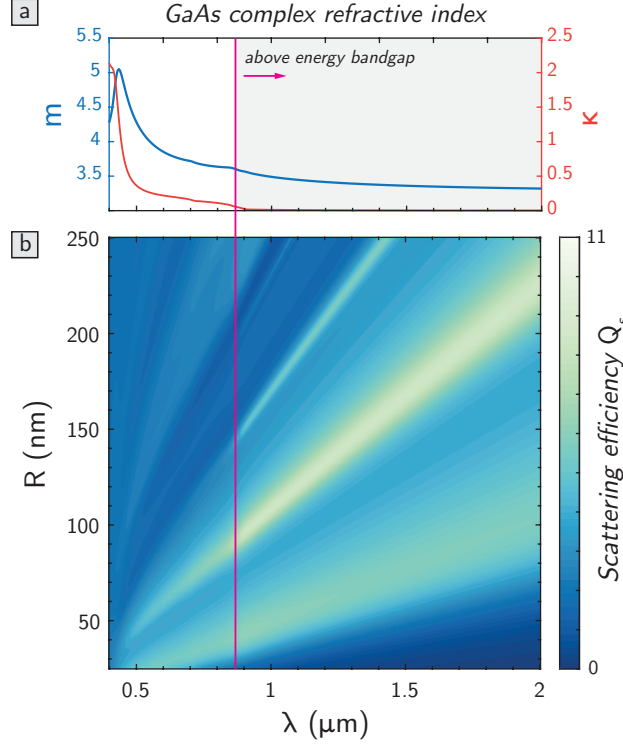


FIGURE 1.10 | **Effective scattering efficiency of a lossy dielectric NW**

(a) Complex refractive index $\tilde{m} = m - i\kappa$ for GaAs [70]. Optical absorption goes to zero over the bandgap energy of GaAs $E_g = 1.42$ eV for GaAs, i.e. where the imaginary part of the refractive index goes to zero. This corresponds to a wavelength $\lambda = 873$ nm; for longer wavelengths the material is transparent. (b) Complete scattering efficiency map for a GaAs NW obtained for \tilde{m} . Above the bandgap the map corresponds to Fig. 1.9(a).

Back-scattered light We detect the NW's motion via the back-scattered light. As a consequence, the incident wave is completely decoupled from the measured signal (\mathbf{S}_s is anti-parallel to \mathbf{S}_i), in contrast with 'transmission' techniques where the sum of both components is measured [22, 71].

The collected intensity is limited by the effective numerical aperture $\text{NA} = \sin(\phi_c/2)$ of the confocal microscope of our system (see Section 2.2.2). For this reason, even though the scattering efficiency Q_s gives a nice insight on the interplay between NW radius, wavelength and polarization, it is more interesting to evaluate the angular distribution of the scattered light via the differential (angular) efficiencies

$$\frac{dQ_s^{TM}}{d\phi} = \frac{1}{\pi k R} |T_1(\Theta)|^2 \quad \text{and} \quad \frac{dQ_s^{TE}}{d\phi} = \frac{1}{\pi k R} |T_2(\Theta)|^2 \quad (1.66)$$

obtained from Eq. (1.63).

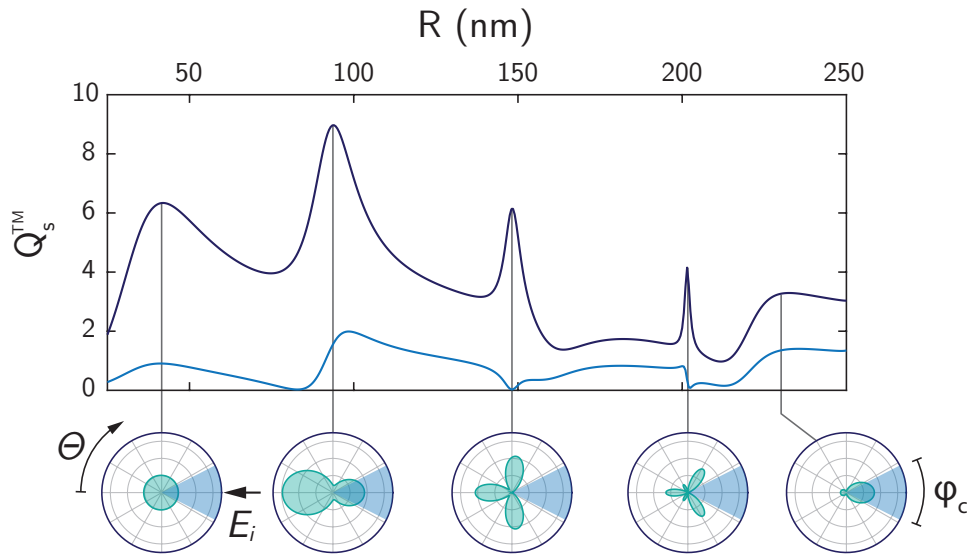


FIGURE 1.11 | **Angular scattering efficiency for a GaAs NW**

The total scattering efficiency Q_s^{TM} (dark blue) is calculated for a wavelength of $\lambda = 900$ nm. The light blue line shows the differential angular efficiency integrated over the angle of collection $\phi_c = 54^\circ$ of the objective with numerical aperture $NA = 0.45$ mounted in our setup. For each peak of the spectrum is shown the correspondent angular scattering efficiency. $\Theta = \pi - \phi$ is the back scattering angle and the polar plot edge corresponds to $dQ_s^{TM} = 3.5$.

1.4 Nanowires fabrication

In this thesis, we study the mechanical characteristics of NWs and their applications as scanning probes. In particular, we focus on NWs grown by *bottom-up* processes, in contrast to other variety of NWs and nano-mechanical devices fabricated with *top-down* micro-machining techniques (e.g. Si or diamond cantilevers [21, 72]).

The term *bottom-up* refers to a progressive epitaxial formation of the nanostructure from a nucleation point on a substrate. Starting from the first seminal work in the 60's on Si 'whiskers' created via Vapor-Liquid-Solid (VLS) crystal growth mechanism [73], several synthesis methods exploiting VLS have been developed; in particular Metal Organic Chemical Vapor Deposition (MOCVD), Metal Organic Vapor Phase Epitaxy (MOVPE) and Molecular Beam Epitaxy (MBE).

The VLS mechanism, as the name suggests, involves three different phases: liquid, solid and vapor. A liquid droplet catalyzes the growth by adsorbing a vapor to supersaturation levels and enabling the formation of a solid phase from nucleated seeds underneath the droplet.

Historically, Au catalyzed growth has been developed and established first. One of main advantage is that the diameter of the NW can be controlled just by adjusting the size of the initial Au nanoparticle and the substrate role is only limited to provide the epitaxial orientation to the NWs in order to grow them in the desired direction. In the last ten years, self-catalyzed techniques have been introduced to avoid the presence of the metallic droplet at the tip of the NW and to overcome major disadvantages such as incorporation of Au at the impurity level in the NW and the difficult growth of sharp axial heterostructures.

1.4.1 Self-catalyzed MBE grown GaAs nanowires

Both experiments – presented in Chapter 3 and 4 – make use of GaAs NWs grown from a Ga catalyst droplet by molecular beam epitaxy [74]. They have a predominantly zinc-blende crystalline structure and display a regular hexagonal cross-section. Gallium catalyst nano-droplets form by diffusion of Ga adatoms on the surface of the substrate, coated by a very thin layer of silicon oxide. In self-catalyzed growth, the substrate not only sets the NW direction but is crucial to allow the formation of the catalytic Ga droplets (on Si substrate it is possible to use directly the native oxide). A growth without the oxide layer produces a 2D polycrystalline growth.

A MBE setup operates in ultra-high vacuum at a base pressure below 10^{-10} mbar, these environmental conditions are fundamental to fulfill the molecular beam conditions, since the atoms' mean free path has to be bigger than the growth chamber. The extreme purity of the elemental sources and the low deposition rates guarantee the highest quality of crystal structure and composition.

The key parameters of the growth process are the flux rates of the gasses targeting the surface and the substrate temperature, which maintains a high mobility of the incoming atoms.

By properly tuning these parameters – specially the As_4/Ga ratio – it is possible to stabilize the crystal phase during the growth to minimize the density of defects such as stacking faults and rotational twins. Also the cross-section shape of the NWs can be influenced: for example, a higher As_4 flux rate leads to a high NW growth rate, inducing a progressive reduction of the catalyst droplet during the NW growth and therefore creating a slightly tapered cross-section. Conversely, a stronger feed of Ga

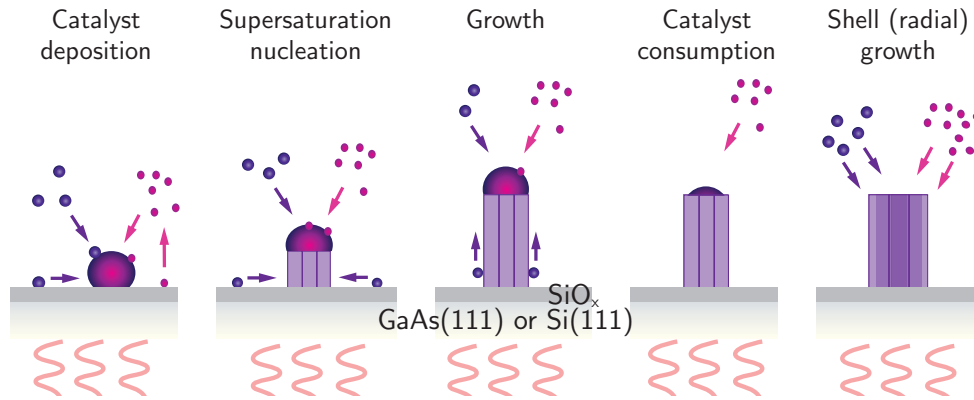


FIGURE 1.12 | **VLS mechanism for self-catalyzed NWs growth**

The substrate is heated up at a temperature of $\sim 650^\circ\text{C}$. When the material fluxes are started, Ga (in purple) diffuses forming droplets on the surface. The As atoms (in magenta) impinging onto the droplet surface are adsorbed and start to diffuse inside the droplet due to a concentration gradient. Since As has a higher vapor pressure than Ga, it tends to stay in the vapor phase through adsorption and desorption. Once the adsorbed atoms reach supersaturation, the material precipitates underneath the droplet in solid form, starting the NW growth. In this stage Ga is fed to the catalytic droplet by diffusion and As directly via flux adsorption. Finally, the vertical growth can be terminated by interrupting the both fluxes or by consuming the Ga left in the droplet keeping a As flow. The last optional step is the shell growth (e.g. passivation layer, heterostructure) by Vapor-Solid mechanism.

to the system causes droplet to increase in volume, leading to an increase in diameter. Finally, also the NW density (average number of NWs per μm^2) can be tuned (e.g. average length and density increase with substrate temperature).

MBE grown NWs as force sensors In contrast with *top-down* fabricated devices, *bottom-up* grown beam resonators present in general a larger statistical distribution of geometrical parameters such as length, diameter and cross-sectional shape. In return, nano-beams such as NWs or Carbon Nanotubes (CNT) lead to the miniaturization of the mechanical resonator which can improve the force sensitivity thanks to a drastic reduction in motional mass, yet preserving high mechanical quality factors.

MBE grown NWs have extremely pure chemical composition and very low defect density, beneficial for their stiffness properties. The NWs are singly-clamped by their crystalline relation to the substrate and their growth location can be controlled via selective beam epitaxy by pre-patterning nano holes into the oxide layer. MBE is also an extremely versatile technique, allowing for additional modification to the main GaAs NW core. For force scanning probe application, the tip can be tapered up to few nanometers by a controlled consumption of the liquid Ga catalyst [75]. Moreover, the tip can be functionalized to detect magnetic forces by turning the liquid Ga droplet into a ferromagnetic MnAs nano-crystal by exposing the NW to a strong Mn flux [35]. The main limitation of MBE grown NWs concerns the aspect ratio. In contrast to NWs obtained with industrial methods like Chemical-Vapor-Deposition (CVD), which can have aspect ratios up to 1000 to the detriment of the total mass [22], the axial and radial epitaxial growth rate are intimately linked. In this respect, the aspect ratio of our GaAs NWs are 10 times smaller, which prevent to obtain modal stiffnesses in the $\mu\text{N}/\text{m}$ range.

Chapter 2

Experimental setup

In this chapter we introduce the fundamental tools and techniques at the base of the experiments presented in this work.

We first present the main parts and instruments of the measurement setup, then, we discuss the design of the actual low temperature scanning probe microscope and its specifications.

The second section is dedicated to the optical detection and characterization of the nanowire's motion. After the characterization of the fiber-based reflection confocal microscope, we analyze interaction between light and sub-wavelength objects such as NWs in the framework of our fiber-optic interferometer setup.

Finally, we present the main aspects of the displacement detection and calibration, introducing basic practices functional to the study the NW's 2D motion.

2.1 Instrumentation

Figure 2.1 gives an overview of the main elements used to carry out the work presented in this thesis.

A ⁴He bucket dewar cryostat¹ with LN₂/vacuum shielding is fixed in the center of an optical table leaning on a 3-post passive vibration isolation system.

At the bottom of the cryostat, a superconducting magnet allows to apply a static magnetic field along the z -axis up to $B = \pm 8$ T. The cryostat probe consists of a stainless steel tube with baffling matching the ones of the magnet support assembly: the 'warm' side is terminated by a set of CF flanges with optical and electrical feedthroughs, while on the 'cold' side is welded to a custom copper flange.

As shown in Fig. 2.2(a), the microscope is bolted to the center of the copper flange which provides the thermal contact with the liquid helium bath as well as an interface to indium seal the probe with the bottom vacuum can. The vacuum in the probe can reach a base pressure of 10^{-7} mbar with a turbo pumping station² and can be maintained at 10^{-6} mbar just by using an ion pump³ to perform measurement at room temperature, thanks to the absence of vibrations in such pumps.

The setup for the optical detection of the nanowire's motion (see Section 2.2.2) is entirely fiber-based (red path in Fig. 2.1). Light from a 35 mW fiber-coupled distributed-feedback diode laser⁴ with $\lambda = 1550$ nm is launched along the slow-axis into one arm of a 95 : 5 polarization maintaining (PM) fiber-optic coupler⁵. The long 5% coupling branch is fed into the probe down to the optical microscope encased in a cylindrical titanium chuck (Fig. 2.3(a)). The 95% coupling branch, instead, can be

¹CRYOMAGNETICS Inc.

⁴TOPTICA DFBpro

²Agilent TPS - Compact

⁵Evanescence Optics 954P

³Agilent VacIon Plus 40

connected to an optical power meter to monitor the power incident on the NW. All the optical fibers used are single-mode.

The light that is scattered from the NW back into the fiber interferes with the one reflected at the fiber/vacuum interface and it is converted into a voltage signal V_{out} by a variable gain (10^2 to 10^8 V/A) and wide bandwidth (up to 200 MHz) photoreceiver⁶. The system is equipped with an additional optical fiber-based setup for a laser light source at $\lambda = 635$ nm, similar to the one just described.

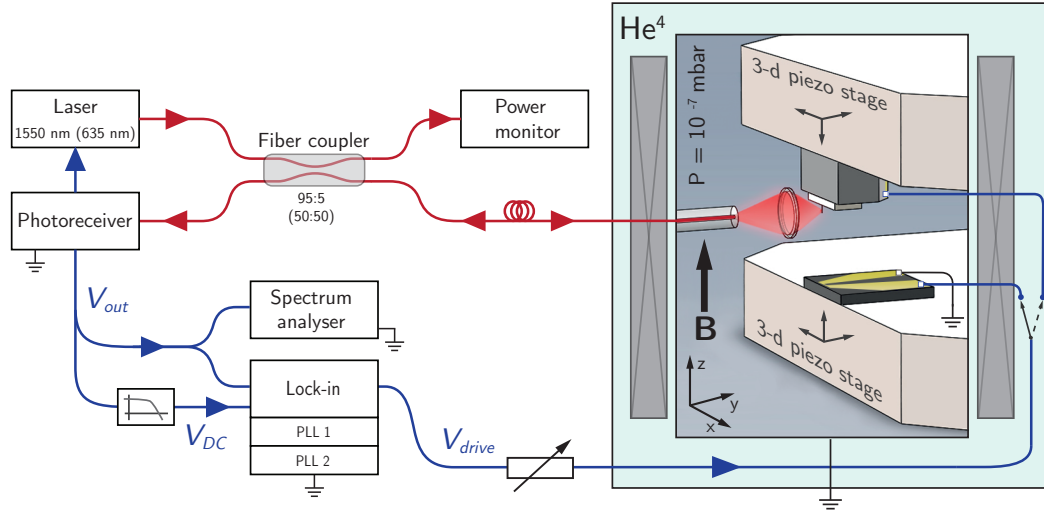


FIGURE 2.1 | **Schematic representation of the measurement setup.**

The photo-receiver signal V_{out} is sent to a fast data acquisition card⁷ to calculate full bandwidth power spectral densities (PSD) and to a lock-in amplifier⁸ to acquire and process the signal around the NW's resonance frequency (i.e. demodulation frequency). The 'DC'-filtered signal V_{DC} is also connected to an auxiliary input of the lock-in and it is streamed to the PC synchronously together with the demodulated signals. The NWs' mechanical resonance is driven by the lock-in oscillators' voltage outputs either via a dither piezo disk located in proximity of the NW's chip, or by modulating other physical quantities which can couple to the NW (e.g. electrostatic forces).

The microscope hangs on 4 beryllium-copper springs (non-magnetic) to further decouple it from vibrations (Fig. 2.2(a)); additionally, 4 soft and loose copper braids, mounted in parallel to the springs, provide proper thermal anchoring as well as damping of the springs' low frequency resonance. The core of the microscope (Fig. 2.2(b)) is fully machined in titanium for its low magnetism and low thermal contraction at cryogenic temperatures. The fiber-based confocal microscope shown in Fig. 2.3(a) is held in place by a dedicated chuck in the middle of the frame. The two stacks of piezo motors are mounted symmetrically with respect to the optical system's axis and allow coarse and fine 3D positioning. The top piezo stack is dedicated to the placement of the NWs in the focused light beam, whereas the bottom one brings the sample under investigation close to the NW's tip and performs the scan (Fig. 2.2(c)). The fine motion of piezo-stacks is controlled from the PC via 3×2 analog voltage

⁶FEMTO OE-300-IN-01

⁷National Instruments PXI-6115

⁸Zurich Instruments UHFLI

⁹Attocube ANPx311

¹⁰Attocube ANSxy100

¹¹Attocube ANPxyz100\lr

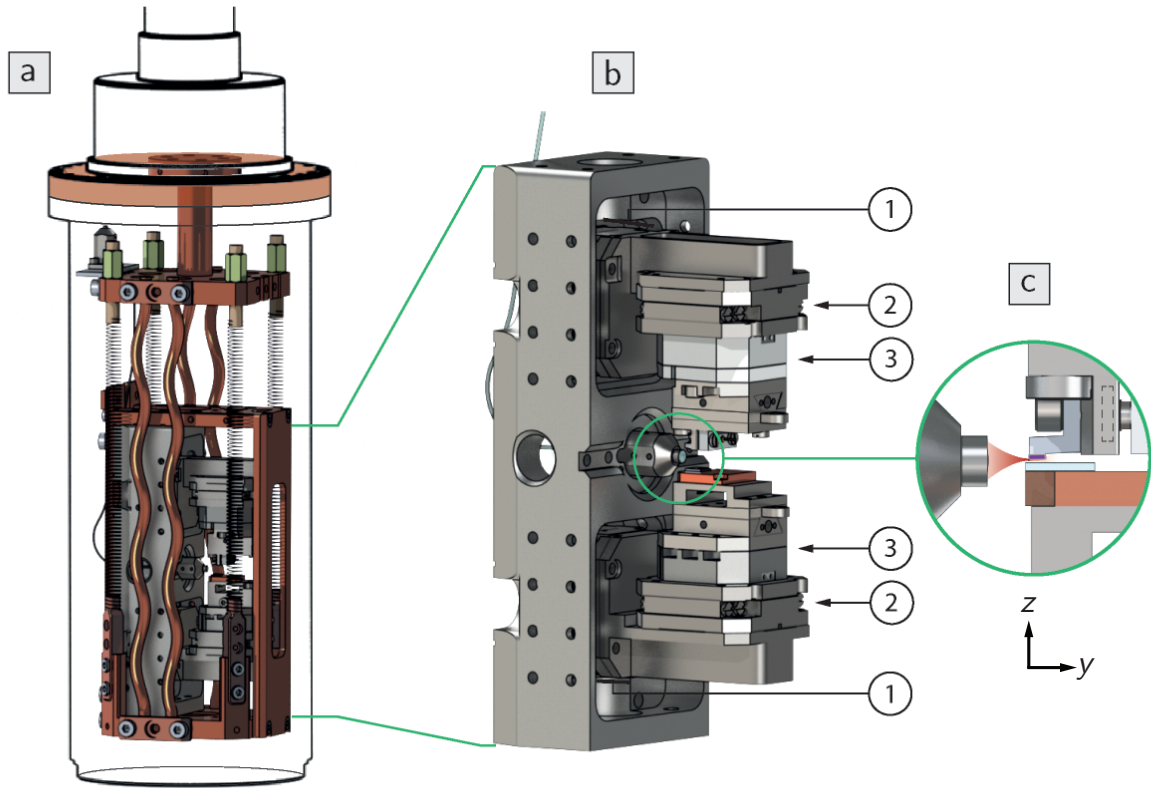


FIGURE 2.2 | **Low temperature nanowire scanning probe microscope.**

3D CAD model of the microscope (actual photographs in Appendix A). (a) Overview of the microscope enclosed in the terminal part of the cryostat probe (sketched by black lines except for the copper flange brown colored).

(b) Titanium central core. Each stack of piezo motors is formed by a y -axis and z -axis linear positioner⁹(stepper) ① connected via an L-shaped mount to a x -axis linear positioner ②. On top of it, a 2D-scanner¹⁰ ③ allows for a $10 \times 10 \mu\text{m}$ (@ 4 K) fine positioning window on the xy -plane. Vertical fine movement is obtained by applying a DC voltage on the z -axis linear positioner, though limited to a small range of $1.75 \mu\text{m}$. Just recently, the top stack scanner has been replaced with a large range xyz -scanner¹¹ $30 \times 30 \times 15 \mu\text{m}$ (@ 4 K) making it possible to image the nanowires for almost their entire length. Both top and bottom samples' supports are designed with a dovetail slide for an easy installation and removal.

(c) Close up on lens(left)/NW(top)/sample(bottom). The NWs' chip on the top stack (in violet) is glued on a L-shaped support with a 2° tilt respect to the xy -plane. Such a tilt is crucial to prevent any unwanted contact against the bottom sample while scanning. A small piezo disk (3 mm diameter 0.5 mm thickness) is mounted just behind the L-shaped holder (its position is indicated by the gray dashed line) to drive the NWs' mechanical resonances.

outputs of a dedicated 16-bits DAQ card¹². The imaging of the NW (top-stack) or of the sample (bottom-stack) can be performed in two modes:

- ... *Point-by-point*: a fine-movement array of 2D coordinates (points) is generated by defining the scan trajectory with a space resolution much higher than the final image for a smoother motion of the piezo. A boolean array of the same size distinguishes between simple movement points (false) and acquisition points (true) forming the final matrix of $m \times n$ points. This mode is indicated if time-consuming measurement routines are performed at each acquisition point, such as thermal noise, static optical gradient or frequency sweeps.
- /// *Line-by-line*: similarly to raster-scan in conventional AFM, each line-scan is sampled at high rate upon a digital trigger, which starts the data acquisition and the analog voltage ramp controlling the ‘fast-axis’ piezo. This mode exploits the functionalities of the Data Acquisition module available for the Zurich Instruments lock-in, which allows to define triggered acquisitions, of user-defined duration, for several quantities such as: tracked frequencies of the NW’s modes (i.e. PLLs control), modes’ oscillation amplitudes (i.e. demodulators R signal) and auxiliary inputs (e.g. DC reflection).

2.2 Motion detection of a nanowire

The motion detection of mechanical resonators represents a key aspect for every force microscopy application. In conventional scanning probe setups, due to the resonator’s dimensions typically ranging from hundreds of microns to few millimeters, the displacement’s readout is mainly carried out either optically by detecting the deflection of a laser beam reflected by the backside of an AFM cantilever [76] or electrically by measuring the piezoelectric signal produced by a resonating quartz tuning fork [77, 78].

Scaling down the dimensions to nano-resonators, a large variety of techniques has been employed to study the mechanical properties of nanobeams, nanowires and nanotubes. In the case of doubly-clamped geometry, the resonator can be directly integrated in an electronic circuit so that its mechanical motion modulates – via capacitive coupling – the frequency of a microwave cavity [79, 80] or the *AC*-current flowing through the beam [17, 81].

More generally, displacement can be probed ‘locally’ by recording the intensity modulation of a focused beam interacting with the resonator: either in form of scattered free electrons using a scanning electron microscope [45, 51, 82] or with a laser measuring the transmitted [22, 71] or reflected [23] optical power. Such methods, despite being compatible with the singly-clamped geometry required in scanning probe applications and ensuring sensitive displacement detection, impose very tight constraints on the setup design.

Conversely, fiber-optic interferometry [15] keeps the design simple, compact and mechanically robust, while still providing very high sensitivity; it has been used with micrometer-scale cantilevers [13] as well as with NWs [24].

2.2.1 Fiber-based confocal reflection microscope

A fiber-optic interferometer is integrated in our cryogenic scanning microscope, encasing the fiber’s terminal part and the lenses in a titanium frame as shown in Fig. 2.3(a).

¹²National Instruments PXI-6733

Given the tiny amount of optical power interacting with the NW, a high numerical aperture (NA) focusing lens is desirable to keep the displacement detection as localized as possible along the NW. The tightly focused spot also maximizes the scattered light collection efficiency [83]. The effective NA of the objective sketched in Fig. 2.3(b) is 0.45 due to the slight mismatch in NAs between the fiber and the collimating lens. Before describing the interferometric technique, it is worth to illustrate the imaging capabilities of our device, which allow for the NWs' sample navigation and beam positioning along the selected NW. The confocal arrangement of the lenses – with the fiber's mode field diameter (MFD) acting as a pinhole – allows for high imaging resolution and optical sectioning. In confocal microscopy, in fact, the final image is constructed by measuring the light's intensity for every scanning position in the plane. The total coherent spread function (CSF) is given by $CSF_{tot} = CSF_{illum} \times CSF_{det}$, where the former term is determined by the field distribution of the focused

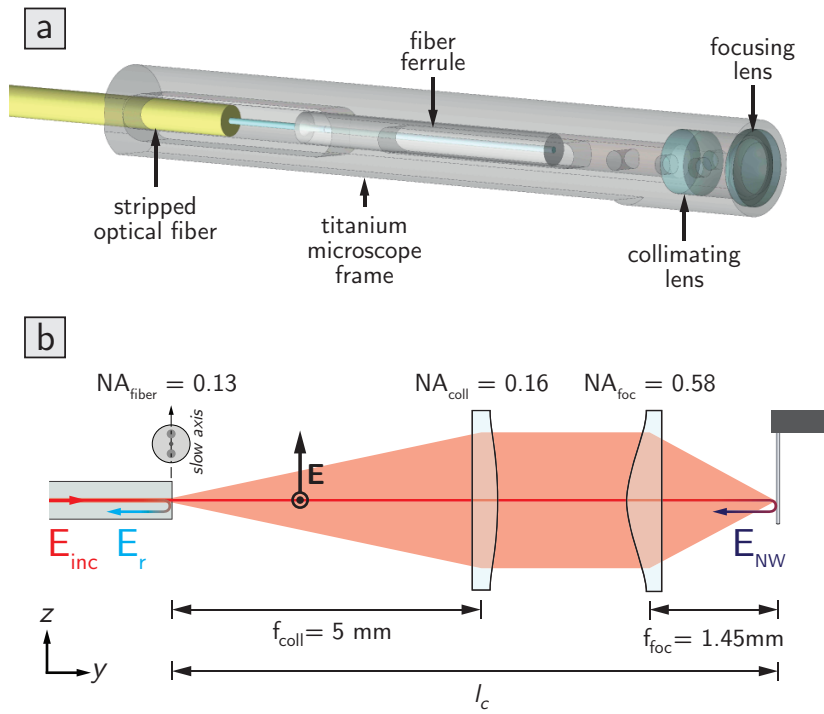


FIGURE 2.3 | **Fiber-based confocal reflection microscopy setup.**

(a) 3D CAD model of the confocal microscope. (b) Sketch of the optical setup. An aspheric lens with an outer diameter of 2 mm and a clear aperture of 1.6 mm is used for beam collimation¹³, while an aspheric lens with an outer diameter of 2.4 mm and a clear aperture of 1.6 mm for focusing¹⁴. \mathbf{E}_{inc} is the incident electric field at the fiber/vacuum interface where a part gets reflected back as \mathbf{E}_r . The transmitted field gets scattered by the NW and partially recollected by the fiber as \mathbf{E}_{NW} . The distance between the fiber's cleaved facet and the NW corresponds to the Fabry-Perot cavity length l_c . The PM fiber is rotated and then fixed to the frame with a drop of epoxy glue on the cladding, in order to align the slow-axis (i.e. E-field axis) parallel to the NW axis.

¹³Thorlabs 354430-C

¹⁴Thorlabs 354140-C

excitation Gaussian beam and the latter by the spatial filtering properties of the pinhole (i.e. fiber's mode field) in the image plane [84].

The intensity map in Fig. 2.4(a) is obtained by scanning the NW in the beam's waist area (xy -plane) and measuring the DC component of the reflected signal on the photo-receiver ($V_{DC}(x, y)$). Such maps show interference fringes superimposed to a typical Gaussian waist profile. The linecut along the x -axis at the focal plane in Fig 2.4(b) allows to directly image the CSF_{tot} itself and to fit it with a Gaussian curve, due

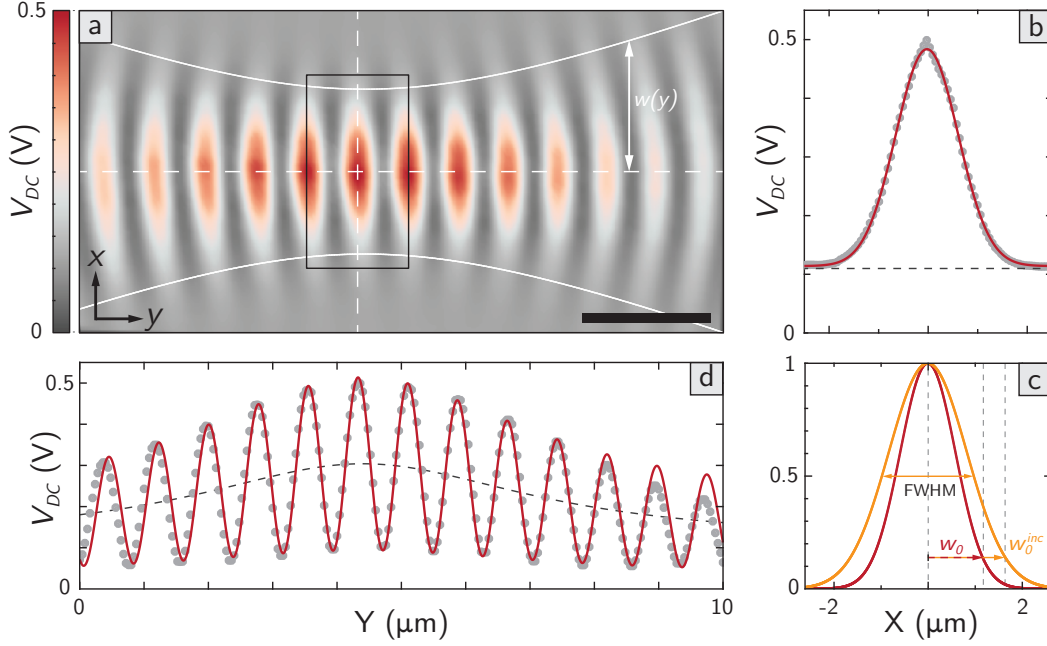


FIGURE 2.4 | **Optical microscope characterization at $\lambda = 1550 \text{ nm}$**

(a) Measured 2D map of the reflected light intensity $V_{DC}(x, y)$ as a function of NW position in the beam's waist, with an incident power of $25 \mu\text{W}$. The plot has been straightened by a clockwise rotation of 2° , due to a small misalignment between the xy -scanners and the optical axis. The white lines show the fitted width $\pm w(y)$ of the detected Gaussian beam. Scale bar $2 \mu\text{m}$. (b) Voltage (i.e. optical power) linecut along the x -axis at the focal plane (dashed vertical line in (a)). The red line fitting the measured points (gray dots) consists of a Gaussian curve summed with a 0.11 V offset (dashed black line), given by the first reflection at the fiber ($\propto |\mathbf{E}_r|^2$). (c) Comparison between CSF_{tot} (red line) and CSF_{illum} (orange line). The CSF_{tot} is taken as the normalized fitted Gaussian profile in (b) and the CSF_{illum} as its squared root. The measured characteristics of the incident laser beam are a waist $w_0^{inc} = 1.65 \mu\text{m}$ – at which the intensity drops by a factor of $1/e^2$ – and a full width at half maximum FWHM = $2 \mu\text{m}$. The waist of the detected beam (CSF_{tot}) is $w_0 = 1.2 \mu\text{m}$. (d) Voltage linecut along the optical axis i.e. y -axis (dashed horizontal line in (a)). The measured data (gray dots) are fitted as the response of a two-component interferometer in Eq. (2.6) (red line). The fitted average voltage (dashed black line) is expressed as the Gaussian beam intensity along the optical axis $V_{avg}(y) = V_0/(1+(y/y_R)^2)$ (Lorentian peak) plus a 0.11 V offset (back-reflection at fiber). The Rayleigh length is $y_R = \pi w_0^2/\lambda = 2.9 \mu\text{m}$. The fringe visibility is $\mathcal{V} = 70\%$ and the highest y -displacement sensitivity, in focus, is $\partial V_{DC}/\partial y = 1.65 \text{ V}/\mu\text{m}$.

to sub-wavelength width of the NW along the scanning direction. The profile of the beam incident on the NW, since in our case illumination and detection CSFs coincide, corresponds to $CSF_{illum} = \sqrt{CSF_{tot}}$ and has a waist $w_0 = 1.65\mu\text{m}$ (see Fig. 2.4(c)). The measured waist is close to the theoretically calculated value of $1.52 \pm 0.15\mu\text{m}$ for a polarization maintaining fiber¹⁵ with MFD = $10.5 \pm 0.5\mu\text{m}$. Deviations in the MFD and diffraction account for the slight magnification measured when defocusing with respect to the collimating lens.

2.2.2 Fiber-optic interferometer

Adopting the notation introduced in the sketch of Fig. 2.3(b), the interferometer response can be treated as a two-component collinear interference between \mathbf{E}_r and \mathbf{E}_{NW} . In fact, due to the poor reflectivity of the NW and fiber's cleaved facet, multiple reflections in such low-finesse cavity can be neglected [15, 85]. The detected voltage output V_{out} of the photo-receiver, proportional to the optical power P_{out} , is given by

$$V_{out} \propto P_{out} = |\mathbf{E}_r|^2 + |\mathbf{E}_{NW}|^2 + 2\text{Re}(\mathbf{E}_r \cdot \mathbf{E}_{NW}) \quad (2.1)$$

where $\mathbf{E}_r = \sqrt{R_f} \mathbf{E}_{inc}$ due to Fresnel reflection, \mathbf{E}_{NW} is the field scattered by the NW and recollected by the fiber, and $\text{Re}(\dots)$ refers to the real part of the quantity in parentheses. The optical reflectivity of the fiber $R_f = P_r/P_{inc} = (n_f - n_v)^2 / (n_f + n_v)^2$ is typically around 3%, being the refractive indexes of the fiber's core and vacuum, $n_f \approx 1.46$ and $n_v = 1$, respectively.

The expression of \mathbf{E}_{NW} as a function of \mathbf{E}_{inc} can be obtained in terms of the detected back-scattered field by the NW in the framework of the Mie theory (Section 1.3) and therefore depends on its optical and geometrical properties in relation with the incident field's wavelength.

A PM panda fiber (see Fig. 2.3(b)) is used to illuminate the NW with TM polarized light, in fact, as shown in Fig. 1.9 and reported in previous works on optical detection of NWs [24], aligning the incident electric field to the NW's axis greatly enhances the scattering efficiency. We consider a TM-polarized focused Gaussian beam $\mathbf{E}^t = E_z^t \hat{\mathbf{z}}$, in paraxial approximation, propagating along the y -axis (i.e. incident normally on the NW). The electric field magnitude transmitted after the fiber on the xy -plane is

$$E_z^t(x, y) = E_{inc} \sqrt{1 - R_f} \frac{w_0}{w(y)} \exp \left[-\frac{x^2}{w^2(y)} \right] \exp [-i\phi(x, y)] \quad (2.2)$$

where the phase $\phi(x, y)$ and the beam width $w(y)$ are determined by the focal length and numerical aperture of the optical setup and are defined as

$$\begin{aligned} w(y) &= w_0 \sqrt{1 + \left(\frac{y}{y_R} \right)^2} \\ \phi(x, y) &= ky + k \frac{x^2}{2y \left[1 + \left(\frac{y}{y_R} \right)^2 \right]} - \tan^{-1} \left(\frac{y}{y_R} \right) \end{aligned} \quad (2.3)$$

where the depth of focus (Rayleigh length) is $y_R = \pi w_0^2 / \lambda$. For $\lambda = 1550\text{ nm}$, in Fig. 2.4 we obtained an incident beam waist $w_0 = 1.65\mu\text{m}$.

In order to make use of the Mie scattering solution in Eq. (1.59), we follow the approach of Kozaki *et al.* [71, 86] to calculate the scattering of a Gaussian beam by

¹⁵PM15-U25D

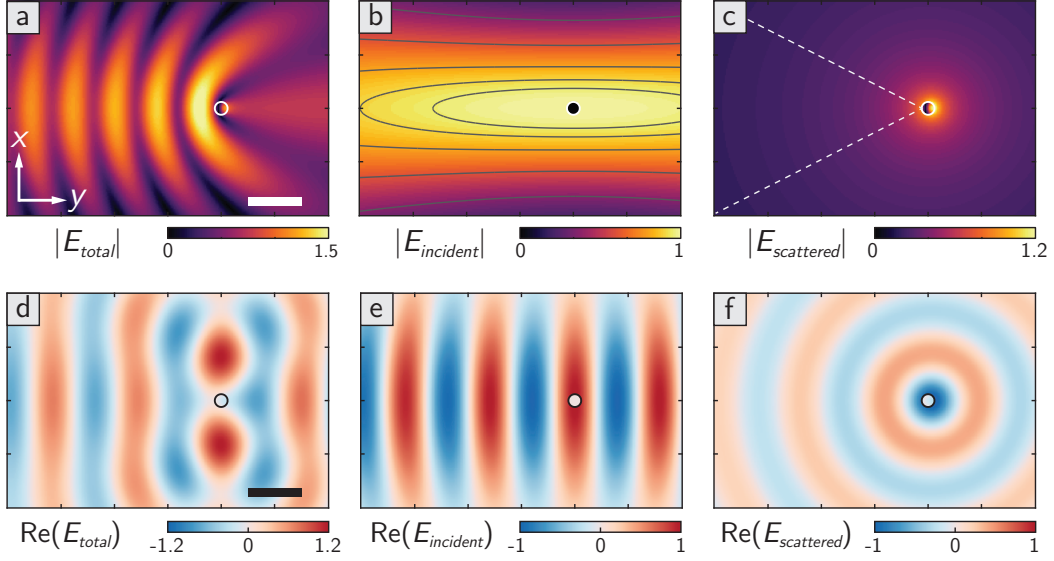


FIGURE 2.5 | **Scattered Gaussian beam by a nanowire**

Calculated magnitude and real part of the total electric field (a,d) for an incident Gaussian beam with $\lambda = 1550$ nm (b,e), scattered by a GaAs NW with $\epsilon_r = 12.9$ and diameter 240 nm (c,f). The circles indicate the NW's position in the focus, while the dashed cone in (c) shows the 54° acceptance angle of the effective NA. Scale bars $1 \mu\text{m}$.

an homogeneous dielectric cylinder, through a planar wave expansion of the incident field in Eq. (2.3). Considering a GaAs NW with a diameter of $d = 240$ nm, Fig. 2.5 shows the calculated total field and its two components: the normalized incident beam and the scattered field. The theoretical result supposes an infinitely long cylinder and therefore is valid along the NW, except for the base and tip of the NW, since w_0 is much smaller than the NW's length. However, at large wavelength with $w_0 \gg d$, the laser spot may be approximated as a simple plane wave with normal incidence $\mathbf{E}_{\text{inc}} \approx E_0 \hat{\mathbf{z}}$. The scattered field at the fiber can be then expressed by integrating the scattered field at the NW propagated over the cavity length and integrated over the effective NA as $\mathbf{E}_{\text{NW}} = \int_{\text{NA}} \mathbf{E}_{\text{scattered}}(l_c, \theta) d\theta$.

Low-finesse Fabry-Pérot interferometer We introduce an effective reflectivity R_{NW} for the NW, which allows us to describe the NW's back-scattered field as $\mathbf{E}_{\text{NW}} = (1 - R_f) \sqrt{R_{\text{NW}}} \mathbf{E}_{\text{inc}}$, reducing Eq. (2.1) to the standard expression for conventional cantilevers [34]:

$$P_{\text{out}} = E_{\text{inc}}^2 \left[R_f + (1 - R_f)^2 R_{\text{NW}} + 2\sqrt{R_f R_{\text{NW}}} (1 - R_f) \Re \left(e^{i \frac{2\pi}{\lambda} 2l_c} \right) \right] \approx \quad (2.4)$$

$$\approx E_{\text{inc}}^2 \left[R_f + R_{\text{NW}} + 2\sqrt{R_f R_{\text{NW}}} \cos \left(2\pi \frac{2l_c}{\lambda} \right) \right] \quad (2.5)$$

where l_c is the cavity length (see Fig. 2.3(b)), e^{iky} is the relative phase picked up by the second component on the path fiber-NW and back (i.e. $k = 2\pi/\lambda$ and $y = 2l_c$). The approximated expression (2.5) neglects second order terms in reflectivity, since $R_f, R_{\text{NW}} \ll 1$.

In Fig. 2.4(d), the cavity is scanned by moving the NW along the optical axis (i.e. y -axis) through the focal point. The measured output voltage can be described by

Eq. (2.5), which can be reformulated by defining an average envelope term $P_{avg} = E_{inc}^2(R_f + R_{NW})$ and a fringe amplitude term $P_{amp} = 2E_{inc}^2\sqrt{R_f R_{NW}}$

$$P_{out}(y) \propto V(y) = V_{avg}(y) \left[1 - \mathcal{V} \cos \left(2\pi \frac{2y}{\lambda} \right) \right] \quad (2.6)$$

where the fringes have period $\lambda/2$ and the interferometer's *visibility* is

$$\mathcal{V} = \frac{P_{amp}}{P_{avg}} = \frac{2\sqrt{R_f R_{NW}}}{R_f + R_{NW}} = \frac{\frac{1}{2}(V_{max} - V_{min})}{\frac{1}{2}(V_{max} + V_{min})} \quad (2.7)$$

For all the NWs studied, with diameters ranging from 200 to 400 nm, the measured fringe visibility was above 65% up to 90%. This high interference contrast indicates that $R_{NW} \approx R_f$, meaning that the optical power P_{NW} , scattered at the NW and guided back into the fiber's core, is close to 3% of the power incident on the NW i.e. $(1 - R_f)P_{inc}$.

The cavity length is set by the position of the NW y_0 and modulated by the projection of its vibrations along the y -direction, $\delta y(t)$. Evaluating Eq. (2.6) for $y = y_0 + \delta y(t)$, the maximum sensitivity to the oscillations $\delta y(t)$ is obtained at quadrature for $y_0 = \frac{\lambda}{8} + n\frac{\lambda}{4}$, $n \in \mathbb{Z}$. At these optimal positions, the interferometer response is linearized around V_{avg} (for $\delta y \ll \lambda/4$) with a displacement sensitivity

$$\left. \frac{dV}{dy} \right|_{y=y_0} = \pm \frac{4\pi}{\lambda} V_{avg} \mathcal{V} = \pm \frac{2\pi}{\lambda} (V_{max} - V_{min}) \quad (2.8)$$

which gives a precise voltage-to-displacement conversion factor, only limited by uncertainties on λ and on V_{avg} (i.e. set-point position). Eq. (2.8) also shows that the sensitivity can be optimized both by simply increasing the laser power (P_{avg}), which ultimately causes the heating of the resonator, and by optimizing the fringe visibility close to its maximum value $\mathcal{V}_{max} = 1$, achieved for $R_{NW} = R_f \sim 3\%$. More generally, P_{avg} is maximized by always positioning the NW in focus, while the 'working-point' on the linear region of the fringe is set by tuning the laser wavelength to shift accordingly the interference pattern. As shown in Fig. 2.6, the wavelength is tuned by changing the operating temperature set-point of the laser diode, which is stabilized by thermoelectric Peltier elements (TEC). For our DFB laser at 1550 nm the emission wavelength shifts 0.099 nm/K. The interferometer response to a λ sweep has a period called *free spectral range* (FSR) of 0.12 nm. The measurement of the FSR allows to precisely calculate the cavity length as

$$l_c = \frac{\lambda^2}{2n_v \text{FSR}} \quad (2.9)$$

which returns $l_c = 9.2$ mm. Due to the laser's coherence length of several meters, the scan presents a faint modulation at higher frequency, which indicates the presence of much a larger cavity of about 2.25 m corresponding to the fiber optical path up to the photo-detector. These unwanted resonances are suppressed by using PM fiber pigtailed isolators¹⁶ on the return path to the photo-detector and/or by shortening the coherence length via modulation of the laser current (RF tone at few MHz or broadband white noise).

¹⁶Thorlabs IO-G-1550

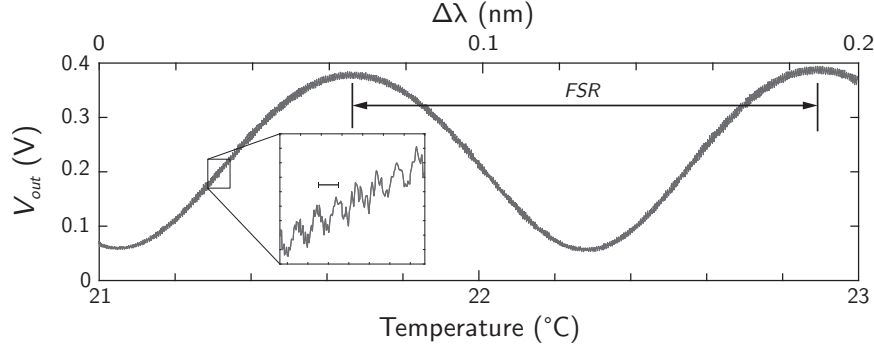


FIGURE 2.6 | **Wavelength/temperature cavity scan**

Cavity scan by detuning the laser nominal wavelength $\lambda = 1550$ over a 2°C temperature sweep around room temperature. $\text{FSR}' = 120$ pm. Inset: zoomed region. The very small amplitude of the spurious oscillation indicates a large reflectivity mismatch between the reflecting surfaces involved. $\text{FSR} = 0.5$ pm.

The fringe can be locked to its optimal value P_{avg} to compensate for possible time-drift of wavelength and cavity length (i.e. NW position), by means of a proportional-integral-derivative (PID) controller implemented in the laser controller unit¹⁷. The photo-receiver voltage is kept at the set-point via laser wavelength adjustment, both by controlling temperature (slow drifts) and laser current (fast transients). Finally, cavity effects are excluded since the same quality factor is always obtained whether the measurement is performed on the positive (red-shifted) or negative (blue-shifted) side of the interferometer fringe.

2.2.3 Displacement calibration and 2D angular mapping

Given the peculiar 2D nature of the oscillations in NWs, it is important to generalize the interferometric technique of motion detection, described in the previous section. In the V_{DC} map of Fig. 2.4(a), for each direction the intensity is varying on a much larger scale compared to the typical NW displacements of few nanometers at most. For this reason, it is always possible to linearize the interferometer response at every position $\mathbf{x}_{NW} = [x_0, y_0, z_0]^T$ and extend the expression of motion detection sensitivity in Eq. (2.8) to

$$\|\nabla V_{DC}(\mathbf{x}_{NW})\| \quad \text{with} \quad \mathbf{e}_\beta = \frac{\nabla V_{DC}(\mathbf{x}_{NW})}{\|\nabla V_{DC}(\mathbf{x}_{NW})\|} \quad (2.10)$$

The unit vector \mathbf{e}_β indicates the direction along which the NW's modes motion is projected. It forms an angle β_0 with the microscope's optical axis which is collinear with the y -axis of the piezo scanner. The direction of the first mode is rotated by an angle β respect to the measurement vector, i.e. $\mathbf{e}_\beta \cdot \hat{\mathbf{r}}_1 = \cos \beta$.

When the NW is positioned on the optical axis, Eq. (2.10) reduces to Eq. (2.8) and therefore $\mathbf{e}_\beta = \pm \hat{\mathbf{y}}$ (i.e. $\beta_0 = 0$). In this case, the measurement is totally insensitive to the motion along the x -direction (i.e. $\partial V_{DC}/\partial x = 0$) and the detection sensitivity

¹⁷TOPTICA DLC pro

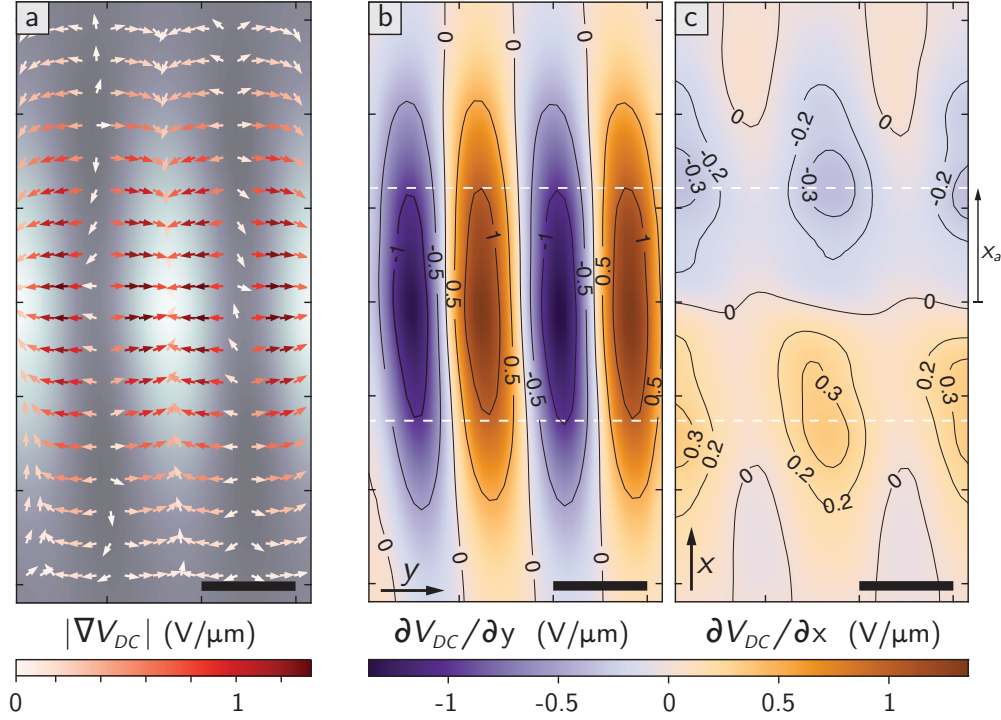


FIGURE 2.7 | **Measurement vectors and displacement sensitivity maps**

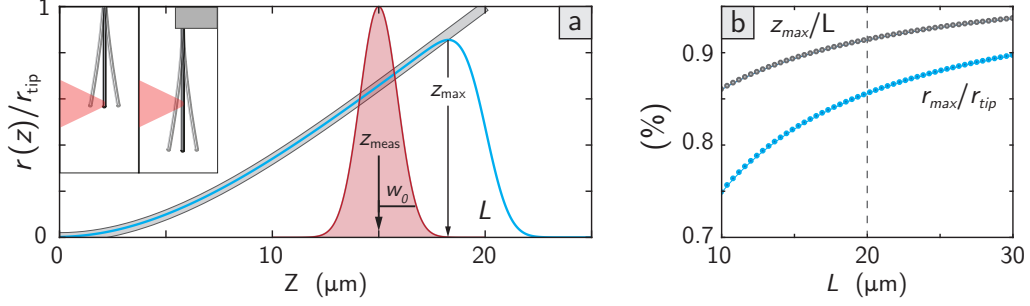
(a) Measurement vectors sampled over a two fringes region (black boxed area of Fig. 2.4(a)). The measurement sensitivity (i.e. vectors' magnitude) is color-coded. (b,c) Maps for the gradient's y - and x -component, scaled evenly to highlight the difference in detection efficiency for the two directions. White dashed lines at $x = \pm x_a$ indicate the optimal offset from the optical axis which allows to change the measurement angle β_0 just by moving along y . Scale bars 500 nm.

is maximum (optimizing y_0); typically on the order of units of V/μm for few tens of μW of incident power.

Fig. 2.7(a) shows the calculated gradient field (i.e. measurement vectors) for a reduced region of the voltage map in Fig. 2.4(a) (black boxed area). The map of the gradient's y -component in Fig. 2.7(b) confirms how the presence of the interference pattern enhances the detection sensitivity along the optical axis. Nevertheless, by displacing the NW off-axis, it is possible to rotate the measurement vector to probe the x -component of the NW's motion at the price of a reduced sensitivity (3 to 4 times worse), as displayed in Fig. 2.7(c).

Another important practical aspect concerns the estimation of the modes' amplitude of motion r_i , which is intended as the displacement at the NW's tip. Despite the detected spot size has a waist of $w_0 \sim 1.25 \mu\text{m}$ (see Fig. 2.4(c)), which is smaller than the NWs length, the measurement of the displacement is not exactly punctual, but is averaged over a Gaussian profile along the NW's length. In Fig. 2.9(a) the mode shape $u_0(z)$ is compared to the normalized measured displacement r_{meas} , modeled as a function of the Gaussian beam's position along the NW

$$r_{meas}(z_{meas}) = \frac{1}{\sqrt{w_0^2 \pi}} \int u_0(z) \exp\left(-\frac{(z - z_{meas})^2}{w_0^2}\right) dz \quad (2.11)$$

FIGURE 2.8 | **Tip displacement calibration**

(a) Calculated plot of the first mode displacement profile $u_0(z)$ (gray line) probed with a focus laser beam of waist $w_0 \sim 1.25 \mu\text{m}$ (red curve) at each position z_{meas} along the NW's axis (blue line). Such curve can be obtained by driving one of the modes on resonance and recording the induced displacement at its resonance frequency for each point [24]. (b) Relative position (gray points) and magnitude (blue dots) of the signal maximum value, for typical NW lengths. The dashed gray line indicates the case plotted in (a). For longer NWs with $L \gg w_0$, the measured displacement curve approaches u_0 , as in the punctual readout limit case.

The spatial extent of the laser spot, causes the signal to be maximum at $z_{\text{max}} < L$, which depends on the NW's length L . The coefficient $r_{\text{max}}/r_{\text{tip}} \approx u_0(z_{\text{max}})$ in Fig. 2.9(b) can be used to convert the maximum measured motion at z_{max} into the real motion at the tip, which is crucial to correctly estimate the effective mass M . In alternative, the tip height $z = L$ can be located by acquiring a V_{DC} map in the plane coplanar to the NW (ideally xz -plane), and deconvolving the intensity linecut along the NW's axis with the laser Gaussian spot. The measurement of the NW motion exactly at the tip, though, suffers from low SNR due to a poor displacement sensitivity. Knowing the position along the NW, the tip's motion is given by $r_{\text{tip}} = r_{\text{meas}}/u_0(z_{\text{meas}})$ and the photo-receiver voltage PSD $S_V(\omega)$ can be converted into the displacement noise PSD in Eq. (1.49) as

$$S_{\delta r_\beta}(\omega) = \frac{S_V(\omega)|_{z=z_{\text{meas}}}}{\|\nabla V_{DC}(\mathbf{x}_{NW})\|^2 u_0^2(z_{\text{meas}})} = \cos^2 \beta S_{\delta r_1}(\omega) + \sin^2 \beta S_{\delta r_2}(\omega) \quad (2.12)$$

It is important to remark that the factor $u_0^{-2}(z)$ rescales the effective mass to its nominal value M (see Eq. (1.20)) and requires a proper estimation of the measurement position. This term contributes, together with the effective temperature T and mass M in Eq. (1.49), to the overall amplitude of the two Lorentians peaks and therefore only one of them can be set as fit parameter. However, the thermal noise PSD can be acquired for different positions along the NW to extract M , which is constant and depends on the NW's geometry and material properties, and for different laser powers, to fit the NW's temperature T , highlighting any possible deviation from the thermal bath temperature.

Finally, in a scanning application, a NW sensor presents additional challenges and constraints. The scanned sample at the bottom should not cut-off the laser beam's power once approached to the NW nor modulate it while moving. At the same time, the NW's deflection amplitude reduces as one moves from its tip towards its clamping point. Given these two competing requirements, the 'measurement-point'

on the NW has to be ensure a good SNR, while being far enough from the sample. Once temperature and effective mass have been estimated, Eq. (2.12) can be used to fit the distance of the detection point from the NW's tip.

Static and dynamical measurement of the local gradient In order to calibrate the voltage-to-displacement gain and the direction of the motion's projective measurement of Eq. (2.10), we use two alternative methods to estimate the gradient of the reflected optical power at the NW's rest position \mathbf{x}_{NW} :

Static mode – Fig. 2.9(a) – the voltage-position map $V_{DC}(x, y)$ is averaged and acquired on a grid of $1 + 8$ points around the rest position (x_0, y_0) . The data are interpolated by a second order polynomial, which is then used to analytically calculate the local gradient's magnitude and angle respect to $\hat{\mathbf{y}}$. The spacings between the grid's points, dx and dy , are chosen in relation with the signal's typical variation lengths in the two directions ($dx = 20$ nm, $dy = 10$ nm).

Dynamic mode – Fig. 2.9(b) – the NW's position is oscillated at low-frequency ($f_{mod} < 70$ Hz) on an ellipsoidal trajectory $x(t) = x_0 + A_x \sin(\omega_{mod} t)$ and $y(t) = y_0 + A_y \cos(\omega_{mod} t)$, by modulating the x - and y -piezo control voltage in quadrature. The reflected signal is demodulated with a lock-in amplifier using an external reference synchronized with the in-phase component X (y -piezo voltage). Being the in-phase (X) and quadrature (Y) signals associated to the detected motion along y - and x -direction, respectively, the gradient can

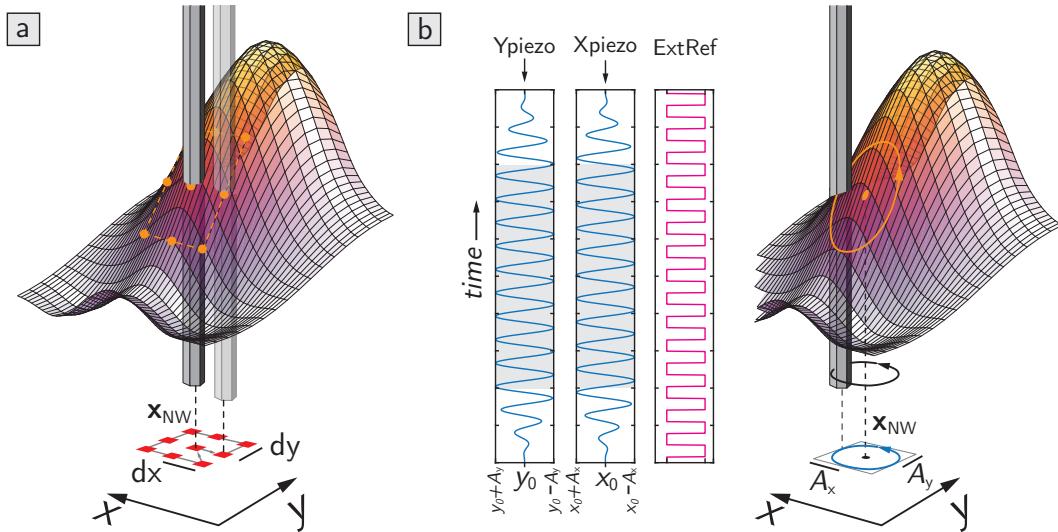


FIGURE 2.9 | **Static and dynamic optical gradient measurement**

The sketches are not properly scaled for the sake of clarity. (a) Static mode. (b) Dynamic mode. Two analog waveforms synchronized to a digital TTL reference are generated by the DAQ-card and sent out on the DC-in inputs of the piezo xy axes controller and to the lock-in external reference input, respectively. The windowing of the two sinusoidal signals ensures a smooth transition to and from the limit cycle. The demodulated signals are averaged over the duration indicated by the gray region.

be calculated as

$$\|\nabla V_{DC}(\mathbf{x}_{NW})\| = \sqrt{\left(\frac{X}{A_y/\sqrt{2}}\right)^2 + \left(\frac{Y}{A_x/\sqrt{2}}\right)^2} \quad (2.13)$$

$$\beta_0 = \tan^{-1}\left(\frac{Y}{X} \frac{A_y}{A_x}\right) \quad (2.14)$$

for a circular trajectory ($A = A_y = A_x$), by using the polar representation (R, ϕ) it reduces to $R/(A/\sqrt{2})$ and $\beta_0 = \phi$, respectively. This mode results to be much faster and robust than the static method. The main limitation is set by the low bandwidth of the piezo scanners; in fact, at constant displacements A_x and A_y (typically ~ 20 nm), the measured gradient magnitude starts decreasing for $f_{mod} > 70$ Hz.

Note that both methods depend on a previous calibration of the piezo scanners displacement. Exploiting the interferometric signal, we can precisely calibrate the displacement of the y -scanner (see Fig. 2.4(d)), while assuming the same conversion factor for the x -scanner.

2D thermal noise map and orthogonality of the modes To perform an angular scan of the NW's displacement [22], it is possible to find an optimal x -offset $x = \pm x_a$, which allows to span the angles $\beta_0 \in [0, \pm\pi]$, by moving the NW across a single fringe ($\sim \lambda/2$), and ensures a good read-out of the motion at each angle. In Fig. 2.10 is reported a complete 2D map of the thermally driven motion of a GaAs NW, which provides a direct proof for the orthogonality of modes' oscillation directions.

In practice, it is possible to extract independently the orientation of each mode respect to the optical axis by acquiring just two projective measurements along non-collinear measurement vectors $\mathbf{e}_{\beta'}, \mathbf{e}_{\beta''}$. For each mode, its orientation can be expressed as a function of the projected power of the relative Lorentian peak along each measurement direction and the angle difference $\Delta\beta_0 = \beta'_0 - \beta''_0$.

As described in Chapter 3, in the case of a NW interacting with an external non-conservative force field the modes' orthogonality is not preserved. This behavior has been shown in the context of strong optical forces acting on a NW being scanned in a tightly confined laser focal waist [22, 87]. These experiments benefit from a free-space optical setup and use a two quadrant photodiode to obtain two signals (sum and difference of voltage of quadrants) with distinct gradient maps of the detected optical power. Hence, by properly positioning in the focal waist, projected thermal noise spectra along two orthogonal directions can be simultaneous acquired.

Conversely, in our cryogenic setup, due to the fiber-based structure of the optical detection system, we rely on a single measurement channel and such simultaneous measurements are not accessible [88]. In analogy with Fig. 2.10, probing the NW's motion at two distinct position of the NW in the focal waist (e.g. $(x_a, 0)$ and $(x_a, \lambda/4)$) is a possible solution, although not feasible for scanning applications, since it requires preserving the relative positioning of the NW with respect to the bottom sample. A better protocol consists of measuring the motion at two slightly detuned laser wavelengths, leaving the NW at $(x_a, 0)$.

In the following, for practical reasons, we use the NW as a scanning probe at fixed wavelength assuming that the eigenmode orthogonality is preserved. To maximize the motion detection sensitivity, the NW is generally positioned on the optical axis at the point of highest gradient. Finally note that, due to the projective nature of the

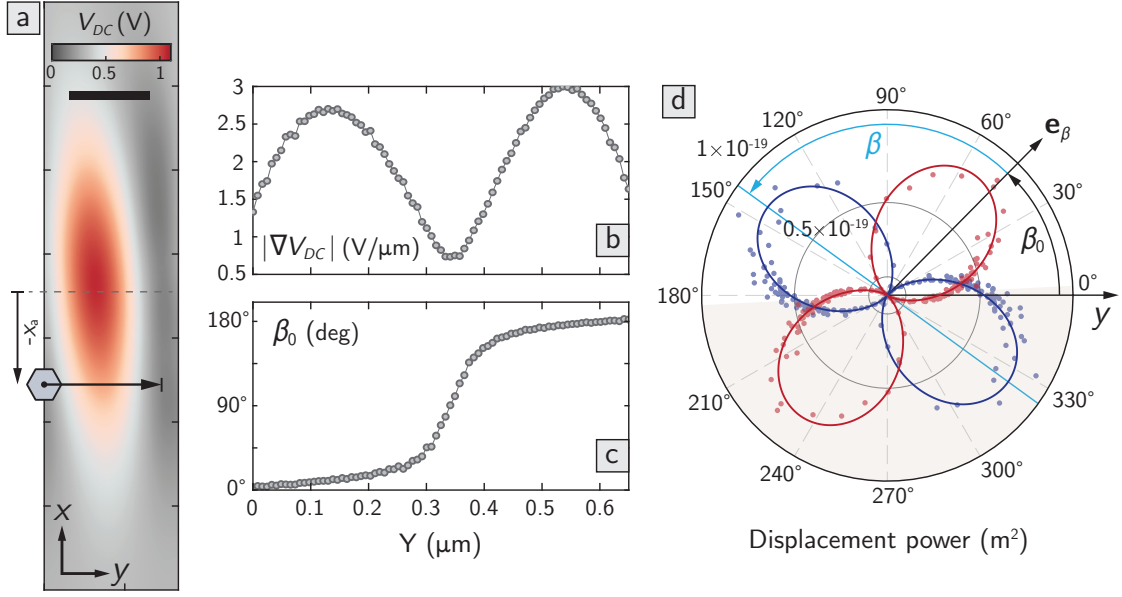


FIGURE 2.10 | **Angular displacement power map**

(a) Voltage map around one single fringe for an incident optical power of $60 \mu\text{W}$. Scale bar 500 nm. After a numerical evaluation of the map's gradient, the NW is placed at $x_0 \approx -x_a$ and line-scanned over a distance $\Delta y = 650 \text{ nm}$ to obtain a smooth rotation of \mathbf{e}_β from $\beta_0 = 0$ to π . (b) Magnitude and (c) direction of the local voltage spatial gradient, at each point of the line scan, measured with the static method illustrated in Fig. 2.9(a). Note that, due to a small misalignment between xy -scanner and optical axis, the gain is maximum (minimum) slightly above $\beta_0 = 0$ ($\pi/2$). The transition from $\beta_0 = 0$ to π in (c) becomes more and more steep for x_0 approaching $x = 0$, increasing the error in the measurement of the gradient direction. Conversely, for $|x_o| \gg |x_a|$ the sensitivity drops, lowering the SNR and introducing an error in the voltage-to-displacement conversion. (d) Plot of the first (blue dots) and second (red dots) mode's displacement power projection on \mathbf{e}_β , as a function of the measurement angle β_0 . At each point the power is calibrated with the gain in (b). After subtracting the background noise, the two datasets are fitted by $P \cos^2(\beta_0 - \beta)$ and $P \sin^2(\beta_0 - \beta)$, respectively, with $P = 8.1 \times 10^{-20}$ and $\alpha = 144^\circ$ as fit parameters. The angle α is the direction of the first mode respect to \mathbf{e}_β and the returned values by the two fits differ by less than 1° confirming the orthogonality of the modes' polarization. The points in the shadowed region have been mirrored to obtain a full 2π representation.

measurement, the modes' orientation respect to \mathbf{e}_β is not univocally determined by a single measurement, since the result is equivalent for $\pm\beta$. However, the real mode directions can be established by comparing the oscillation amplitudes obtained at different β_0 or can emerge from the orientation of features in AFM-like scans realized by using the NW as a force probe (see Fig. 3.4).

Chapter 3

Vectorial scanning force microscopy using a nanowire sensor

3.1 Introduction

Atomic force microscopy (AFM) [4, 89] is a well established microscopy technique existing in several forms and is nowadays routinely used to image a wide variety of surfaces, even with atomic [90] or sub-atomic resolution [5]. Variations on the basic technique, including contact and non-contact modes, allow its application under diverse conditions and with enhanced contrast for specific target signals. Typically, the ‘atomic’-force probes are top-down fabricated silicon cantilevers (hundreds of μm long, tens of μm wide and few μm thick) or functionalized quartz tuning forks. In both cases, the spatial resolution is prioritized over the force sensitivity, since the tip oscillates very close to the surface where strong short-range forces dominate.

Conversely, in recent years, researchers have developed new types of mechanical force transducers, fabricated by bottom-up processes [91]. Prominent examples include doubly-clamped carbon nanotubes (CNTs) [81], suspended graphene sheets [92], and NW cantilevers [24, 32, 93–95]. Assembly from the bottom up allows for structures with extremely small masses and low defect densities. Small motional mass and high structural quality result in high mechanical resonance frequencies, which decouple the resonators from common sources of noise, while low mechanical dissipation enables high thermally-limited force sensitivity. As opposed to extreme aspect ratios and ultra-soft spring constants of CNTs and graphene resonators, NWs are ideal candidates for scanning probe applications. If arranged in the pendulum geometry, i.e. with their long axis perpendicular to the sample surface, NWs are well-suited as scanning probes, with their orientation preventing the tip from snapping into contact [11]. When approached to a surface, NWs experience extremely low non-contact friction making possible near-surface ($< 100\text{ nm}$) force sensitivities around $1\text{ aN}/\sqrt{\text{Hz}}$ [29]. As a result, NWs have been used as force transducers in nuclear magnetic resonance force microscopy [96] and may be amenable to other ultra-sensitive microscopies such as Kelvin probe force microscopy [97] or for the spectroscopy of small friction forces [27]. Furthermore, their highly symmetric cross-section results in orthogonal flexural mode doublets that are nearly degenerate [24, 32]. In the pendulum geometry, these modes can be used for the simultaneous detection of in-plane forces and spatial force derivatives along two orthogonal directions [22]. In contrast with conventional AFM, where 1D dynamic lateral force microscopy can be carried out using the cantilever’s torsional mode at the price of a high mode stiffness [98–102], the ability to simultaneously image with high sensitivity all vectorial components of nanoscale force fields is of great interest. Not only this would provide more information on tip-sample interactions, but it would also enable the investigation of inherently 2D effects, such as the anisotropy

or non-conservative character of specific interaction forces.

In this chapter, we use an individual as-grown NW to realize the vectorial scanning force microscopy of a patterned surface. By monitoring the NW's first-order flexural mode doublet, we fully determine the magnitude and direction of the static tip-sample force derivatives in the 2D scanning plane. Moreover, we characterize the electrostatic interaction by dynamically probing the force field generated by voltages applied to a sample with multi-edged gate electrodes and we identify the contributions of NW spurious surface charge and polarizability to tip-sample interactions. Finally, we exploit such electrostatic interaction to strongly couple the NW's mechanical modes and study their coherent dynamic.

3.2 Nanowire sensor and setup

The NWs used in this experiment have been fabricated via MBE, by the group of Prof. A. Fontcuberta at EPFL, according to the process described previously in Section 1.4.1. More specifically, a GaAs 290-nm-thick core is grown on a Si(111) substrate, by the Ga-assisted method detailed in *Uccelli et al.* [103] and *Russo-Averchi et al.* [104]. Axial growth is stopped once the NWs are about 25 μm long by temporarily blocking the Ga flux and reducing the substrate temperature from 630°C down to 465°C. Finally, a 50-nm-thick $\text{Al}_{0.51}\text{Ga}_{0.49}\text{As}$ shell is radially grown, capped by a 5 nm GaAs passivation layer to prevent oxidation and reduce surface charge density [105]. The radial layering of these NWs as well as their hexagonal cross-section are clearly visible in Fig. 3.1(a).

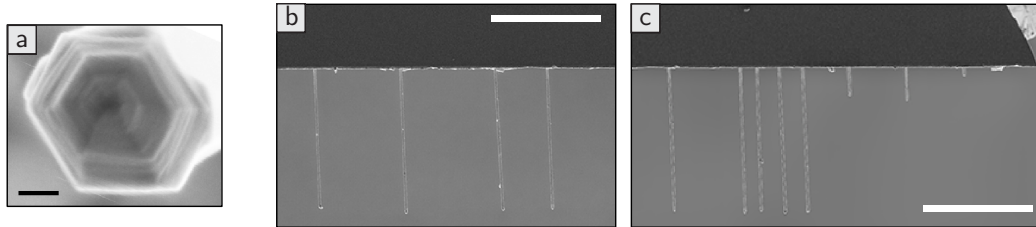


FIGURE 3.1 | **Array of GaAs/AlGaAs core-shell nanowires.**

(a) SEM close-up view of a FIB milled NW's cross-section. Scale bar 100 nm. (b,c) SEM micrographs of the NW cantilevers' chip installed in the microscope. The sharp cleaved edge of Si helps in the focusing and navigation of the sample. Scale bars 10 μm .

A small Si chip was cleaved from the original growth wafer and processed following the procedure detailed in Appendix B. In Figs. 3.1(b,c) are shown two SEM micrographs from the resulting array of NW cantilevers. In the measurements presented below, we use two individual NWs: NW1 and NW2, however, similar results could be obtained from several other NWs.

The experimental setup allows us to determine optically the mechanical characteristics of each NW: light from a laser diode with wavelength of 635 nm is sent through one arm of a 50:50 fiber-optic coupler and focused by a pair of lenses to a $\sim 1 \mu\text{m}$ spot. As reported in Section 2.1, the system has been only afterwards equipped with an equivalent infrared 1550 nm detection setup in order to trade spatial resolution (wider spot size) for lower power absorption.

However, the incident power of around $5 \mu\text{W}$ does not significantly heat the NWs as confirmed by measurements of laser power dependence and by the values of effective masses obtained from the fits $M = M_{\text{tot}}/4 \sim 3.25 \times 10^{-15} \text{ kg}$ which are in good agreement with the mass calculated from geometry and nominal densities¹ $\rho_{\text{GaAs}} = 5320 \text{ kg/m}^3$ and $\rho_{\text{Al}_{0.49}\text{Ga}_{0.51}\text{As}} = 4525 \text{ kg/m}^3$.

These mechanical parameters yield dissipations and force sensitivities (Eq. (1.53)) very close to 100 pg/s and $5 \text{ aN Hz}^{-1/2}$, respectively. Figs. 3.2 and 3.3 show the calibrated noise spectra for NW1 and NW2, respectively. For each measurement, the NW is always centered in the focal waist and positioned such that the optical gradient is maximum in order to maximize the detection sensitivity. As a consequence, the measurement direction \mathbf{e}_β is aligned with the optical axis (i.e. y -axis).

In general, resonance frequencies range from 350 to 450 kHz and the average frequency splitting of the modes' doublet is several hundred times the peak line width, given the high quality factors Q_i in the order of 50000 at 4.2 K. As pointed out in Section 1.1.2, the net splitting of the resonance peaks is enhanced for shorter resonators in length. Nevertheless, the difference is still hundreds of times smaller than the resonant frequencies, guaranteeing practically identical sensitivity for both mechanical polarizations.

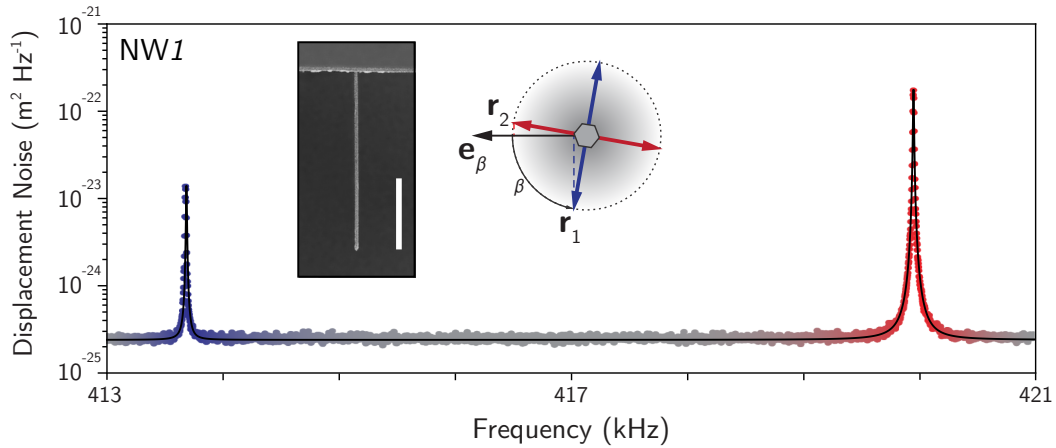


FIGURE 3.2 | **Displacement noise spectrum of core/shell GaAs/AlGaAs NW1.**

PSD of NW1 displacement noise measured with an incident optical power of $5 \mu\text{W}$. The raw data points are fitted by the black line. The extracted resonance frequency, spring constant, and intrinsic quality factor of the first (second) mode are $f_1 = 414 \text{ kHz}$, $k_1 = 25 \text{ mN/m}$ and $Q_1 = 50580$ ($f_2 = 420 \text{ kHz}$, $k_2 = 26 \text{ mN/m}$ and $Q_2 = 50373$). The first mode is rotated by an angle $\beta = 75^\circ$ respect to the measurement direction. Inset: SEM micrographs with scale bar $10 \mu\text{m}$.

¹Density $\text{Al}_x\text{Ga}_{1-x}\text{As}$: $5.32 - 1.56x \text{ g/cm}^3$

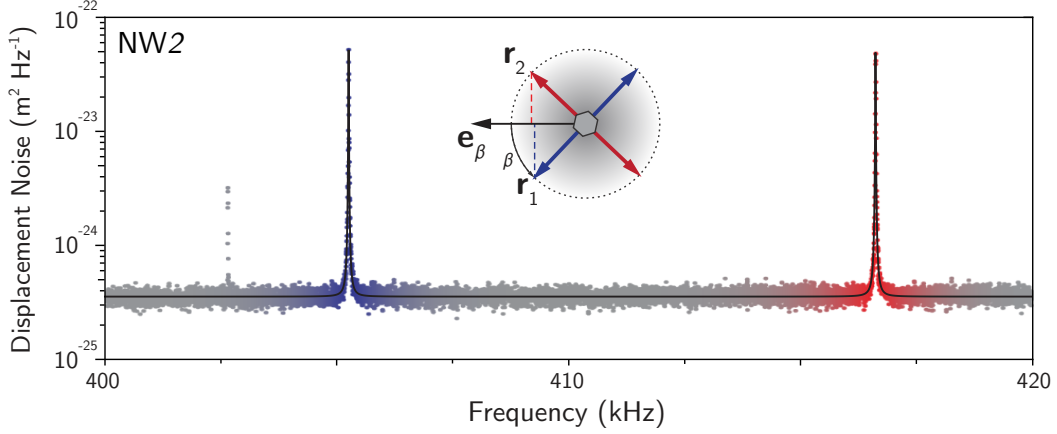


FIGURE 3.3 | **Displacement noise spectrum of core/shell GaAs/AlGaAs NW2.**

PSD of NW2 displacement noise measured with an incident optical power of $5 \mu\text{W}$. Each mode is rotated by a similar angle ($\beta = 46.5^\circ$) respect to \mathbf{e}_β . As a consequence, the measured peaks' power of the projected Brownian motion is almost equal. The extracted resonance frequency, spring constant, and intrinsic quality factor of the first (second) mode are $f_1 = 405 \text{ kHz}$, $k_1 = 35 \text{ mN/m}$ and $Q_1 = 47360$ ($f_2 = 416.6 \text{ kHz}$, $k_2 = 36 \text{ mN/m}$ and $Q_2 = 43855$).

3.3 Nanowire-sample interaction

To use the NW as a scanning probe, we approach the sample and scan it in a plane below the NW tip. By monitoring the mechanical properties of the NW — that is, the frequency, dissipation and orientation of its doublet modes — we map the tip-sample interaction. Such microscopy can be accomplished by measuring the NW thermal displacement spectral density as the sample surface is scanned below it. Although, as it will be shown later on, this measurement provides a full mechanical characterization of the modes, it is time-consuming due to long averaging of the Brownian motion at each point.

Conversely, a technique that is more amenable to a fast spatial scan of the sample topography, uses the resonant excitation of the doublet modes through two independent phase-locked loops (PLL) to track both frequencies simultaneously.

3.3.1 Bi-modal scanning probe microscopy

As in standard FM-AFM [106], we use a lock-in amplifier² to resonantly drive each mode and demodulate the resulting optical signal measured by the photo-receiver. A voltage signal reference, given by the sum of two tones at the modes' resonance frequencies, drives the piezoelectric transducer fixed to the back of the NW chip holder (see Fig. 2.2). Each frequency shift $\Delta f_i = f'_i - f_i$ is tracked by a phase-locked loop (PLL), while a proportional integral control loop (PI) maintains the mode's oscillation amplitude constant by adjusting the amplitude of the respective sinusoidal component of the dithering piezo voltage. Owing to the high quality factors and the large frequency gap between the resonances it is possible to monitor and control both

²Zurich Instruments UHFLI + PLL/PID module

modes simultaneously, avoiding any cross-talk between the two PLLs by choosing a proper filter bandwidth to separate each frequency component.

The test sample in Fig. 3.4(a) consists of nine 5- μm long and 200-nm thick finger gates of Au on a Si/SiO₂ substrate, radially disposed and equally spaced along a semicircle. The finger gates and their tapered shape are intended to provide edges at a variety of different angles, highlighting the directional sensitivity of the orthogonal modes. The frequency shift maps $\Delta f_1(x, y)$ and $\Delta f_2(x, y)$ in Figs 3.4(b,c) are acquired keeping a constant oscillation amplitude of 6 nm. The spatial scan is performed at a distance of 70 nm from the Au surfaces without feedback to maintain a constant tip-sample separation, i.e. in ‘open-loop’. The Au gates are grounded during the measurement. Such spatial scans are extremely time efficient and are just limited by the high Q factor of the resonator, i.e. each point is acquired for $Q/f \sim 125$ ms. The frequency shift images clearly delineate the topography of the patterned sample, with each mode showing stronger contrast for features aligned along orthogonal directions. These two directions (identified by noting the direction of the fingers with maximum contrast) agree with the angle $\beta = 75^\circ$ measured for NW1 via the thermal noise plotted in Fig. 3.2. Edges, i.e. large topographical gradients, pointing perpendicular (parallel) to the mode oscillation direction appear to produce the strongest (weakest) contrast. The nature and strength of the tip-sample interactions, producing the frequency shifts in non-contact AFM, depends on the distance and can include electrostatic (long-range), van der Waals, or chemical bonding (short-range) forces. In our case, because of the ‘large’ spacing, they are entirely dominated by electrostatic forces.

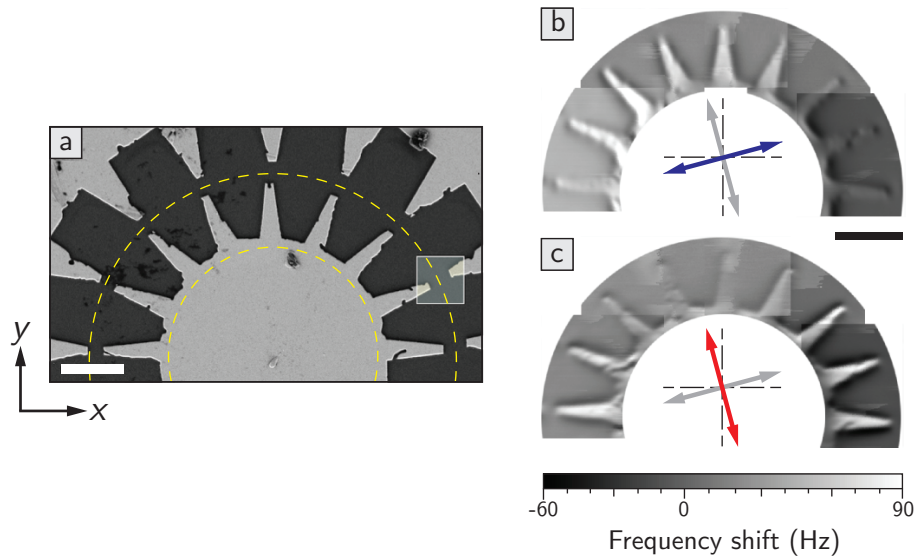


FIGURE 3.4 | **2D lateral force microscopy.**

(a) SEM micrograph of the scanned sample. The frequency shift data shown refer to the region delimited by the dashed yellow line. The results presented in Section 3.4 and 3.5 are restricted to the highlighted $3.6 \times 3.6 \mu\text{m}$ region. Scale bar $5 \mu\text{m}$. (b,c) Frequency shift maps obtained by tracking mode 1 and mode 2 resonance simultaneously. Due to the limit xy scanning range at 4.2 K, the complete maps are obtained combining together 5 scans. The oscillation amplitude for each mode is kept constant at 6 nm. The spacial resolution is ultimately limited by the large diameter of the NW. Scale bars $5 \mu\text{m}$.

3.3.2 Nanowire dynamics in a bi-dimensional force field

The information given by the frequency shifts Δf_i is not sufficient to entirely describe the interaction of the NW with the sample's force field. Hereby, we apply the bi-dimensional vectorial Eq.(1.29) – obtained in Section 1.2.1 – to describe the planar motion of the NW tip $\mathbf{r}(t)$ subjected to an external force $\mathbf{F}(t)$. In general, we focus on the force field governing the motion of the two fundamental mode's polarizations, ignoring the contribution of higher orders modes. In scanning probe microscopy, it would correspond to the so-called tip-sample interaction force which is felt by the probe starting from a certain distance from the sample (Fig. 3.5(a)).

To describe each component we can use Eq. (1.25) and write:

$$M\ddot{r}_i + \Gamma_i \dot{r}_i + M\omega_i^2 r_i = \delta F + F_i \quad (3.1)$$

where δF is the Langevin force and F_i is the modal force which was introduced in Section 1.1.1. The latter accounts for the portion of the applied force $\mathbf{F}(t)$ acting along $\hat{\mathbf{r}}_i$. In the more general case of a distributed force $\mathbf{F}(z, t)$ at the NW position, it has to be averaged over the length by the normalized mode shape as $F_i(t) = \langle u_0(z), \mathbf{F}(z, t) \cdot \hat{\mathbf{r}}_i \rangle = \int_0^L u_0(z) F_i(z, t) dz$. Following from the definition, a punctual force acting at the tip is expressed $\mathbf{F}(t)\delta(z - L)$. In order not to overcrowd the notation, the force is always considered at the NW rest position $r_i = 0$ and therefore often omitted as well as the time dependence.

Following the treatment of *Gloppe et al.* [22], F_i can be expanded up to the first order for small oscillations around the equilibrium $r_i = 0$, giving $\mathbf{F}(\mathbf{r}) \approx \mathbf{F}(\mathbf{0}) + (\nabla_{\mathbf{r}} \mathbf{F})|_0 \cdot \mathbf{r}$. Each modal force writes as

$$F_i \approx F_i(0) + \sum_{j=1,2} r_j \left. \frac{\partial F_i}{\partial r_j} \right|_0 \quad (3.2)$$

By replacing this expansion in (3.1), we can write the equations in vectorial form as

$$M\ddot{\mathbf{r}} + \underline{\underline{\Gamma}}\dot{\mathbf{r}} + \underline{\underline{K}}\mathbf{r} = \mathbf{F}_0 + \delta\mathbf{F} \quad (3.3)$$

where $\mathbf{r} = [r_1 \ r_2]^T$ and the equilibrium tip-sample force $\mathbf{F}_0 = \mathbf{F}(\mathbf{r} = \mathbf{0})$. The dissipation and spring constant matrices are defined by:

$$\underline{\underline{\Gamma}} \equiv \begin{bmatrix} \Gamma_1 & 0 \\ 0 & \Gamma_2 \end{bmatrix} \quad (3.4)$$

$$\underline{\underline{K}} \equiv \begin{bmatrix} k_1 - F_{11} & -F_{21} \\ -F_{21} & k_2 - F_{22} \end{bmatrix} \quad (3.5)$$

where $k_i = M\omega_i^2$ is the effective spring constant of the mode and we used a shorthand notation for the force derivatives $F_{ij} \equiv (\partial F_i / \partial r_j)|_0$. Note that, in the following we prefer to make use of the modal stiffness k_i which is compliant with the usual expressions adopted by the scanning force microscopy community and has the physical dimensions of a force gradient (N/m). As $\underline{\underline{K}}$ matrix definition (3.5) makes clear, the field derivatives F_{ii} of the tip-sample force alter the modes' intrinsic stiffness redefining new effective spring constants, while the shear cross-derivatives on the anti-diagonal, i.e. F_{ij} for $i \neq j$, act as coupling terms for the two mechanical polarizations [107].

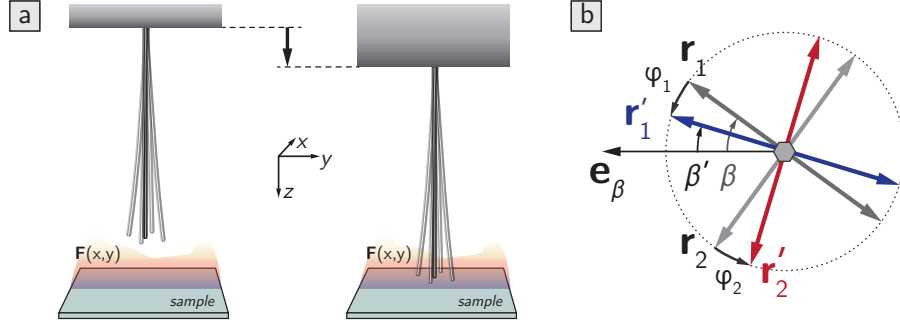


FIGURE 3.5 | **NW immersed in a tip-sample force field and eigenvectors rotation.**

New eigenfrequencies and modal coordinates In the presence of weak tip-surface interactions, as those studied here, the dissipation rates of the NW modes are negligibly small compared to their unperturbed resonant frequencies, i.e. $\frac{\Gamma}{2M} \ll \sqrt{\frac{k}{M}}$. In this limit, the NW mode frequencies and oscillation directions are determined by $\underline{\underline{K}}$. Therefore, by diagonalizing $\underline{\underline{K}}$, we can find a new pair of uncoupled flexural modes. The corresponding spring constants and mode directions result modified from the unperturbed state by the spatial tip-sample force derivatives F_{ij} as

$$k'_{1,2} = \frac{1}{2} \left(k_1 + k_2 - F_{11} - F_{22} \pm \sqrt{(k_1 - k_2 - F_{11} + F_{22})^2 + 4F_{12}F_{21}} \right) \quad (3.6)$$

$$\begin{aligned} \hat{\mathbf{r}}'_1 &= \frac{1}{\sqrt{(k_2 - F_{22} - k'_1)^2 + F_{12}^2}} \begin{bmatrix} k_2 - F_{22} - k'_1 \\ F_{12} \end{bmatrix} \\ \hat{\mathbf{r}}'_2 &= \frac{1}{\sqrt{(k_1 - F_{11} - k'_2)^2 + F_{21}^2}} \begin{bmatrix} F_{21} \\ k_1 - F_{11} - k'_2 \end{bmatrix} \end{aligned} \quad (3.7)$$

These new modes remain orthogonal ($\hat{\mathbf{r}}'_1 \cdot \hat{\mathbf{r}}'_2 = 0$) for conservative force fields ($\nabla \times \mathbf{F} = 0$, i.e. $F_{12} - F_{21} = 0$), but lose their orthogonality for non-conservative force fields. Such property can be deduced from the fact that, if $F_{12} = F_{21}$, $\underline{\underline{K}}$ is symmetric and therefore its eigenvectors of distinct eigenvalues ($k'_1 \neq k'_2$) are orthogonal.

Weak-field limit For tip-sample force derivatives that are much smaller than the bare NW spring constant – as in our case – the modified spring constants and the modified modal coordinates in (3.6) and (3.7) can be approximated to first order

derivatives:

$$k'_1 \approx k_1 - F_{11} \quad \text{and} \quad k'_2 \approx k_2 - F_{22} \quad (3.8)$$

$$\begin{aligned} \hat{\mathbf{r}}'_1 &\approx \frac{1}{\sqrt{(k_1 - k_2)^2 + F_{12}^2}} \begin{bmatrix} k_1 - k_2 \\ -F_{12} \end{bmatrix} \\ \hat{\mathbf{r}}'_2 &\approx \frac{1}{\sqrt{(k_1 - k_2)^2 + F_{21}^2}} \begin{bmatrix} F_{21} \\ k_1 - k_2 \end{bmatrix} \end{aligned} \quad (3.9)$$

In the limit of small dissipation discussed previously ($\Gamma \ll M\omega$), analogously to the unperturbed situation, the new resonance frequencies of the flexural modes are given by $f'_i = \frac{1}{2\pi} \sqrt{k'_i/M}$. For small tip-sample force derivatives, we can apply the approximated expression (3.8), obtain $f'_i \approx \frac{1}{2\pi} \sqrt{(k_i - F_{ii})/M}$ and finally expand to first order in F_{ii} , finding $f'_i \approx f_i - \frac{f_i}{2k_i} F_{ii}$.

Solving in terms of the frequency shift induced by the tip-sample interaction, we have:

$$\Delta f_i = f'_i - f_i \approx -\frac{f_i}{2k_i} F_{ii} \quad (3.10)$$

Therefore, by monitoring the frequency shift between the bare resonances and those modified by the tip-sample interaction, we measure F_{ii} as

$$\left. \frac{\partial F_i}{\partial r_i} \right|_0 \approx -2k_i \left(\frac{\Delta f_i}{f_i} \right) \quad (3.11)$$

Note that, because the oscillation amplitude is usually very small compared to the tip diameter (in our case it is 6 nm against a NW diameter of ~ 350 nm), the spatial variations of the force derivative over the oscillation cycle can be neglected. Just as in conventional 1D dynamic force microscopy (e.g. standard non-contact AFM along z -axis and lateral AFM driving the cantilever torsional mode), each $\Delta f_i(x, y)$ depends on the derivative F_{ii} , i.e. on the force both projected and differentiated along the mode oscillation direction. The mode doublet of a NW probe, however, is able to simultaneously measure force derivatives along orthogonal directions.

With the mechanical parameters of NW2, a frequency shift of one linewidth $\Delta\omega = \Gamma/M$ corresponds to a gradient $F_{ii} = 2\omega\Gamma \approx 1.4 \times 10^{-7}$ N/m. However, gradients in the order of 1 nN/m can be sensed at the limit resolution of the frequency shift measurement which can be set to a hundred times less the linewidth (i.e. RBW ~ 0.1 Hz) by calculating the noise PSD spectrum on the demodulated signal around the resonance frequencies.

Using the expressions in (3.9), we can also write an expression involving the angle ϕ_i between the bare mode direction $\hat{\mathbf{r}}_i$ and the corresponding modified mode direction $\hat{\mathbf{r}}'_i$, as pictured in Fig. 3.5(b):

$$\tan \phi_i \approx \frac{F_{ij}}{|k_i - k_j|} \quad (3.12)$$

This equation then allows us to solve for $F_{ij} = \partial F_i / \partial r_j$ for $i \neq j$ in terms of the rotation of the mode axes ϕ_i and the unperturbed spring constants:

$$\left. \frac{\partial F_i}{\partial r_j} \right|_0 \approx |k_i - k_j| \tan \phi_i \quad (3.13)$$

For NW2, a modes rotation $\phi = \pi/4$ corresponds to a shear gradient $F_{ij} = |k_i - k_j| \approx 1$ mN/m. From this expression it follows that the sensitivity to shear gradients can be improved by using softer NWs with higher cross-sectional symmetry to reduce the modes' frequency splitting.

In the following, we apply Eqs. (3.11) and (3.13) to calculate all the in-plane tip-sample force derivatives in the small interaction limit (i.e. all derivatives much smaller than the unperturbed spring constants) by monitoring the doublet mode frequency shifts Δf_i and oscillation directions ϕ_i ,

Strong-field limit In this regime, the strength of the gradients F_{ii} is much bigger than the modes' stiffness k_i . Therefore, the stiffness matrix \underline{K} can be approximated by the Jacobian (gradients) matrix³ $\underline{J}_{\mathbf{F}}$ of the force field, which takes over the NW dynamics at the first order approximation. In this conditions, while the modes' stiffness (and eigenfrequencies) are directly and unlimitedly modified by the gradient longitudinal components F_{ii} , the rotation of the modes reaches a saturation angle. In fact, at each position the NW's modal coordinates are oriented in order to diagonalize the force gradients matrix, aligning along the force field principal directions. More specifically, the mode 1 at lower frequency points to the direction of the eigenvector with the lowest eigenvalue, while mode 2 points to the direction with the highest eigenvalue [23].

In conclusion, the mapping of strong field gradients results more straight-forward, since the NW's modes indicate at each point the direction of the force field principal axes.

3.4 Imaging of static in-plane force derivatives and dissipation

A complete measurement of static in-plane force derivatives, the resulting force field, and dissipations is performed using NW2 over a smaller scanning region (see Fig. 3.4) at a fixed spacing of 70 nm from the grounded gold electrodes. It is important to remark that, despite having set the electrodes and the NWs support at the same potential, a residual voltage V_0 exists between the NW and the golden gates, due to the difference in electron work function of the two materials ($W_{Au} - W_{NW} = -eV_0$).

Δf_i and Γ_i are extracted by fitting Eq. (1.49) to the spectral density of the thermal noise measured at each acquisition position of the scan window. In particular, by assuming a conservative tip-sample interaction ($F_{ij} = F_{ji}$ hence $\phi_1 = \phi_2$), we determine $\phi = \beta' - \beta$ by comparing the extracted modes' angle to the NW's intrinsic polarization directions extracted far from the surface, which is $\beta = 46.5^\circ$ as shown in Fig. 3.3. In order to measure any force field, including non-conservative force fields such as those due to opto-mechanical interactions [87], ϕ_1 and ϕ_2 have to be measured independently, i.e. along two linearly independent measurement vectors. As described

³ $\underline{J}_{\mathbf{F}_{ij}} = F_{ij}$

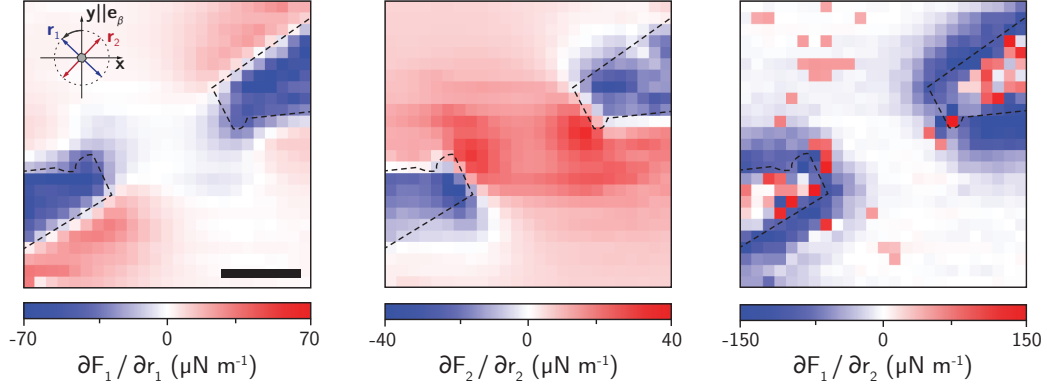


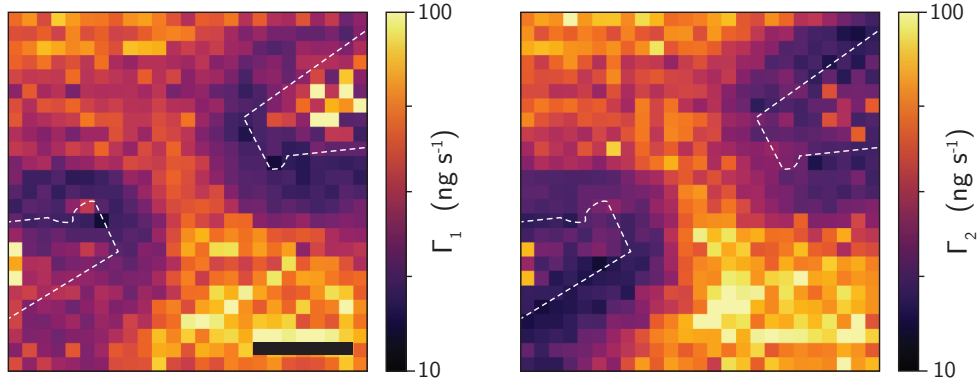
FIGURE 3.6 | **In-plane force gradients of tip-sample interaction.**

Force derivatives F_{11} , F_{22} , and $F_{12} = F_{21}$, respectively, extracted from thermal noise data as a function of the xy -position of NW2, at 70 nm over the sample. Overlaid dashed lines indicate the edges of the finger gates, as obtained by SEM (see Fig. 3.4). Inset: scanners (x, y) and NW modes (r_1, r_2) coordinate system orientation. Scale bar 1 μm .

in Section 2.2.3, such a measurement it is possible in our fiber-coupled setup, by positioning the NW slightly on the side of the optical axis and detuning the laser wavelength to shift the interference fringe and therefore rotate the optical gradient direction.

Using these data along with Eq. (3.11) and Eq. (3.13), we produce maps of $F_{ij}(x, y)$ and $\Gamma_i(x, y)$, plotted in Figs. 3.6 and 3.7, respectively. The measurements show strong positive followed by negative contrast of F_{ii} for edges perpendicular to the NW mode oscillation $\hat{\mathbf{r}}_i$. In non-contact AFM, long-range tip-sample forces have an electrostatic origin and are generally attractive, getting stronger with decreasing tip-sample distance and increased interaction area. As the NW approaches a Au edge perpendicular to $\hat{\mathbf{r}}_i$ from a position above the lower Si surface, it experiences an increasingly attractive force, i.e. a positive F_{ii} . After the midpoint of the tip crosses this edge, the attractive force starts to drop off, resulting in a negative F_{ii} [98]. The consideration of an instrumental mechanical vibration between sample and NW is required in these fits to produce integrable force derivatives. The root mean squared amplitude of this vibration is 3 nm root-mean-square, which is reasonable for our experimental setup. This parameter only affects measurements of $F_{12} = F_{21}$ in Fig. 3.6, which depend on ϕ_i and are derived from the ratio of the mean square displacements of the two modes. Measured dissipations Γ_i in Fig. 3.7 are nearly isotropic and appear to reflect the different materials and tip-sample spacings over the Au fingers and the Si substrate. Similar 1D measurements of non-contact friction also show lower values over conducting surfaces like Au compared to insulating surfaces like Si and point to charge fluctuations as the origin for the dissipation [27, 28]. Another possible mechanism is the so-called Joule dissipation, attributed to a residual static charge on the NW tip generating a time varying image charge (current) on the sample underneath, which dissipates energy depending on the local resistivity.

In order to produce a vectorial force map in the (x, y) coordinates reference of the scanners (laboratory frame), a change of coordinate system is required for the force gradients obtained in the reference system of NW's uncoupled modes (r_1, r_2) . We can

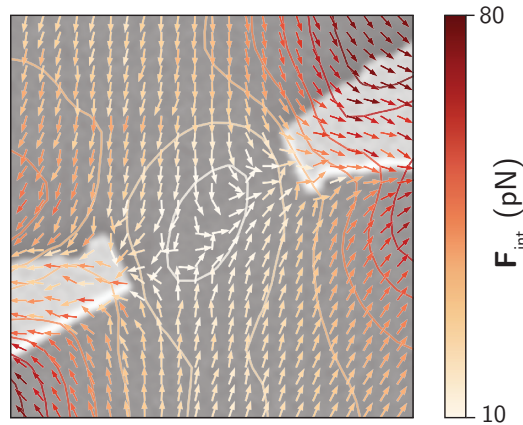
FIGURE 3.7 | **Dissipation maps.**

Dissipation Γ_i of each mode as a function of the xy -position. Scale bar $1 \mu\text{m}$.

use

$$\begin{aligned}
 F_{xx} &= F_{11} \sin^2 \beta + F_{22} \cos^2 \beta - \cos \beta \sin \beta (F_{12} + F_{21}) \\
 F_{yy} &= F_{11} \cos^2 \beta + F_{22} \sin^2 \beta + \cos \beta \sin \beta (F_{12} + F_{21}) \\
 F_{xy} &= F_{12} \cos^2 \beta + F_{21} \sin^2 \beta - \cos \beta \sin \beta (F_{22} - F_{11}) \\
 F_{yx} &= F_{21} \cos^2 \beta + F_{12} \sin^2 \beta - \cos \beta \sin \beta (F_{22} - F_{11})
 \end{aligned} \tag{3.14}$$

where β is the angle between the $\hat{\mathbf{r}}_1$ and the y -axis (i.e. our measurement vector). The 2D gradient ∇F_x (∇F_y) is integrated over the 25×25 points of the map to extract the relative force field component F_x (F_y). At each cell (i, j) , the value of F_x corresponds to $F_x(i, j) = F_x(i_0, j_0) + \int_{\mathcal{C}} (F_{xx} dx + F_{xy} dy)$, where \mathcal{C} is a path connecting the starting cell (i_0, j_0) to the current cell (i, j) ; similar expression applies for $F_y(i, j)$. Respect to the straight-forward 1D integration used for conventional AFM data [108], in the 2D case the calculation should be ideally performed averaging the result on every

FIGURE 3.8 | **In-plane tip-sample force field.**

The map is numerically integrated from the force derivatives in Fig. 3.6 up to a spatially constant force. Solid lines show contours of constant force magnitude.

possible short path connecting the two points. However, to simplify the process, the calculation was performed iteratively along rows and columns starting from each of the four sides of the domain. The obtained results were then averaged together. The map of the static in-plane force field due to tip-sample interactions is shown in Fig. 3.8. Note that this force field is determined up to an integration constant, i.e. up to a spatially constant force. The field lines confirm the presence of a residual electrostatic force attracting the NW towards the golden electrodes, even when the NW chip support and the gates are grounded. The electrostatic ‘zero’ in between the gates corresponds to an equilibrium position (unstable) where the attractive forces cancel out.

3.5 Dynamic measurement of 2D force fields

Any force field coupling to the NW, if modulated on resonance, can be mapped with a thermally limited sensitivity of $5 \text{ aN}/\sqrt{\text{Hz}}$ by measuring the induced displacements of the two modes. At each point, the coherent trajectories generated in this way correspond to the NW response to two resonant forces.

The measurement scheme, illustrated in Fig. 3.9, is similar to the one used for the driven bi-modal scan in Section 3.3.1. Here, instead of driving a dither piezo to enhance the modes’ displacement and speed-up the readout of tip-sample interaction (i.e. force gradients in terms of frequency shifts), the NW’s motion is resonantly excited by the force field itself, allowing for a direct force detection.

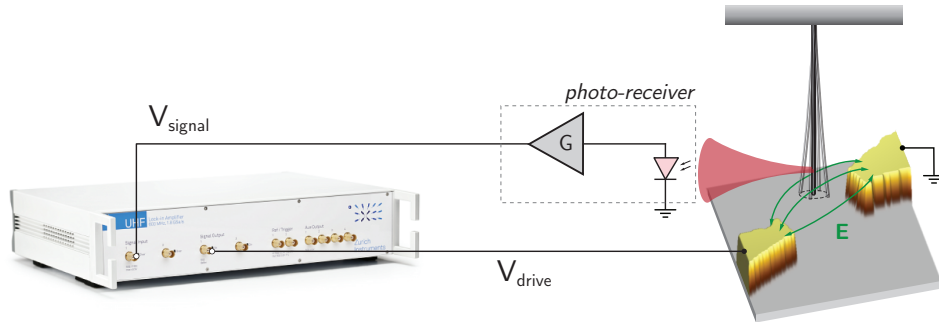


FIGURE 3.9 | **Operating scheme for the dynamic measurement of 2D force fields.**

In this way, we study the electrostatic nature of the interaction forces by applying a small AC voltage drive $V_{drive} = V_d \sin(\omega t)$ to produce an oscillating electric field $\mathbf{E}(\mathbf{r}, t)$ between the opposing finger gates.

The model of the total force field has two contributions:

- a Coulomb force term, linearly dependent on the electric field strength, associated with trapped surface charges

$$\mathbf{F}_q = q\mathbf{E} \propto V_d \quad (3.15)$$

where q is the net charge on the NW tip;

- a term with quadratic dependence on the field strength, associated with the induced dipolar moment of the dielectric NW in an external electric field⁴ [109]. By considering a scalar polarizability, the force can be written as

$$\mathbf{F}_p = -\nabla(\alpha|\mathbf{E}|^2) \propto V_d^2 \quad (3.16)$$

where α is the effective polarizability of the GaAs/AlGaAs NW.

Due to their linear and quadratic dependence on \mathbf{E} , respectively, \mathbf{F}_q drives the NW at frequency ω , while \mathbf{F}_p drives it at DC and 2ω . As a result, the two interactions can be spectrally separated.

By scanning the sample in a plane 70 nm below NW2 and measuring thermal motion and driven response at each point, we construct vectorial maps of the \mathbf{F}_q and \mathbf{F}_p , as shown in Fig. 3.10(a) and (c), respectively.

In first place, the thermal noise spectrum in the absence of the AC drive, is acquired to calibrate the orientation $\hat{\mathbf{r}}'_i$ and resonance frequencies ω'_i of the modes doublet, which are altered by the static tip-sample interaction as described in Section 3.4. Then, the frequency of the driving voltage V_{drive} is swept through $\omega'_i/2$ and ω'_i to probe \mathbf{F}_p and \mathbf{F}_q respectively, by recording amplitude and phase of the displacement signal. In this way, the resulting force is always resonantly driving each mode, which can be described as

$$M\ddot{r}'_i + \Gamma'_i\dot{r}'_i + k'_i r'_i = \delta F + F_{d,i} \sin(\omega t + \phi) \quad (3.17)$$

where $F_{d,i}$ is the force component along $\hat{\mathbf{r}}'_i$.

In the linear regime, the modes' displacement amplitude and phase are determined by their mechanical susceptibility $\chi'_i(\omega) = 1/(k'_i - M\omega^2 + i\Gamma'_i\omega)$, as presented in Section 1.2.1. As shown schematically in Fig. 3.10(e), the magnitude and orientation of the driving force at each point is extracted from the displacement and phase response of each mode as a function of frequency. For mode i , the oscillation amplitude is fitted by $|\chi'_i(\omega)||F_{d,i}(\omega)|$ and gives the magnitude of the driving force $F_{d,i}$ along $\hat{\mathbf{r}}'_i$. Instead, the phase $\arg(F_{d,i}(\omega))$ gives the direction of $F_{d,i}$ along either positive or negative $\hat{\mathbf{r}}'_i$. As an alternative measurement protocol for one of the two forces, it would be possible and faster to use two PLLs (as in Section 3.3.1) to simultaneously excite and track the resonant response of both modes with two distinct tones. In this case, the PLLs' phase set-point has to be adjusted during the scan, since the phase response undergoes a π -shift when the force component driving the mode becomes negative (see Fig. 3.10(e)). These measured force fields are compared to the \mathbf{E} and $-\nabla|\mathbf{E}|^2$ fields simulated by FEM analysis (COMSOL) using the real gate geometries in Figs. 3.10(b) and (d). Dividing the measured force fields by the corresponding simulations, we estimate an equivalent net charge on the NW tip $q = 30 \pm 10e$, where e is the fundamental charge, and the effective polarizability $\alpha = 10^{-29}$ C/(V m), which is roughly consistent with the size and dielectric constant of the NW.

⁴ $\mathcal{E}_{pol} = \mathbf{p} \cdot \mathbf{E} \simeq \alpha|\mathbf{E}|^2$; $\mathbf{F}_p = -\nabla\mathcal{E}_{pol}$

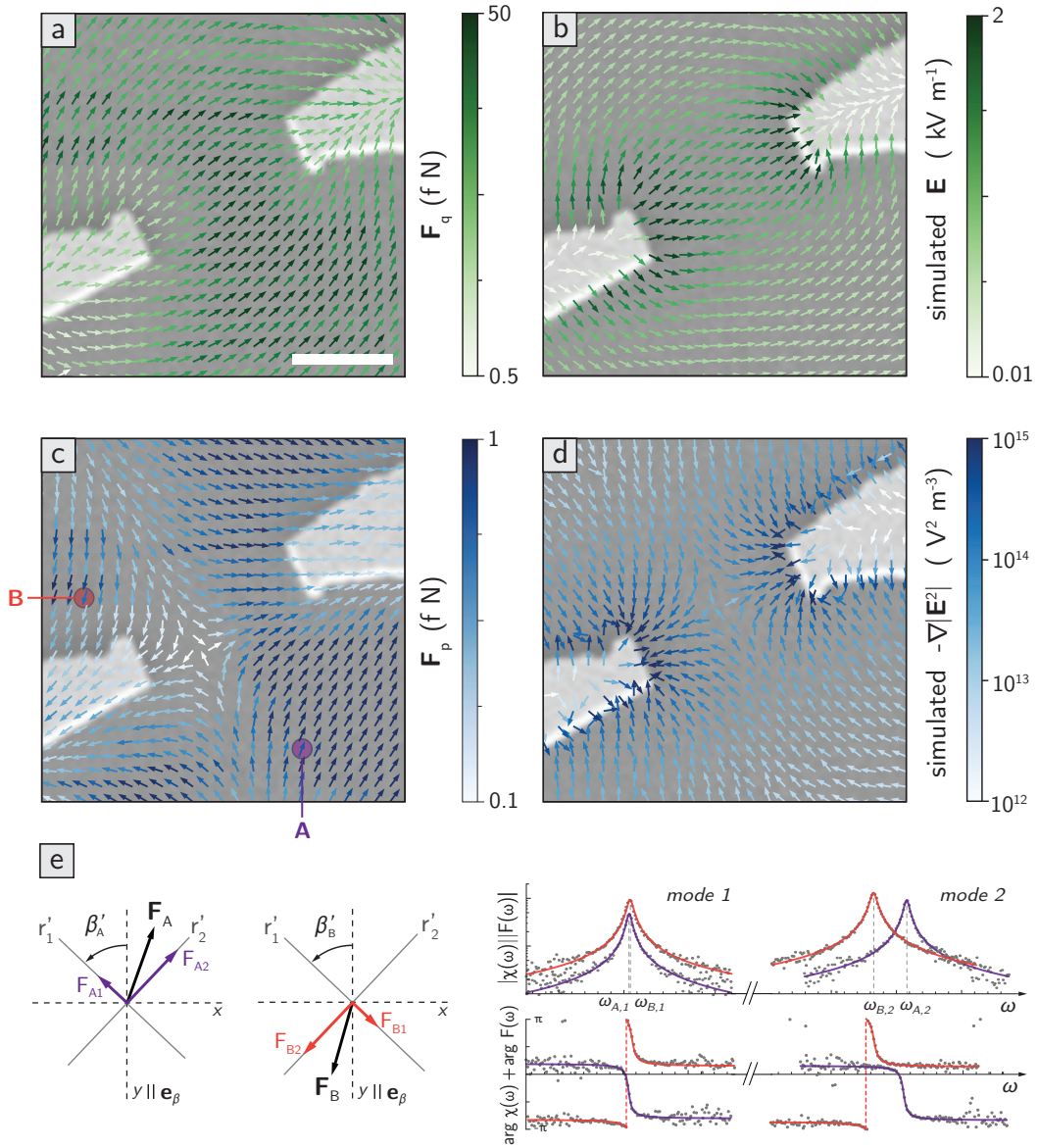


FIGURE 3.10 | **Vector plots of electrostatic force fields.**

(a) Vector plot of the force field induced by an electric field on the charged NW. The vector plot is overlaid on top of a SEM image of the sample. The scale bar represents $1 \mu\text{m}$. (b) Vector plot of the simulated electric field $\mathbf{E}(\mathbf{r})$ induced by the biased finger gates. (c) Vector plot of the force field induced by the electric field on the polarizable dielectric NW. The voltage amplitude applied to the gates in (a) and (c) is 2 mV and 20 mV, respectively, the vertical spacing between NW2 and the Au gates is 70 nm. (d) Vector plot of the simulated values of $-\nabla|\mathbf{E}(\mathbf{r})|^2$ induced by the biased finger gates. (e) Schematic explanation of how force vectors are extracted from measurements at the example positions A and B shown in (c). Example plots on the right showing amplitude and phase response as a function of driving frequency illustrate the method (violet/red for positions A/B). The magnitude of the force component along each mode direction is extracted from the displacement of that mode. The phase response of the mode with respect to the driving then allows the extraction of the sign of the force component along each mode direction.

3.6 Coherent Two-Mode Dynamics

Classically coherent dynamics analogous to those of quantum two-level systems can be studied in this setting of force sensing.

In the last years, the coherent dynamics in classical systems has been studied in the context of nanoscale mechanical resonators, typically top-down fabricated and with doubly clamped geometry. In particular, strong coupling between mechanical modes [107, 110, 111], driven Rabi oscillations [110–112] and Stückelberg interferometry [113] have already been demonstrated, measuring also coherence and dephasing times [110, 114]. Here, exploiting the electrostatic NW-sample interaction characterized previously, we demonstrate quantitative control over the coupling between two orthogonal mechanical modes of a nanowire cantilever, through measurement of avoided crossings as we deterministically position the nanowire in the electric field produced by gate electrodes. Furthermore, we measure Rabi oscillations between the two mechanical modes in the strong coupling regime.

By applying a static voltage V_g to the gates, we control the strength of the interaction between the NW and the electric field. As discussed in the previous section, the resultant force is given by the sum of a weak Coulomb term $\mathbf{F}_q \propto V_g$ due to a small surface charge excess and a term $\mathbf{F}_p \propto V_g^2$ due to the polarization of the bound charge inside the dielectric NW. Note that this linear and quadratic dependence on the voltage it also applies to the respective force gradients. The eigenfrequencies of the hybridized modes can be derived from Eq. (3.6), indicating explicitly the dependence of the force gradients F_{ij} on V_g

$$\omega'_{1,2} = \frac{1}{\sqrt{2}} \left[\omega_1^2 + \omega_2^2 - \frac{F_{11}(V_g)}{M} - \frac{F_{22}(V_g)}{M} \pm \sqrt{\left(\omega_1^2 - \omega_2^2 - \frac{F_{11}(V_g)}{M} + \frac{F_{22}(V_g)}{M} \right)^2 + \frac{4F_{12}(V_g)^2}{M^2}} \right]^{1/2} \quad (3.18)$$

Avoided crossings A signature of strong coupling is formed by mode energies exhibiting avoided crossing under detuning, with a splitting larger than the sum of the linewidths of the individual resonances [115]. At the same tip-gates distance of 70 nm and with a procedure similar to the one adopted in Section 3.4, we search for such avoided crossings by acquiring thermal noise spectra at each point (x, y) for a set of voltage values in the interval $[-10 \text{ V}, 0 \text{ V}]$ with steps of 500 mV. From this, we determine the mode frequencies ω'_i for each spatial point (x, y) as a function of V_g .

In Fig. 3.11(a) and 3.12(b) are plotted the frequencies $f'_i = \omega'_i(V_g)/2\pi$ for exemplary positions in the electric field generated by the gate electrodes, which exhibit an avoided crossing. In order to obtain a frequency anti-crossing, starting from a small V_g (weak-field limit), each longitudinal gradient components F_{ii} has to shift the correspondent frequency towards the other. This condition can be met in many combinations of sign and magnitude of the two F_{ii} terms, which ultimately determine the sign and curvature of the parabolic frequency shift around zero voltage. In all the cases shown, at low V_g , mode 1 gets stiffer (f'_1 increases), i.e. $F_{11} < 0$, while mode 2 gets softer (f'_2 decreases), i.e. $F_{22} \geq 0$.

At the center of an avoided crossing, for voltage $V_g = V_x$, the eigenmodes are fully hybridized in a symmetric and antisymmetric superposition of the original modal

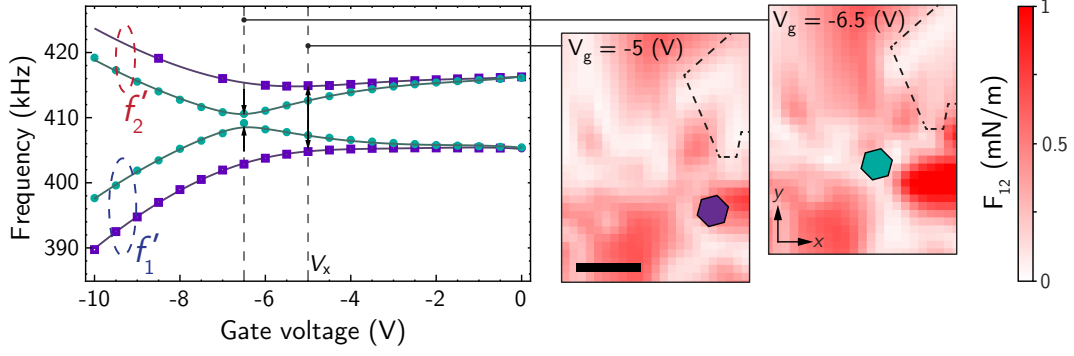


FIGURE 3.11 | **Shear force gradient vs. gate voltage mapping**

(a) Mode frequencies as a function of the gate voltage. Data points represented by green circles are taken at the position indicated by the green hexagon drawn in (b), while the violet squares corresponds to data taken at the position of the violet hexagon in (b). The curves are fits of Eq. (3.18) to the data. Both sets of data show avoided crossings, with different splittings due to different coupling strengths. (b) Spatial maps of the measured coupling term F_{12} for $V_g = -5$ V (left) and $V_g = -6.5$ V (right). The dashed black line indicates the position of the nearest gate electrode. Scale bar 500 nm.

basis. The size of the avoided crossing can be approximated as

$$\Delta\omega_x \equiv \Delta\omega(V_x) = \omega'_2 - \omega'_1 \approx \frac{F_{12}(V_x)}{M\omega_0} \quad (3.19)$$

where $\omega_0 \equiv \sqrt{\omega_1^2 - \frac{F_{11}(V_x)}{M}} = \sqrt{\omega_2^2 - \frac{F_{22}(V_x)}{M}}$.

We see, therefore, that the splitting is proportional to the coupling force gradient. Moreover, by moving along the edge of a gate electrode, we can controllably set F_{12} and observe avoided crossings with correspondingly different gap sizes. Fitting Eq. (3.18) to $\omega'_1(x, y, V_g)$ and $\omega'_2(x, y, V_g)$, directly returns the values for F_{11} , F_{22} , and F_{12} as a function of (x, y, V_g) . Setting the gate voltage at each avoided crossing ($V_g = V_x$) displayed in Fig. 3.11(a), the strength of the coupling term $F_{12}(V_x)$ can be mapped spatially as shown in Fig. 3.11(b). Consistently with expectations, the larger avoided crossing occurs at a position where F_{12} is larger. Similarly, we can obtain spatial maps of F_{11} , F_{22} , and F_{12} for each voltage V_g [116].

Fig. 3.12 analyzes in more detail the evolution of the modes' frequency and orientation at a fixed position on the plane which shows well defined avoided crossings. At $V_g = V_x$, the modes have been turned by an angle that maximizes the shear components F_{ij} . Around these points, the change in curvature of the frequency curves indicates that the respective longitudinal gradients F_{ii} are changing sign, pulling the frequencies in the opposite direction. Locally, the field lines are mostly perpendicular to the mode basis $(\hat{\mathbf{r}}_1, \hat{\mathbf{r}}_2)$, which indicates the dominant role of the off-diagonal coupling terms F_{ij} .

In the high-field limit ($|V_g| > 6$ V), the first mode is rotating towards the direction of the eigenvector of the force gradients matrix with the lowest absolute value (smallest curvature), as explained in Section 3.3.2. The displacement spectra in Fig. 3.12 show additional damping, increasing quadratically with the gate voltage, due to the dissipative re-orientation of the dipoles in the resonator caused by its motion in a static and inhomogeneous electric field. It can be taken into account by considering a complex

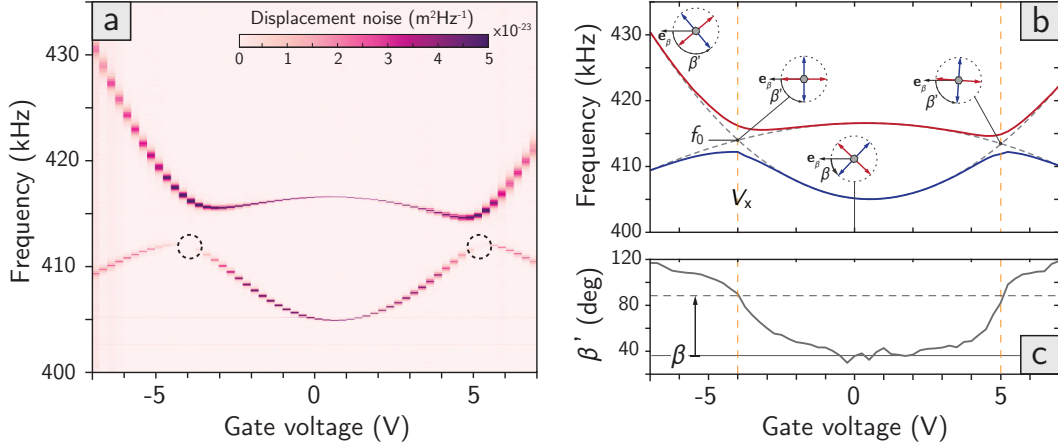


FIGURE 3.12 | **Vibrational modes evolution at an anti-crossing point.**

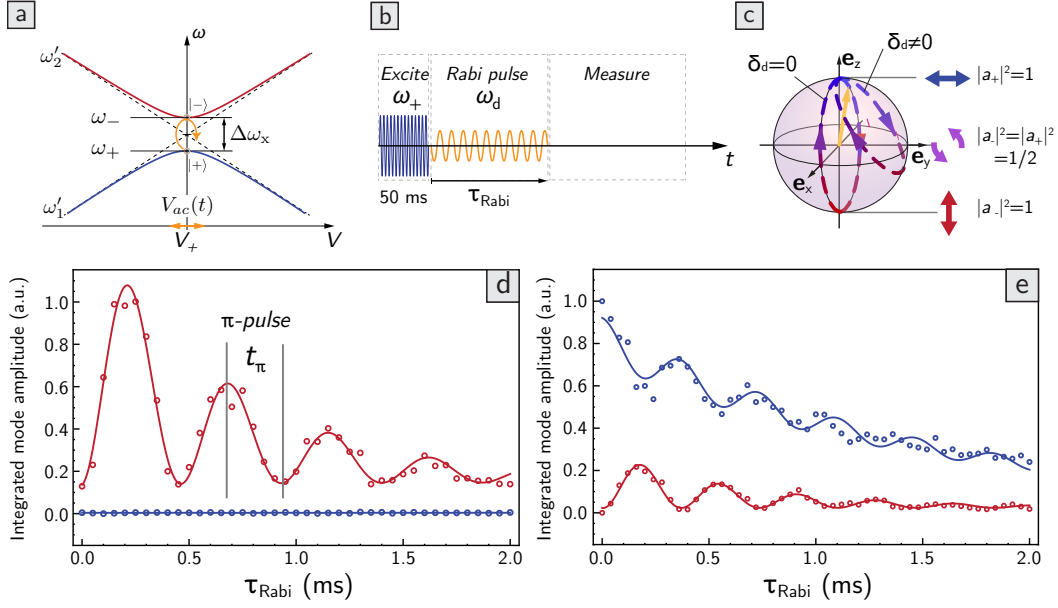
(a) Evolution of the displacement noise density as a function of the applied gate voltage V_g . The mode frequencies f'_i and orientation angle β' respect to the measurement vector, shown in (b) and (c) respectively, are obtained by fitting the spectra in (a). The two gray dashed parabolas in (b) correspond to a second order polynomial fit and show the deviation of the two frequencies in absence of coupling. At high fields, the direction of the modes is inverted with respect to the initial situation. The minimum of the lower parabola at $V_g \sim 0.5$ V confirms the existence of a residual electrostatic force. (c) Due to the intrinsic orientation of the modes $\beta \sim 45^\circ$, at the anti-crossing points the modes' basis rotates of $\sim 45^\circ$ making first mode becomes orthogonal respect to the detection direction \mathbf{e}_β , and therefore not measurable (see dashed circles in (a)). β' saturates ideally at 90° .

polarizability $\alpha = \alpha' + i\alpha''$ [109]. Moreover, the dissipation shows strong dependence on the electric field orientation, being higher on the first mode for $V_g < V_x$ and then moving onto the second one as a result of the modes' rotation.

Rabi oscillations In strongly coupled two-level systems, energy can be coherently exchanged between the two levels through driven Rabi oscillations. Here, such regime of operation is confirmed by frequency splittings $\Delta\omega_x$ of several kHz compared to linewidths of few tens of Hz. At the avoided crossing, the system can be parametrically driven through a periodic modulation of the detuning [117]. When the modulation frequency ω_d is close to the frequency difference $\Delta\omega_x$, a coherent oscillation between the populations of the two modes takes place. Here, modulation of the detuning is generated by superimposing an oscillating voltage drive $V_{ac}(t) = V_d \cos(\omega_d t)$ over the gate voltage V_g .

Borrowing the notation from the two-level quantum mechanical system representation, we indicate the first and second hybrid state (mode) frequency and orientation respectively as ω_+ , $|+\rangle = (1, 1)$ and ω_- , $|-\rangle = (1, -1)$ (see Fig. 3.13(a)). In a classical picture, Rabi oscillations between the populations $|a_\pm|^2$ of the two modes (i.e. power stored in each mode), including decay, can be described as [117]

$$|a_+(t)|^2 = \cos^2\left(\frac{\omega_R t}{2}\right) e^{-\Gamma t} \quad , \quad |a_-(t)|^2 = \sin^2\left(\frac{\omega_R t}{2}\right) e^{-\Gamma t} \quad (3.20)$$

FIGURE 3.13 | **Rabi oscillations.**

(a) Sketch of the energy swap between the eigenmodes at the avoided crossing, by harmonically modulating of the voltage detuning with $V_{ac}(t)$. (b) Schematic of Rabi pulsing scheme. (c) Bloch sphere representation of Rabi oscillations. The two trajectories on the sphere correspond to resonant and non-resonant Rabi oscillations. (d) Detected spectral power of both modes as a function of Rabi pulse duration, for zero detuning $\delta_d = 0$. The fit for mode $|-\rangle$ (red line) returns a Rabi frequency of 1.9 kHz ($\Delta\omega_x/2\pi = 10.9\text{kHz}$). (e) Similar to (d), but for $\delta_d \neq 0$. Fits yield Rabi frequencies of 2.8 kHz (mode $|-\rangle$) and 3.0 kHz (mode $|+\rangle$) with $\Delta\omega_x/2\pi = 12.1\text{kHz}$. Note that the offset in the measured Rabi oscillations is due to thermal excitation of the mode. Moreover, following from the definition of the Rabi frequency, $\omega_R^{non-res} > \omega_R^{res}$ for all $\delta_d \neq 0$.

Here, initialization is assumed to give $|a_-(0)|^2 = 0$, $|a_+(0)|^2 = 1$. Furthermore, $\omega_R = \sqrt{A^2 + \delta_d^2}$ is the generalized Rabi oscillation frequency, with the amplitude A set by V_d , and $\delta_d = \omega_d - \Delta\omega_x$.

We use a single decay constant Γ for both modes, since for the two hybridized modes (at the center of the avoided crossing), population decay rates should be equal. Γ corresponds to the time constant of evolution towards $|a_-(0)|^2 = 0$, $|a_+(0)|^2 = 0$. In a Bloch sphere representation of the populations, this corresponds to a shrinking of the state vector.

In order to excite and detect Rabi oscillations in our system, we implement the following measurement protocol (see Fig. 3.13(b)). First, we excite mode $|+\rangle$ by applying a drive pulse with frequency ω_+ for 50 ms. Next, a pulse of varying duration τ_{Rabi} with frequency ω_d is supplied in order to drive the Rabi oscillations. During this pulse, a coherent exchange of energy takes place between the two modes, resulting in a change of the two populations. Finally, the populations of the two modes are read out by measuring the power spectral density of each mode. For each Rabi pulse duration τ_{Rabi} , we average such cycle over 50 acquisitions.

Figure 3.13(d) shows Rabi oscillations for $\delta_d = 0$ (i.e. $\omega_d = \Delta\omega_x$). Since we are using NW2 which has an intrinsic orientation of $\beta \sim 45^\circ$ respect to our detection

direction (see Fig. 3.3), at $V_g = V_x$ the modes result aligned approximately parallel (mode $|-\rangle$) and perpendicular (mode $|+\rangle$) to the optical axis of the interferometer (see Fig. 3.12(b)). Consequently, the displacement noise of mode $|+\rangle$ is below our detection noise, and Rabi oscillations are hard to detect. Instead, for a small but finite δ_d (i.e. $\omega_d = \Delta\omega_x + \delta_d$), the modes are rotated with respect to the optical axis, and Rabi oscillations can be detected for both modes (see Fig. 3.13(e)). In this case, the Rabi oscillations result in only a partial transfer of populations, as can be understood from the schematic depiction of the Bloch sphere in Fig. 3.13(c). For $\delta_d = 0$, the Rabi frequency depends linearly on the drive amplitude A , where A is a quadratic function of V_d . We observe Rabi frequencies in the kHz-regime, with a maximum of 4.5 kHz, as determined from fitting Eq. 3.20 to the data. The same fits return values for the relaxation time $T_1 = M/\Gamma = Q/\omega$ between 0.6 and 1.5 ms, in agreement with independent ringdown measurements.

Interestingly, our driven two-mode system is close to the regime of strong driving, with the Rabi frequency ω_R approaching the transition frequency $\Delta\omega_x$. We observe a maximum of roughly $\omega_R = \Delta\omega_x/3$. When a two-level system is strongly driven, its dynamics is not simply sinusoidal anymore, but can become anharmonic and non-linear. In other systems, ripples on top of sinusoidal oscillations have been observed [118], as well as oscillations that are faster than expected from the Rabi model [119, 120]. Such effects may explain irregularities in our measurements. Furthermore, note that in our experiments we were limited by our electronics allowing only a limited amplitude A of the Rabi drive, and higher Rabi frequencies should be feasible. This would enable further studies of the strong driving regime in the case of a classical two-mode system.

3.7 Discussion and outlook

Our measurements demonstrate the potential of NWs as sensitive scanning vectorial force sensors. By monitoring two orthogonal flexural modes while scanning over a sample surface, we map forces and force derivatives in 2D. While we demonstrate the technique on electrostatic tip-sample interactions, the ability to vectorially map electric fields on the nanometer-scale extends the capability of conventional AFM to image charges [121, 122] and contact potential differences [97] and has applications in localizing electronic defects on or near surfaces, e.g. in microelectronic failure analysis.

The technique has a universal applicability, given a proper functionalization of the NW tip, and can for instance be used to measure magnetic forces [25] – as will be shown in the next Chapter – or even in liquid [71] for the study of batteries, water splitting, or fuel cells. Note that in the presented data, the 350 to 400-nm diameters of the NW tip strongly limited the spatial resolution of the microscopy. Nevertheless, the same directional technique could be applied to NWs grown or processed to have sharp tips [75], presenting the possibility of atomic-scale or even sub-atomic-scale force microscopy, a feature already achieved in 1D [102]. The vectorial nature of the NW-based non contact-AFM is therefore ideal to reveal anisotropies of non-contact friction and forces like atomic bonding forces.

Chapter 4

Magnetic Force Sensing Using a Self-Assembled Nanowire

4.1 Introduction

In magnetic force microscopy (MFM), mass-produced ‘top-down’ Si cantilevers with sharp tips coated by a magnetic material represent the current standard since many years. Under ideal conditions, state-of-the-art MFM can reach spatial resolutions down to 10 nm [123], though more typically around 100 nm. These conventional cantilevers are well-suited for the measurement of the large forces and force gradients produced by strongly magnetized samples.

In this context, nanostructures grown by ‘bottom-up’ techniques, such as carbon nanotubes (CNTs), have been used to functionalize AFM cantilevers’s tip in order to obtain finer spacial resolution. Such a tiny extension serves essentially as a template to achieve a very localized and highly concentrated deposition of the magnetic material [124–127]. However, even in these implementations, the cantilever’s force sensitivity is imposing stringent conditions on the detectable magnetic signal as a function of tip-sample distance, tip’s volume and magnetization.

As discussed throughout this thesis, in order to overcome these limitations, it is possible to use NWs and CNTs as mechanical force transducers in scanning probe applications, exploiting their mechanical properties and very high force sensitivity. In principle, such sensitivity to small forces allows to operate MFM in a different regime, allowing on the one hand to detect very weak magnetic fields and therefore to image subtle magnetic patterns, on the other hand to use even tinier magnetic tips to achieve nanometer-scale spatial resolution, while also reducing the invasiveness of the tip on the sample under investigation. Such improvements are crucial for imaging nanometer-scale magnetization textures such as domain walls, vortices and skyrmions [128–131], superconducting vortices [132, 133]; mesoscopic transport in two-dimensional systems [134], and small ensembles of nuclear spins [14, 135–137].

Following from recent experiments introducing the use of single NWs and CNTs as sensitive scanning force sensors [22, 23, 138], including the one discussed in the previous chapter [33], we aimed to integrate a magnetic tip onto a NW transducer and therefore to give a proof-of-principle of ‘NW-MFM’. Due to its singly-clamped beam geometry, the NW is arranged in the pendulum geometry to probe both the size and direction of weak in-plane magnetic forces, maintaining excellent force sensitivities of few aN/ $\sqrt{\text{Hz}}$ near sample surfaces (< 100 nm), due to extremely low non-contact friction [29].

In this chapter, remaining in the framework of self-assembled as-grown NWs, we demonstrate such MFM transducers using individual GaAs NWs with integrated single-crystal MnAs tips, grown by molecular beam epitaxy (MBE).

We first introduce the structural and magnetic properties of the sample. Then, by monitoring the motion of each NW's flexural mode in a static magnetic field, we are not only able to determine its mechanical properties, but also to characterize the MnAs nanomagnet at the tip via dynamic torque magnetometry. Moreover, we determine the equilibrium magnetization configurations of each tip by comparing its magnetic response with micromagnetic simulations.

Finally, in order to determine the sensitivity and resolution of the NWs as MFM probes, we use them as scanning probes in the pendulum geometry. By analyzing their response to the magnetic field produced by a lithographically patterned current-carrying wire, we find that the MnAs tips can be approximated as magnetic dipoles. The thermally-limited sensitivity of a typical NW to magnetic field gradients is found to be $11 \text{ mT}/(\text{m}\sqrt{\text{Hz}})$, which corresponds to the gradient produced by $63 \text{ nA}/\sqrt{\text{Hz}}$ through the wire at a tip-sample spacing of 250 nm.

4.2 GaAs nanowires with a ferromagnetic MnAs tip

In the group led by Prof. D. Bougeard at University of Regensburg, has been developed a method for the epitaxial growth of single ferromagnetic MnAs nanoscale segments in GaAs NWs [35]. The NWs are produced with the Ga-catalyzed growth method [74] using Si(111) wafers covered with a thin layer of native oxide as a substrate and a growth temperature of 600° .

In order to terminate the growth with a magnetic tip, the liquid Ga catalyst droplet at the top of the NW is heavily alloyed by a Mn flux. Then, to initiate its crystallization, it is exposed to an As_4 background pressure for 30 min. Under such conditions, the droplet undergoes a sequential precipitation: first, the Ga is preferentially consumed to build pure GaAs; next, the remaining Mn crystallizes in the form of MnAs. The outcome of such procedure is shown at the tip of a NW in the bright field STEM image in Fig. 4.1(a). The chemical composition in the corresponding area has been detected by energy-dispersive X-ray spectroscopy (EDX) and confirms a homogeneous content of As and a net separation between Ga and Mn, the latter only confined in the tip region (Fig. 4.1(b,c,d)).

Furthermore, the crystallinity of both GaAs and MnAs phases is revealed by high-resolution TEM imaging. The GaAs wire is mostly zinc-blende (ZB) with few twin planes. In the final part shown in Fig. 4.1(e), a short GaAs wurzite (WZ) segment is followed by few nanometers of GaAs ZB, as expected from the consumption and precipitation of the Ga from the Ga-Mn alloy in the tip's droplet. On top, the MnAs compound can be clearly identified as a well-defined hexagonal α -MnAs WZ crystal, with an epitaxial relationship $[0001]\text{MnAs} \parallel [111]\text{GaAs}$ along the growth axis (i.e. NW's axis).

4.2.1 Magnetic properties of MnAs(0001)/GaAs(111)

Bulk MnAs compound was already studied more than a hundred years ago, in 1904, by Heusler [140]. Few years later, in 1911, its ferromagnetism and two polymorphic phase transformations were discovered by Hilpert and Dieckmann [141].

In fact, MnAs can adopt three different phases depending on the lattice temperature. A first order transition is observed around 40° where the ferromagnetic hexagonal α -MnAs phase starts turning into an orthorhombic β -MnAs phase, which is usually assumed to be paramagnetic. The shrinking of the hexagonal lattice cell causes a reduction in volume and the ferromagnetic coupling to disappear, therefore setting the Curie temperature of MnAs just above RT at $T_C \approx 40^\circ$.

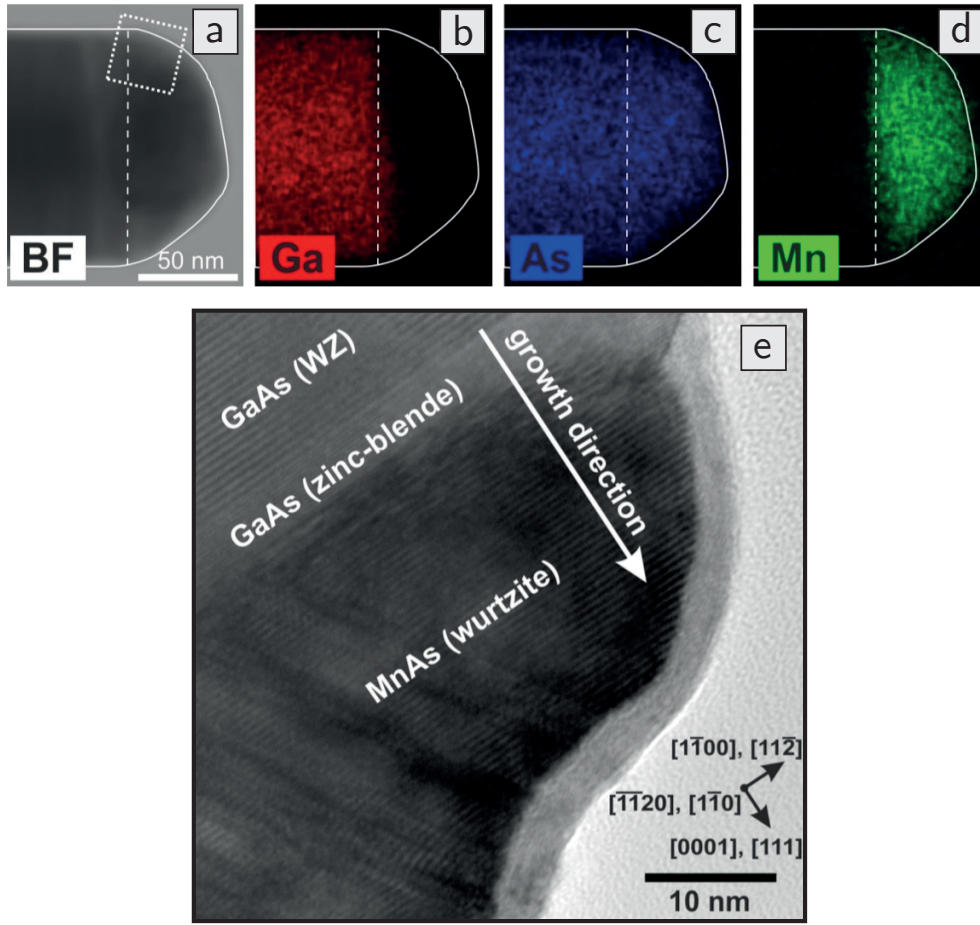


FIGURE 4.1 | **Composition and crystal structure of MnAs-tipped nanowires.**

(a) Bright field STEM and (b,c,d) EDX maps for Ga, As and Mn at the tip region of the nanowire. (e) HRTEM image of the dotted area in (a). Epitaxial relations in the lower right corner are referred to the ZB GaAs final layer. Adopted from [139].

Notably, the α - β transition presents thermal hysteresis and the two phases can coexist around RT [142, 143]. A second order transition at 126° reverses the crystal structure back to WZ, without any volume change.

With the advances in nanotechnologies, MBE grown ferromagnet/semiconductor hybrid structures such as MnAs/GaAs has been extensively studied as potential candidates for spintronics at RT [144]. Due to the high technological relevance of the GaAs(001) surface, most of the studies focus on this substrate's orientation. Here, the hexagonal MnAs crystal structure is growing with the c -axis lying in-plane (i.e. orthorhombic unit cell). The lattice constant c contracts much more than the underneath GaAs lattice constant while cooling down to RT, causing a very pronounced strain-induced in-plane anisotropy of the physical properties of the film, reflected in a strong uniaxial (in-plane) magnetic anisotropy (Fig. 4.2(c)).

On the contrary, MnAs on GaAs(111), i.e. the growth orientation of our magnetic tips, has the c -axis (0001) perpendicular to the substrate and therefore free to relax [145]. Minor biaxial strain is released in-plane to accommodate the different lattice constants between the hexagonal WZ MnAs ($a = 3.725 \text{ \AA}$ and $c = 5.713 \text{ \AA}$) and cubic

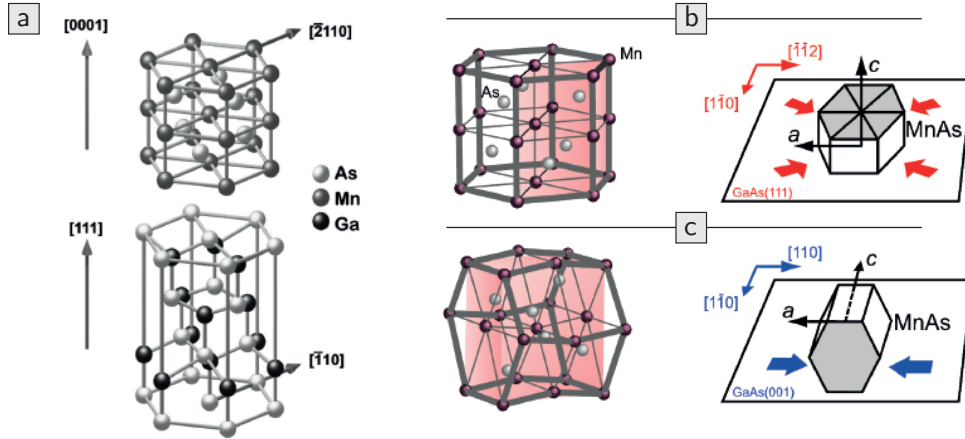


FIGURE 4.2 | **MnAs/GaAs crystalline configurations and epitaxial relations.**

(a) Sketch of the crystal orientations of WZ MnAs (above) grown on the (111) surface of a ZB GaAs crystal (below). Adopted from [145]. (b) MnAs/GaAs(111). On the left, crystal structure of α -MnAs consisting of hexagonal planes of Mn and As. Unit cell highlighted in red. On the right, epitaxial scheme with biaxial compressive strain indicated by arrows. (c) MnAs/GaAs(001). On the left, orthorhombical crystal structure with a distorted unit cell highlighted in red. On the right, epitaxial scheme with uniaxial compressive strain indicated by arrows along the a -axis||[110]. Magnetocrystalline anisotropy is quite strong in the sample plane, with easy and hard axis being the a and c axis, respectively. Adopted from [146].

ZB GaAs ($a = 5.65 \text{ \AA}$). In such configuration, the MnAs crystal is characterized by a strong magnetocrystalline anisotropy K in the form of a magnetic hard axis parallel to the c -axis, which, in general, is coincident with the NW growth direction. As a result, the magnetization will tend to lie in the growth plane being a nearly isotropic magnetic easy plane [143]. Additional factors like strain and shape anisotropy can potentially lift the degeneracy of the in-plane directions.

The main magnetic parameters for MnAs, summarized in Table 4.1, have been taken from literature and deployed in our micromagnetic simulation described in 4.3.2. Since no study at 4 K has been reported, assuming a minor dependence with temperature, the parameters are all referred to RT except for the magnetocrystalline anisotropy, which was measured in bulk at 77 K [147].

| | Symbol | Value |
|--|-------------|----------------------------------|
| Saturation magnetization [143] | $\mu_0 M_s$ | 1.005 T |
| Exchange stiffness constant [143] | A_{ex} | 10 pJ/m |
| Uniaxial magnetocrystalline anisotropy [147] | K | $-1.2 \times 10^6 \text{ J/m}^3$ |

TABLE 4.1 | **MnAs/GaAs(111) magnetic parameters.**

4.2.2 Mechanical properties

SEM micrographs of the growth batch used in this experiment are shown in Fig. 4.3. Most of the NWs are perpendicular to the substrate (i.e. $[111]$ direction) with a length of $17 \pm 1 \mu\text{m}$ and a diameter of $225 \pm 15 \text{ nm}$. To a lesser extent, also parasitic growth occurs along other angled direction, as typically observed on Si(111) wafers. The NWs show slight inverse tapering of about 0.2%, while a wider tapering ($\sim 10\%$) is usually present at the base due to the radial growth stabilization at the beginning of the process (Fig. 4.3(a)). These deviations from the ideal NW geometry with constant cross-section can contribute to the frequency splitting of the modes and to marginal changes of the effective mass for the first order mode. A crystallized MnAs tip is present in the vast majority of the standing NWs, while the regularity of its shape and faceting can vary significantly, due to its self-assembled nature (Fig. 4.3(b)).

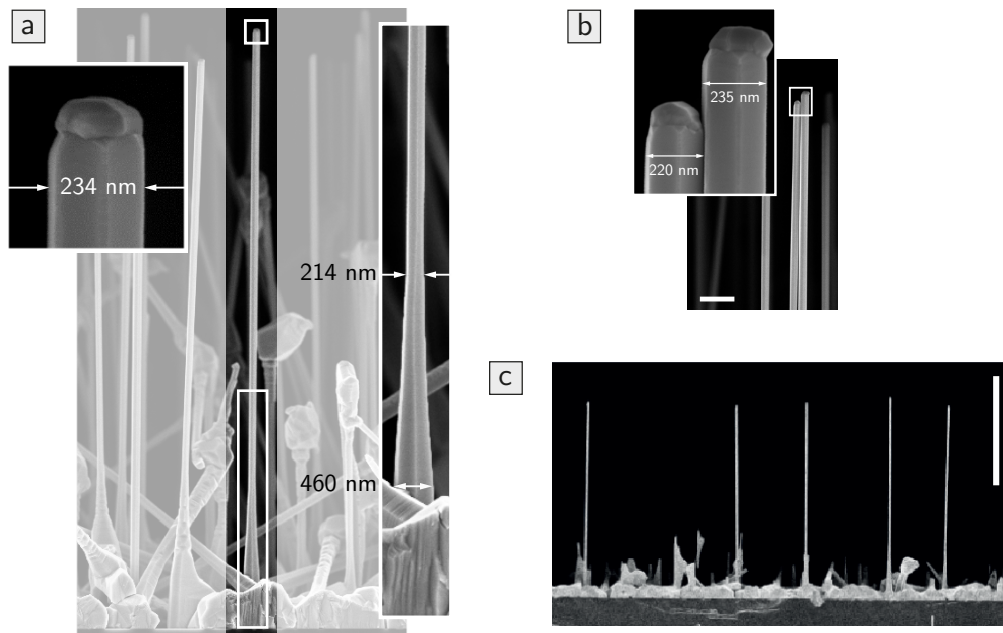


FIGURE 4.3 | **SEM micrographs of GaAs NWs with MnAs tip.**

(a) Vertical standing NW on the unprocessed wafer. Zoomed-in insets of the tip and base area. (b) Particular of crystallized MnAs tips (scale-bar $1 \mu\text{m}$). Images taken by F. Dirnberger. (c) Particular of the processed chip with NWs standing next to the cleaved edge (scale-bar $10 \mu\text{m}$).

Following the procedure described in Appendix B, a small chip ($\sim 1\text{-}2 \text{ mm}^2$) is obtained from the growth $2''$ wafer, processed and installed in our measuring setup (Section 2.1). In first place, by means of a micro-manipulator, only a single row of vertical standing NWs is left along the designated reference cleaved edge. After SEM imaging, the NWs not showing a crystallized MnAs tip or much shorter than the average are selectively removed from the chip. The resulting sample – partially shown in Fig. 4.3(c) – consists of tens of NWs spaced at least by $5 \mu\text{m} > 2w_0$, with w_0 being the beam's waist, to avoid the presence of more than one NW in the focal spot and therefore the simultaneous motion detection of multiple NWs.

More than 50 NWs have been characterized thanks to the ease of navigation in such array-like configuration. Each doublet of mechanical frequencies served also as a tag to backtrack the NWs of interest.

Fig. 4.4 shows a typical thermal noise spectrum measured in our setup. In general, resonance frequencies range from 500 to 700 kHz and, for each NW, the doublet modes are completely separated by a frequency splitting δ of several hundred times the peak line width, given the high quality factors. The two modes' mechanical parameters can be extracted just by fitting the data with Eq. (1.49).

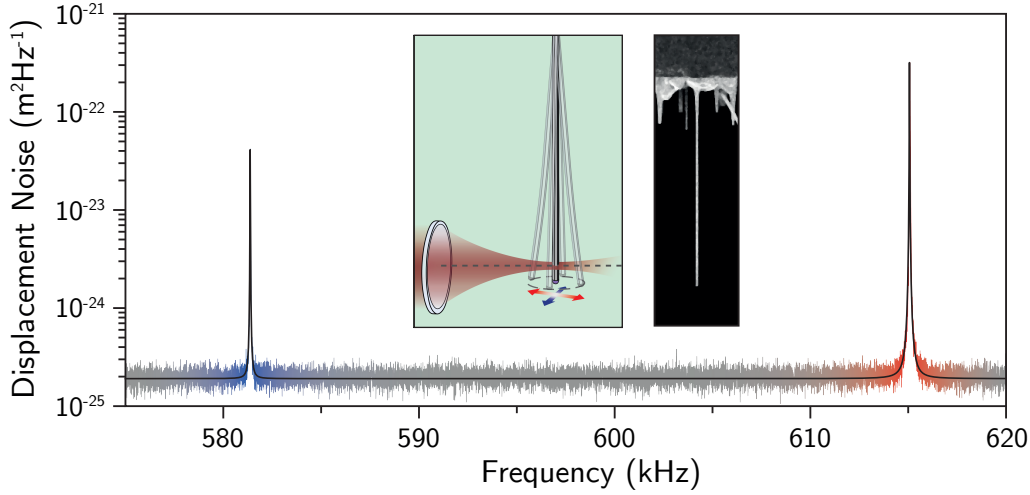


FIGURE 4.4 | **Displacement noise spectrum of a MnAs-tipped GaAs NW.**

Power spectral density (PSD) of the thermally excited NW's displacement measured with an incident optical power of $25\mu\text{W}$. The two peaks, highlighted in blue and red, correspond to the doublet of first order flexural modes. The raw data is fitted by the black line. The extracted resonance frequency, spring constant, and intrinsic quality factor of the first (second) mode are $f_{01} = 581\text{ kHz}$, $k_1 = 10.5\text{ mN/m}$ and $Q_1 = 44650$ ($f_{02} = 615\text{ kHz}$, $k_2 = 11.6\text{ mN/m}$ and $Q_2 = 48456$). Estimated motional mass is $M = 780\text{ fg}$. The first mode is rotated by an angle $\beta = 70^\circ$ respect to the measurement direction. Insets: sketch of the extracted polarizations direction with respect to the vector measurement \mathbf{e}_β collinear with the optical axis. On the right, SEM micrograph of the measured NW with hexagonal cross-section of maximal diameter 234 nm and length $16.8\text{ }\mu\text{m}$.

In the cooling process from RT to 4.2 K, the resonant frequencies of the NWs' first order flexural modes shift by about $+8\text{ kHz}$. This stiffening is related to the Young modulus' temperature dependence in GaAs [148]. A similar behavior was observed also for core-shell GaAs/AlGaAs NWs studied in Chapter 3.

At RT, typical quality factors start from several hundreds in air and improve by a factor $\times 10$ in vacuum already at a pressure of $\sim 10^{-3}\text{ mbar}$, due to the drastic decrease of viscous and acoustic damping. By cooling the resonator at liquid helium temperature, the modes' quality factors usually gain another factor $\times 10$. Their values range between 2×10^4 and 5×10^4 , differing from each other by less than 1%. The spring constants extracted from fits to the PSD for each flexural mode are on the order of 10 mN/m , yielding a mechanical dissipation (friction coefficient) and a thermally limited force sensitivity down to 50 pg/s and 3 aN/Hz , respectively.

With a systematic study of the thermal noise PSD at several positions along the NW and at different laser powers, we observed a heating of the NW above the 4.2 K bath temperature up to 15 K, when the detection spot overlaps with the MnAs particle. Similar effects were reported on Si NWs with Au catalyst particle at the tip [24]. For

scanning purposes, however, this aspect is irrelevant since the laser is focalized far away from the NW extremity.

4.3 Nanowire dynamic torque magnetometry

In order to use our NWs as magnetic sensors it is crucial to be able to obtain a characterization of their magnetic behavior. In fact, similarly to MFM, the mechanical response of the NW in an external magnetic field will depend on the tip's magnetic configuration. Thanks to the high mechanical sensitivity of the NWs and to the possibility to apply an homogeneous magnetic field in our setup, we were able to probe the magnetization of each individual magnetic tip by means of a technique known as dynamic cantilever magnetometry (DCM).

This technique has enabled a large variety of experiments including the measurement of magnetic dissipation in individual nanomagnets [149], persistent currents in normal metal rings [10], magnetization reversal processes and vortex-like states in magnetic nanotubes [9, 150, 151] and skyrmion phase mapping in MnSi NWs [8].

Conventional cantilever torque magnetometry detects with high sensitivity the weak magnetic response of nanometer-scale samples mounted on a cantilever and placed in a homogeneous external field \mathbf{B} . The sample's net magnetic dipole moment $\mathbf{m}(\mathbf{B})$ will therefore exert a torque $\boldsymbol{\tau} = \mathbf{m} \times \mathbf{B}$ on the cantilever. Generally, three distinct modes of operation can be distinguished:

1. The *static mode* measures the deflection of the cantilever caused by the torque. Despite enabling a direct measurement of the magnetization, this method does not operate at cantilever's resonance and therefore sacrifices sensitivity.
2. The *dynamic cantilever magnetometry (DCM)* - used in this thesis - measures the resonator's frequency and dissipation as a function of the applied static field. As a consequence, it requires a model of the magnetization in order to extract quantitative information above the sample's magnetic properties¹.
3. The *phase-locked cantilever magnetometry* [152] combines the two previous techniques measuring a dynamic deflection excited by a small alternating torque field orthogonal to a static field. The complexity of the required setup is a major drawback.

It is important to remark the fact that cantilever torque magnetometry provides an integral measurement, averaged over the entire specimen's volume. Dynamic magnetometry (mode 2 and 3) offers a number of advantages in comparison to static magnetometry (mode 1). By operating at the resonant frequency, the measurement is better decoupled from $1/f$ noise and the displacement sensitivity is enhanced by the quality factor Q of the resonator, which greatly facilitates thermal limited force detection. Magnetization dynamics are not accessible since these methods are limited to the resonator's frequency which is usually in the kHz range and thus well below relevant time scales. Hence, DCM data always corresponds to magnetization being in

¹Methods see 4.3.2

equilibrium. This kind of magnetometry is minimally invasive since the motion read-out avoids perturbation of the sample's magnetization by currents as used in transport measurements, intense illumination or inhomogeneous magnetic fields.

4.3.1 Basic principles of dynamic cantilever magnetometry

As-grown MnAs tipped GaAs NWs constitute a device which can be directly characterized by DCM: it provides a magnetic tip at the apex, epitaxially grown onto a high quality mechanical resonator.

As shown in Section 3.3.2, each mode can be treated as an independent damped harmonic oscillator, in the limit of small oscillations and in absence of coupling via external force field gradients.

The equation of motion for each mode can be expressed as

$$M\ddot{r}_i + \Gamma_i\dot{r}_i = \tau_i/l_e \quad (4.1)$$

where M and l_e are the effective mass and effective length, respectively. For $i = 1, 2$, each mode is polarized along the in-plane direction $\hat{\mathbf{r}}_i$ perpendicular to the NW's axis $\hat{\mathbf{n}}$, has a mechanical dissipation Γ_i and senses a torque τ_i . Each mode's deflection angle θ_i , associated to a displacement $r_i = l_e\theta_i$ (for $\theta_i \ll 1^\circ$), depends on the torque exerted on the mode along its correspondent axis of rotation. The total energy E_i for the i -th mode of a NW with a magnetic tip is simply given by the sum of two terms: the mechanical energy in the form of a harmonic oscillator with spring constant k_i and a generic magnetic energy term E_m that will be later better specified:

$$E_i = \frac{1}{2}k_i(l_e\theta_i)^2 + E_m \quad (4.2)$$

In the small angle regime, we can express the torque $\tau_i = -\partial E_i/\partial\theta_i$ in terms of the mode's energy E_i by expanding to the first order around the mode's equilibrium angle $\theta_i = 0$ and obtain

$$\tau_i = -\left(\frac{\partial E_m}{\partial\theta_i}\bigg|_{\theta_i=0}\right) - \left[k_i l_e^2 + \left(\frac{\partial^2 E_m}{\partial\theta_i^2}\bigg|_{\theta_i=0}\right)\right]\theta_i \quad (4.3)$$

By replacing Eq. (4.3) into Eq. (4.1) and rearranging, we obtain the following equation of motion for each mode

$$M\ddot{r}_i + \Gamma_i\dot{r}_i + \left[k_i + \frac{1}{l_e^2}\left(\frac{\partial^2 E_m}{\partial\theta_i^2}\bigg|_{\theta_i=0}\right)\right]r_i = -\frac{1}{l_e}\left(\frac{\partial E_m}{\partial\theta_i}\bigg|_{\theta_i=0}\right) \quad (4.4)$$

Here, the two torque components related to E_m in Eq. (4.3) produce a constant deflection of the NW along $\hat{\mathbf{r}}_i$ and a shift by \tilde{k}_i of the original mode's spring constant k_i , respectively. The latter translates into a shift of the angular resonance frequency $\omega_i = \sqrt{(k_i + \tilde{k}_i)/M}$, which is the measured quantity in DCM. Note that, since the resonator is highly under-damped, the terms related to damping are neglected and in absence of magnetic interaction the bare frequency is just given by $\omega_{0i} = 2\pi f_{0i} = \sqrt{k_i/M}$.

Finally, an expression for the measured frequency shifts² $\Delta f_i = f_i - f_{0i}$ can be

²For complete derivation see SI [8]

written as a function of the applied static magnetic field B affecting the magnetic tip's energy $E_m(B)$

$$\Delta f_i(B) = \frac{f_{0i}}{2k_i l_e^2} \left(\frac{\partial^2 E_m}{\partial \theta_i^2} \bigg|_{\theta_i=0} \right) \quad (4.5)$$

In such a field, by monitoring the resonance frequency of each orthogonal flexural mode f_i , it is possible to probe simultaneously the curvature of the tip's magnetic energy E_m along two orthogonal directions. This is an additional feature in contrast with traditional DCM, where multiple cantilevers and samples mounted in various orientations are required [9, 150].

4.3.2 Magnetic energy and numerical simulations

In order to establish a framework for the prediction and interpretation of our DCM data via Eq. (4.5), it is crucial to provide a model for the MnAs tip's magnetization, and therefore for E_m .

Analytical model

By assuming our tip to be an idealized single-domain magnet, the magnetization $\mathbf{M} = M_s \hat{\mathbf{m}}$ is supposed uniform throughout its volume V , with magnitude equal to magnetization saturation M_s and directed along the unit vector $\hat{\mathbf{m}}$. E_m can be approximated by the sum of a Zeeman term dependent on the external field \mathbf{B} and an anisotropy term related to the magnet's properties [149]:

$$E_m = -V\mathbf{M} \cdot \mathbf{B} - KV(\mathbf{M} \cdot \hat{\mathbf{k}})^2 \quad (4.6)$$

As discussed in Section 4.2.1, MnAs(0001)/GaAs(111) is a hexagonal system with a strong magnetocrystalline anisotropy. The anisotropy energy is expanded up to several orders, but our analysis is restricted to the dominant first two terms, which determine a uniaxial anisotropy K along the unit vector $\hat{\mathbf{k}}$, collinear to the c -axis of the lattice [147]. Since $K \ll 0$, as reported in Table (4.1), $\hat{\mathbf{k}}$ is the hard axis direction for the magnetization, which will tend to lie in the easy plane orthogonal to it.

It is important to remark that Eq. (4.6) gives a simplified description of the tip's magnetism and does not include second order effects such as shape and magnetoelastic anisotropy, which can play an important role in breaking the basal plane isotropy.

In the *high-field limit*, when $|B| \gg |K|/M_s$, \mathbf{M} stays aligned to the external field \mathbf{B} , regardless of the magnetic tip's orientation. Therefore, the first term in Eq. (4.6) is a constant and does not contribute to the measured frequency shifts in Eq. (4.5). This regime, is of particular interest to characterize the sample's saturation magnetization M_s (or alternatively its volume V) and probe its anisotropy.

In our case, with \mathbf{B} ideally parallel to the hard axis \mathbf{K} , the system is in the most unfavorable configuration (maximum of E_m) and therefore the asymptotic limits of Δf_i are expected to be negative. Moreover, since tip oscillates in two orthogonal directions, any difference in Δf_i gives information on additional anisotropy present in the easy plane.

In the *low-field limit* when $|B| \ll |K|/M_s$, the crystalline anisotropy dominates the magnetic energy and the model becomes inconclusive, since the magnetization

is lying in the easy plane. For our MnAs nanoparticles, the measured data in this region is usually rich of features related to complex and non-uniform magnetization configuration. For this main reason we have to rely on numerical calculations for the interpretation of our experimental results.

Numerical model

In order to obtain a complete understanding of DCM measurements, we carry out numerical simulation of the tip's magnetization mainly with two open-source software packages: *Nmag* [153], which is based on the finite element method and *MuMax³* [154], based on the finite element difference method. Both software packages use micromagnetic formalism and solve numerically the Landau-Lifschitz-Gilbert equation. After checking the physical equivalence of the results provided by both methods, *MuMax³* has been preferred for its high computational performance given by GPU-acceleration at the cost of a simpler space discretization in cubic meshes.

The geometrical model of each MnAs magnetic tip is based on observations made by SEM. The side of the cubic mesh elements is set to 5 nm, corresponding to the dipolar exchange length of the material $l_{ex} = \sqrt{2A_{ex}/(\mu_0 M_s)^2}$. The validity of this discretization is confirmed by comparing few representative results with simulations carried out by using much smaller mesh sizes.

With the magnetic parameters listed in Table (4.1), *MuMax³* calculates the equilibrium magnetization configuration for each external field value. Because the microscopic processes in a MnAs tip are expected to be much faster than the NW resonance frequencies, the magnetization of the tip is assumed to be in its equilibrium orientation throughout the NW oscillation.

The simulation also yields the total magnetic energy E_m corresponding to each of the configuration. We calculate Δf_i in Eq. (4.5) by numerically evaluating the second derivatives of E_m with respect to θ_i . As sketched in Fig. 4.5, for each field we calculate E_m at the equilibrium angles $\theta_i = 0$ and at tiny tilt angles $\delta\theta_i < 0.3^\circ$ along the NW modes' orientation i.e. $\theta_i = \pm\delta\theta_i$.

The second derivative can therefore be approximated by a finite difference:

$$\left. \frac{\partial^2 E_m}{\partial \theta_i^2} \right|_{\theta_i=0} \approx \frac{E_m(\delta\theta_i) - 2E_m(0) + E_m(-\delta\theta_i)}{(\delta\theta_i)^2} \quad (4.7)$$

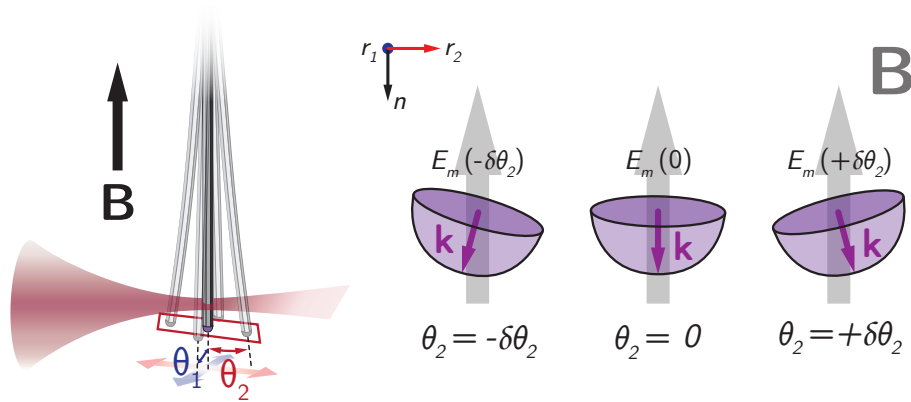


FIGURE 4.5 | Sketch for NW magnetometry measurement and simulation

By setting f_{0i} , k_i and l_e to their measured values, we then obtain the curves $\Delta f_i(B)$ associated to the calculated tip magnetization at each field.

In the simulated geometry, every vector is referred to the orthogonal reference system $\{\hat{\mathbf{r}}_1, \hat{\mathbf{r}}_2, \hat{\mathbf{n}}\}$ defined by the modes' direction and the NW's axis. Note that, in practice, the process of fitting to the data requires multiple iterations to tune the simulation parameters affected by uncertainties on the tip's geometry and possible misalignment of vectorial quantities such as \mathbf{B} and \mathbf{K} , respect to the NW axis $\hat{\mathbf{n}}$.

4.3.3 MnAs tips DCM: experimental results and analysis

The measurements are carried out by saturating the tip at the maximum field for our setup of ± 8 T and stepping it down to ∓ 8 T, while acquiring a PSD of the NW's displacement noise at intermediate points.

The partitioning of the sweeping range $[\pm 8T, \mp 8T]$ is not homogenous and depends on the magnetic properties of the sample. Typically, the measurement points are spaced out by an interval $\Delta B \sim 100$ mT in the high field range which gets refined down to few mT at low field.

We chose to acquire full thermal noise spectra instead of tracking of the driven resonance frequencies via phase-locked loop or self-oscillation protocols, both for simplicity of implementation and 'isotropy' of the thermal driving force. When working at high fields, drift of few micrometers can occur in our microscope requiring additional care to maintain the alignment of the NW respect to the lens, conversely to a conventional cantilever.

The entire experiment is performed by a *LabView* VI program consisting of the following steps for each measurement point:

1. ramping and settling to the current magnetic field value;
2. re-centering of the NW in the xy -plane for optimal motion detection (i.e. the maximum optical gradient position on the optical axis);
3. re-calibration of voltage-to-displacement coefficient³ in the current position;
4. acquisition of the thermal displacement PSD and extraction of the modes' resonance frequencies.

For nearly all investigated NWs (11 out of 12), $\Delta f_i(B)$ is negative for all applied fields. In general, negative values of Δf_i correspond to a local maximum in $E_m(\theta_i)$ with respect to θ_i . As predicted by the simple analytical model described in Section 4.3.2, this is consistent with \mathbf{B} being aligned along the magnetic hard axis of the MnAs tip, which ideally coincides with the NW axis $\hat{\mathbf{n}}$.

We present here data related to three NWs as a representative set of the variety of magnetic behaviors found in our sample. For each NW, DCM has been performed sweeping the external field in both directions, but, due to the exact specularity of the frequency curves, only data related to 'positive to negative' sweep ($+8$ T \rightarrow -8 T) are reported. More details about the simulated tip geometries and fit parameters are given in Appendix C.

³Methods see 2.2.3

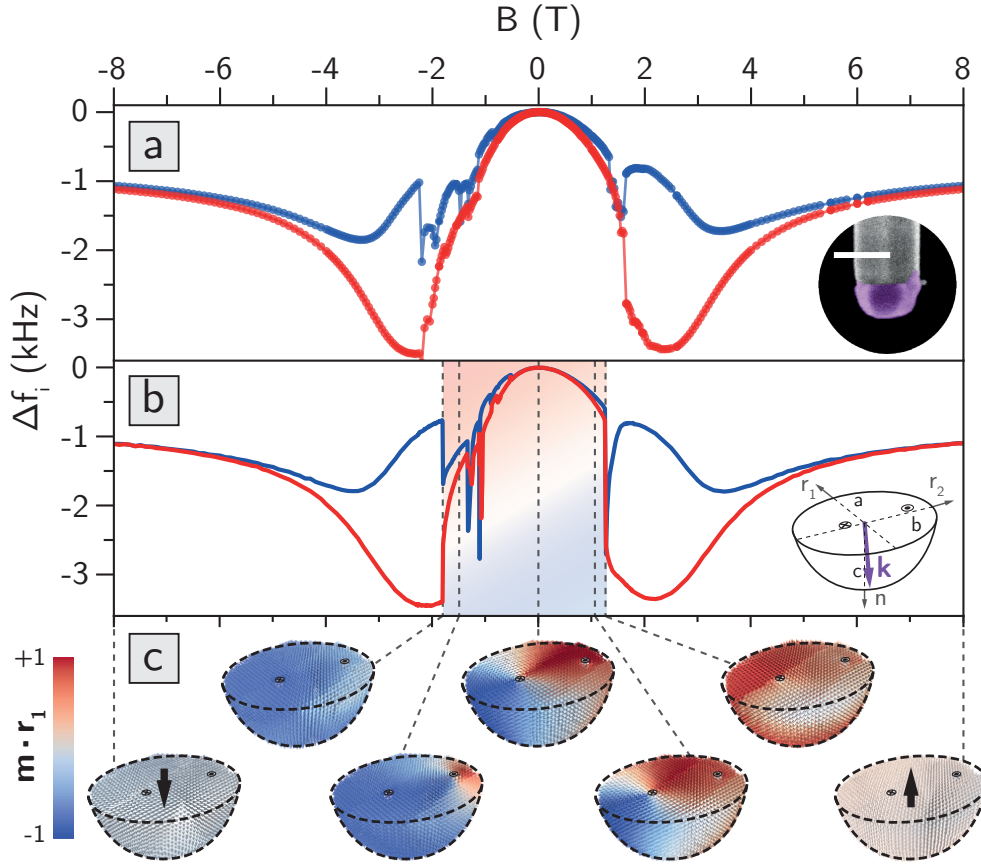


FIGURE 4.6 | **NW1 - MnAs tip magnetometry: zero-field vortex state.**

(a) Plot of the $\Delta f_i(B)$ for $i = 1$ ($i = 2$) in blue (red), extracted at each B from the thermal displacement PSD. The bare resonance frequencies and spring constants are $f_{0_1} = 613$ kHz, $f_{0_2} = 636$ kHz and $k_1 = 7.7$ mN/m, $k_2 = 8.3$ mN/m, respectively. Inset: false-color SEM of NW1's MnAs tip with a 200 nm scale-bar. (b) Plot of the corresponding $\Delta f_i(B)$ simulated for a half-ellipsoid. Inset: schematic diagram of the half-ellipsoid geometry used to approximate the MnAs tip, where $a = 85$ nm, $b = 90$ nm, $c = 95$ nm. The simulation uses parameters for MnAs listed in Table (4.1) and the hard axis direction $\hat{\mathbf{k}}$ (purple arrow) is given by $\theta_K = 4.2^\circ$ and $\phi_K = 45.5^\circ$. Black dots and crosses indicate the position and direction of the sites of pinned magnetization. (c) Simulated magnetization configurations for B indicated by the dashed lines. Each cone, associated with a discretized volume, is color-coded with the magnitude of the magnetization component along $\hat{\mathbf{r}}_1$. Large black arrows indicate the net magnetization for $B = \pm 8$ T.

NW1: ideal easy plane. In Fig. 4.6(a), NW1 shows a particularly ideal magnetic response, in which the frequency shift of both modes asymptotically approaches the same negative value at high-field. This behavior indicates a MnAs particle with a hard axis along $\hat{\mathbf{n}}$ and no preferred easy axis in the r_1r_2 -plane. The DCM response of the MnAs tip, measured in Fig. 4.6(a) and shown in the inset, is simulated by approximating its shape as a half ellipsoid, with dimensions given in the inset of Fig. 4.6(b) and its caption. The excellent agreement between the measured and simulated $\Delta f_i(B)$, plotted in Figs. 4.6(a) and (b), respectively, allows us to precisely determine the direction of the magnetic hard axis \mathbf{K} . As expected, this axis is found to be nearly along $\hat{\mathbf{n}}$: just $\theta_K = 2.5^\circ$ away from $\hat{\mathbf{n}}$ and $\phi_K = 19.5^\circ$ from $\hat{\mathbf{r}}_1$.

Furthermore, as shown in Fig. 4.6(c), the simulations relate a specific magnetization configuration to each value of B . In this particular case, a stable vortex configuration in the easy plane is seen to enter (exit) from the edge in correspondence with the abrupt discontinuities in the eigenmodes' frequencies around +2 T (−2 T). Between these two fields, the vortex core moves from one side to the other, inducing several discontinuities in $\Delta f_i(B)$. The smoothness of the measured frequency shifts around $B = 0$ T indicates pinning of the vortex and is well-reproduced in the simulation by the introduction of two sites of pinned magnetization. This is modeled in *Mumax*³ by freezing the magnetization on a region of 4 cells (~ 10 nm \times 10 nm) along the entire tip's height. In one case the magnetization is fixed along $-\hat{\mathbf{n}}$ and in the other along $+\hat{\mathbf{n}}$. The second pinning point on the vortex trajectory⁴ is not crucial for the evolution of the reversal process but counteracts in terms of energy the presence of the first one, preserving the symmetry of the frequency shift asymptotes for both the negative and positive high field limit.

NW2: anisotropic easy plane. The majority of the measured NWs (10 out of 12) present DCM curves as shown by NW2 in Fig. 4.7(a). Despite the similarity of these curves to those shown in Fig. 4.6(a), no sharp discontinuity is observed upon sweeping B down from saturation (forward applied field). Furthermore, the high-field frequency shifts of both modes do not asymptotically approach the same negative value as in Fig. 4.6(a). Both of these effects can be explained by taking into account magnetic shape anisotropy in the MnAs tips (a similar result could be caused also by in-plane strain formed during the crystallization process). Despite the nearly perfect symmetry of NW1's tip, most of the crystallized MnAs droplets are asymmetric in the r_1r_2 -plane. This asymmetry introduces an effective magnetic easy axis in the r_1r_2 -plane. In fact, the measured $\Delta f_i(B)$ shown in Fig. 4.7(a) are well-reproduced by a simulation that takes into account the geometry of NW2's MnAs tip as observed by SEM. While small refinements in the microscopic geometry, which often cannot be confirmed by the SEM, affect how well the simulation matches every detail of the measured $\Delta f_i(B)$, the precise orientation of the hard axis and the direction of the effective shape anisotropy in the r_1r_2 -plane sensitively determine the curves' overall features (e.g. their high field asymptotes and shape).

In general, simulations show that shape anisotropy restricts the field range for a stable magnetic vortex to reverse applied field. In small forward applied field and in remanence, the magnetization evolves through a configuration with a net magnetic dipole in the r_1r_2 -plane. Only upon application of a reverse field, this configuration smoothly transform into a vortex⁵, resulting – for NW2 – in a subtle dip in $\Delta f_i(B)$

⁴See video NW1 in SI [25]

⁵See video NW2 in SI [25]

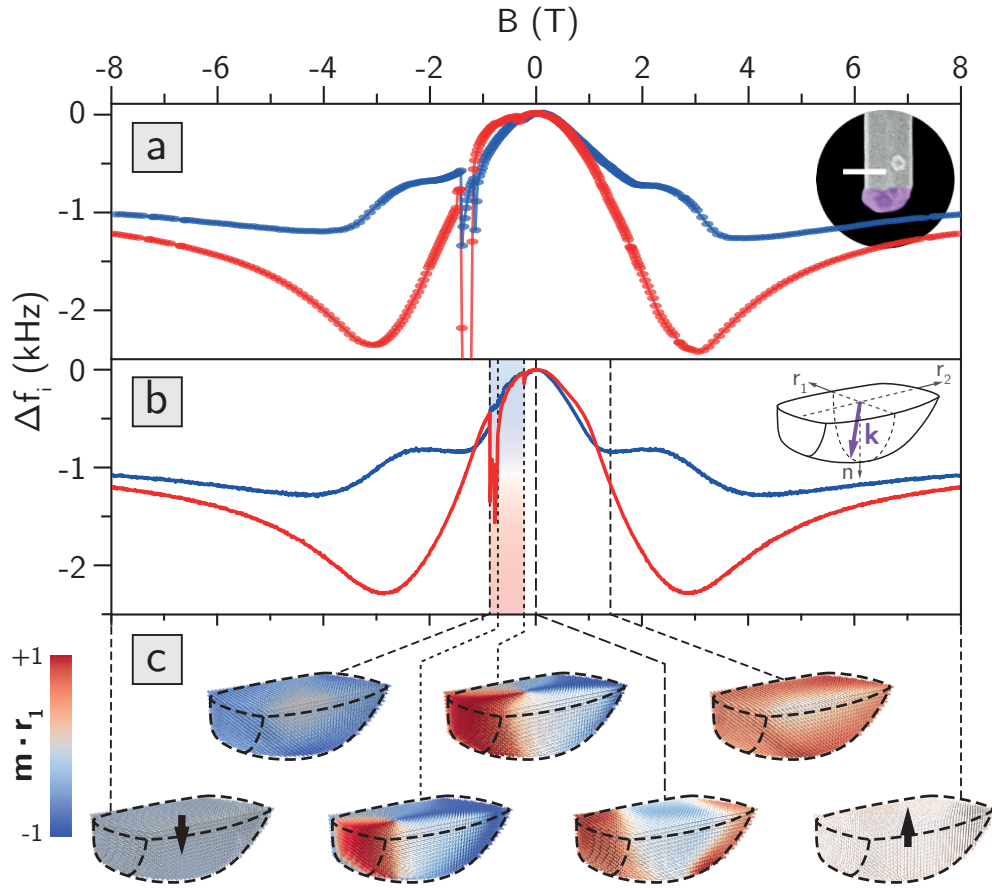


FIGURE 4.7 | **NW2 - MnAs tip magnetometry: zero field in-plane dipole.** (a) Plot of the $\Delta f_i(B)$ for $i = 1$ ($i = 2$) in blue (red), extracted at each B from the thermal displacement PSD. Inset: false-color SEM of NW2's MnAs tip with a 200 nm scale-bar. (b) Plot of the corresponding simulated $\Delta f_i(B)$. For NW2, the frequency shifts are calculated by using the mechanical characteristics extracted from its displacement noise spectrum, shown in Fig. 4.4. Inset: tip modeled as a truncated asymmetric ellipsoid of length $l = 230$ nm, width $w = 115$ nm, and depth $h = 110$ nm. The hard axis (purple arrow) is set to $\theta_K = 8^\circ$ and $\phi_K = -9.5^\circ$. (c) Simulated magnetization configurations for B indicated by the dashed lines. Large black arrows pointing out of plane indicate the net magnetization for $B = \pm 8$ T. Note that at zero field the tip presents a net magnetization lying entirely in-plane.

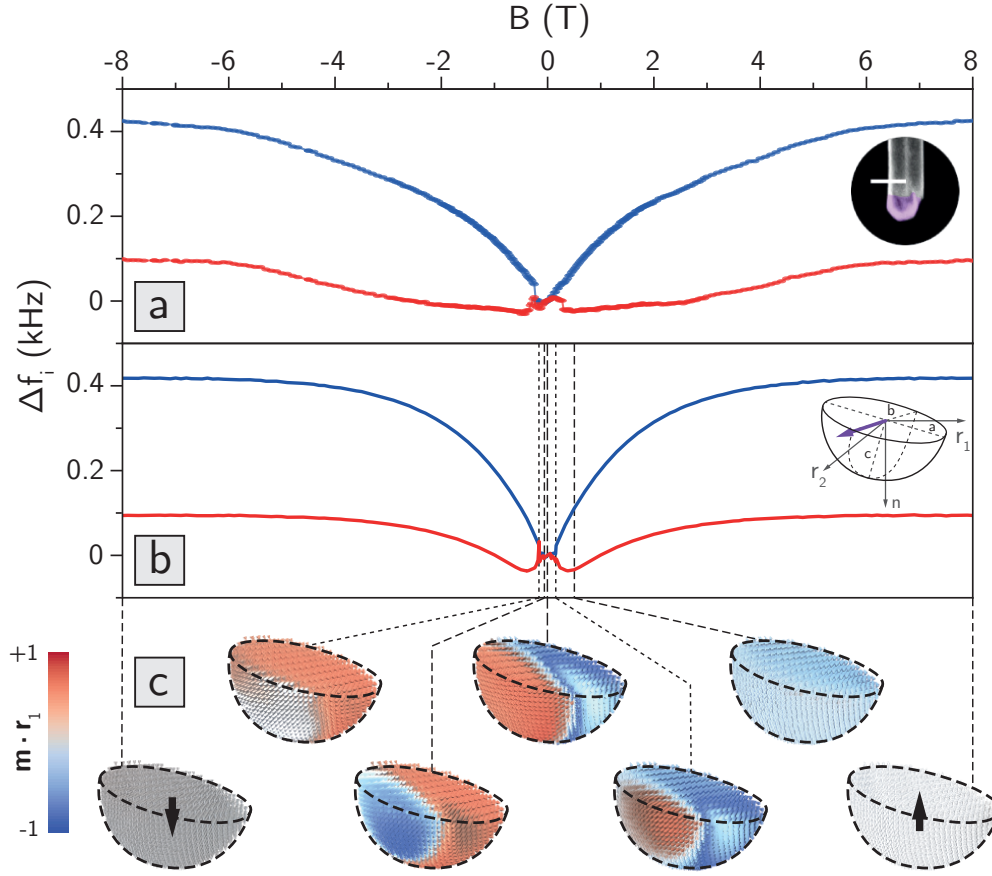


FIGURE 4.8 | **NW3 - MnAs tip magnetometry: anomalous hard axis tilt.**

(a) Plot of the $\Delta f_i(B)$ for $i = 1$ ($i = 2$) in blue (red), extracted at each B from the thermal displacement PSD. On the side: false-color SEM of NW2's MnAs tip with a 200 nm scale-bar. The bare resonance frequencies and spring constants are $f_{01} = 435$ kHz, $f_{02} = 447$ kHz and $k_1 = 14.3$ mN/m, $k_2 = 15$ mN/m, respectively. (b) Plot of the calculated $\Delta f_i(B)$. On the side: simulated tip's geometry approximated as an elongated ellipsoid with $a = b = 85$ nm and $c = 90$ nm and it is tilted with respect to the modes' reference system, so that its semi-axis c is tilted by $\theta_t = 20^\circ$ and $\phi_t = 210^\circ$ with respect to \hat{n} . The hard axis (purple arrow) is nearly perpendicular to \hat{n} with $\theta_K = 68.3^\circ$ and $\phi_K = 142.2^\circ$. (c) Simulated magnetization configurations for B indicated by the dashed lines. Each cell is color-coded with the magnitude of the magnetization component along \hat{r}_1 . Large black arrows indicate the net magnetization for $B = \pm 8$ T.

around $B = -0.3$ T. At a reverse field close to $B = -2$ T, an abrupt jump indicates the vortex's exit and the appearance of a single-domain state, which eventually turns toward \mathbf{B} . This analysis indicates that NW2's tip – as well as the majority of the MnAs tips – present a dipole-like remanent configuration pointing in the r_1r_2 -plane, rather than vortex-like configuration with a core pointing along $\hat{\mathbf{n}}$, as in NW1. Such remanent magnetic dipoles have been already observed by MFM in a previous batch of such NWs [35] and in analogous MnAs nanocrystals [155, 156].

NW3: tilted hard axis. In the rare case (1 of 12) of NW3 reported in Fig. 4.8 (a), we measure mostly positive $\Delta f_i(B)$ with different high-field asymptotes for each eigenmode. This behavior indicates a MnAs particle, whose hard axis points approximately in the r_1r_2 -plane. In fact, the features of the measured $\Delta f_i(B)$ in Fig. 4.8(b) are reproduced by simulating a nearly symmetric half-ellipsoid with a hard-axis lying at an angle $\theta_K = 68.3^\circ$ from $\hat{\mathbf{n}}$ and $\phi_K = 142.2^\circ$ from $\hat{\mathbf{r}}_1$. These data are clear evidence that crystallization of the liquid droplet can occasionally occur along a direction far off from the NW growth axis.

4.4 Dynamical current sensing

In order to test the behavior of these NWs as scanning magnetic sensors, we approach a typical one (NW2) to a current-carrying Au wire patterned on a SiO₂ substrate, as described in Fig. 4.9. Once in the vicinity of the wire constriction, the NW's two modes are excited by the Biot-Savart field \mathbf{B}_{AC} resulting from an oscillating drive current $I = I_1 \sin(2\pi f_1 t) + I_2 \sin(2\pi f_2 t)$, where $I_1 = I_2 = 50 \mu\text{A}$.

Single $10 \mu\text{m}$ -long line scans are acquired by moving the NW across the wire at the fixed tip-sample spacing $d_z = 250$ nm. This spacing is chosen to match the scanning probe's tip size, since getting closer would not improve its spatial resolution. Both the resonant frequencies f_i and displacement amplitudes r_i are tracked using two phase-locked loops (PLL) and the corresponding values of the force F_i driving each mode at resonance are then calculated as ⁶

$$F_i = \frac{k_i}{Q_i} r_i \quad (4.8)$$

Using an approach similar to that used to calibrate MFM tips [157, 158], we model the force exerted by a well-known magnetic field profile on the magnetic tip by using the so-called point-probe approximation. This approximation models the complex magnetization distribution of the tip as an effective monopole moment q_0 and a dipole moment \mathbf{m} located at a distance d from the tip apex (the monopole contribution compensates for the non-negligible spatial extent of the tip). The magnetic force acting on each mode is then given by $D_i = q_0 \mathbf{B}_{AC} \cdot \hat{\mathbf{r}}_i + \nabla(\mathbf{m} \cdot \mathbf{B}_{AC}) \cdot \hat{\mathbf{r}}_i$.

Moreover, we also consider the magnetic torque $\boldsymbol{\tau} = \mathbf{m} \times \mathbf{B}_{AC}$ generated at the tip, which results in a torsion and/or bending of the NW depending on its orientation. Although this contribution is negligible in MFM with conventional cantilevers, the short effective length of NWs ($l_e = 12.2 \mu\text{m}$) and soft spring constant ($k_1 \approx k_2 \approx 11$ mN/m), make the bending component of the torque responsible for an observable displacement along $\hat{\mathbf{r}}_i$, equal to $T_i = (l_e^{-1} \hat{\mathbf{n}} \times \boldsymbol{\tau}) \cdot \hat{\mathbf{r}}_i$.

⁶see Section 1.2.1

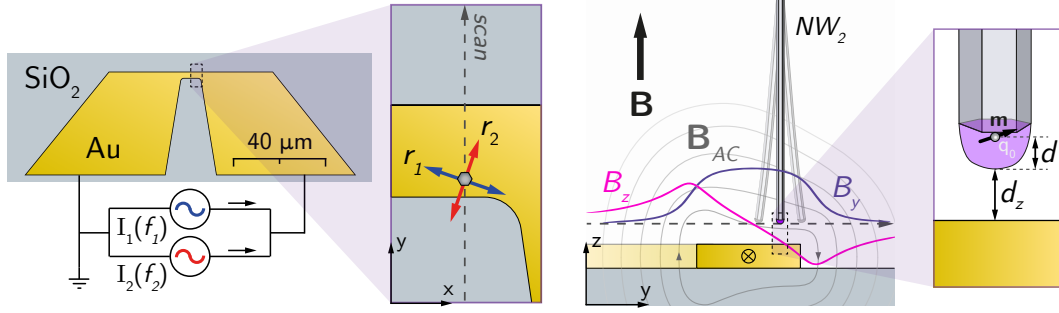


FIGURE 4.9 | **Sketch of the setup for dynamical current sensing**

Schematic drawing of the bottom sample consisting of a 240-nm-thick Au wire on an insulating SiO₂ substrate. NW₂ is approached on the constriction 3-μm-wide and 6-μm-long and scanned across it, with a tip-sample spacing $d_z = 250$ nm.

We then model the total force F_i driving each mode as

$$F_i = D_i + T_i = \left[q_0 \mathbf{B}_{AC} + \nabla(\mathbf{m} \cdot \mathbf{B}_{AC}) + \frac{1}{l_e} \hat{\mathbf{n}} \times (\mathbf{m} \times \mathbf{B}_{AC}) \right] \cdot \hat{\mathbf{r}}_i \quad (4.9)$$

The point-probe model is applied at a distance $d = 100$ nm from the tip (i.e. approximately at the base of the MnAs crystallite) for the best fits, while q_0 and \mathbf{m} are used as free parameters. The precise spatial dependence of the field \mathbf{B}_{AC} produced by the current I is calculated using the finite-element package *COMSOL* and is shown in Appendix D.

We characterize the NW magnetic response at $B = -5$ T and $B = 0$. In the high field case shown in Fig. 4.10(a), a fit of the two driving forces is obtained with an effective dipole \mathbf{m} nearly along \mathbf{B} with a magnitude $|\mathbf{m}| = 0.45 M_s V$, where $M_s = 1.005$ T is the saturation magnetization of MnAs and $V = 2.24 \times 10^{-21}$ m³ is the volume of the tip defined in the correspondent magnetometry simulation. In general, the estimation of V from SEM is approximate due to the difficulty in determining the precise three-dimensional geometry and in distinguishing regions of non-magnetic material inside the tip or at its surface. The fit returns a small, but non-zero q_0 and shows a very good agreement with the measured forces sensed by the two modes.

In Fig. 4.10(b), the same line scan is performed in absence of external field and, as expected, the observed response changes radically, since the magnetization lies mostly in the easy plane and is not completely saturated. In the fit, the effective dipole contribution is dominant and mostly orthogonal to the NW axis $\hat{\mathbf{n}}$ with $|\mathbf{m}| = 0.3 M_s V$. As an additional confirmation of the relevance of the magnetic torque at this scales, the direction of \mathbf{m} is closely related to the torque contribution making the fit particularly sensitive to the in-plane orientation $\phi_{\mathbf{m}}$ of the dipole term.

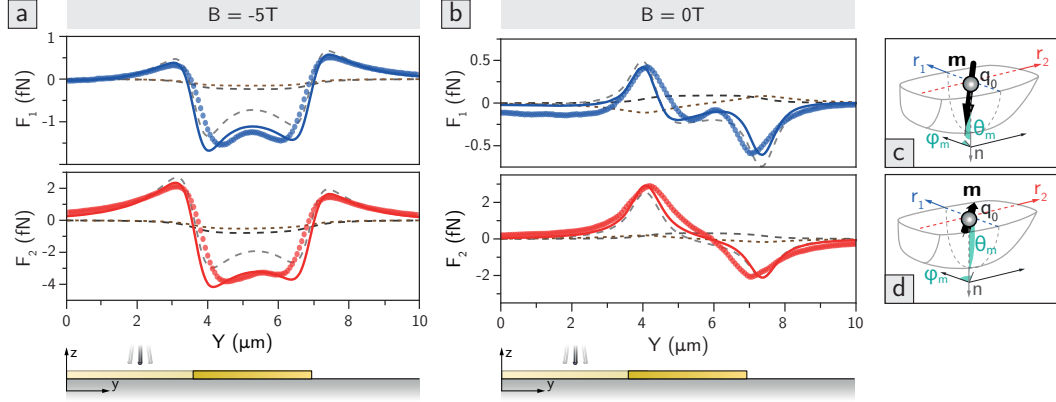


FIGURE 4.10 | **Characterization of NW2 as magnetic scanning probe.**

Plots of the measured (dotted line) and calculated (solid line) forces F_i driving the first (blue) and the second (red) mode over a 10 μm long line scan, as sketched in Fig. 4.9. For each plot, the three distinct drive contributions in Eq. (4.9) are shown as dashed lines: the monopole (black), dipole (gray) and torque (brown) terms. For the high magnetic field case in (a,c), the simulated response is fit by setting $q_0 = -1 \times 10^{-10}$ A·m, $|\mathbf{m}| = 8 \times 10^{-16}$ A·m² with $\theta_{\mathbf{m}} = 2^\circ$, $\phi_{\mathbf{m}} = 20^\circ$. For the zero field case in (b,d), fitting parameters are set to $q_0 = 4 \times 10^{-11}$ A·m, $|\mathbf{m}| = 5.3 \times 10^{-16}$ A·m² with $\theta_{\mathbf{m}} = 87^\circ$, $\phi_{\mathbf{m}} = 42^\circ$.

The results, obtained by using point-pole model for MFM probes, are entirely consistent with the DCM characterization of the MnAs tip obtained for NW2. However, this technique is dependent on the relation between the size of the tip and the scale of the field variation. In fact, the contribution of the single-pole and the dipole is sample dependent and changes with the tip-sample distance [159]. Despite the validity of the point-pole approximation at $d_z = 250$ nm, for future imaging application at smaller distances and to obtain quantitative understanding of MFM data, more robust and general tip calibration procedures have been proposed [160, 161]. Based on both numerical simulations and control experiments, using the applied magnetic field to initialize the MnAs tip magnetization along opposing directions, we find spurious electrostatic driving of the NW modes to be negligible.

4.4.1 Current sensitivity

The NWs' high force sensitivity combined with highly concentrated and strongly magnetized dipole-like tips gives them an exquisite sensitivity to magnetic field gradients. In order to quantify this sensitivity – according to the definition we gave in Section 1.2.3 – we restrict our attention to the second mode of NW2 (always plotted in red in this thesis), positioning it at the point of maximal response over the wire at $d_z = 250$ nm and $B = 0$ T (i.e. $y = 4.5$ μm on Fig. 4.10(b)). The displacement signal r_2 is measured with a lock-in amplifier while decreasing the driving current $I = I_2 \sin(2\pi f_2 t)$.

The sweeps plotted in Fig. 4.11(a) and (b) show the expected linear response as well as a wide dynamic range. In Fig. 4.11(b), we focus on the low-current regime, showing both the in-phase X (signal+noise) and quadrature Y (noise) response. By simple linear regression, we extract the signal as $\bar{X} = \beta I_2 / \sqrt{2}$, with a transduction factor $\beta = 0.26$ nm/ μA . The noise in both X and Y is found to be Gaussian and fully ascribable to the NW's thermal motion with variances $\sigma_X^2 \approx \sigma_Y^2 \approx S_{r_2}(\omega_2) \times \text{BW}_{\text{neq}}$,

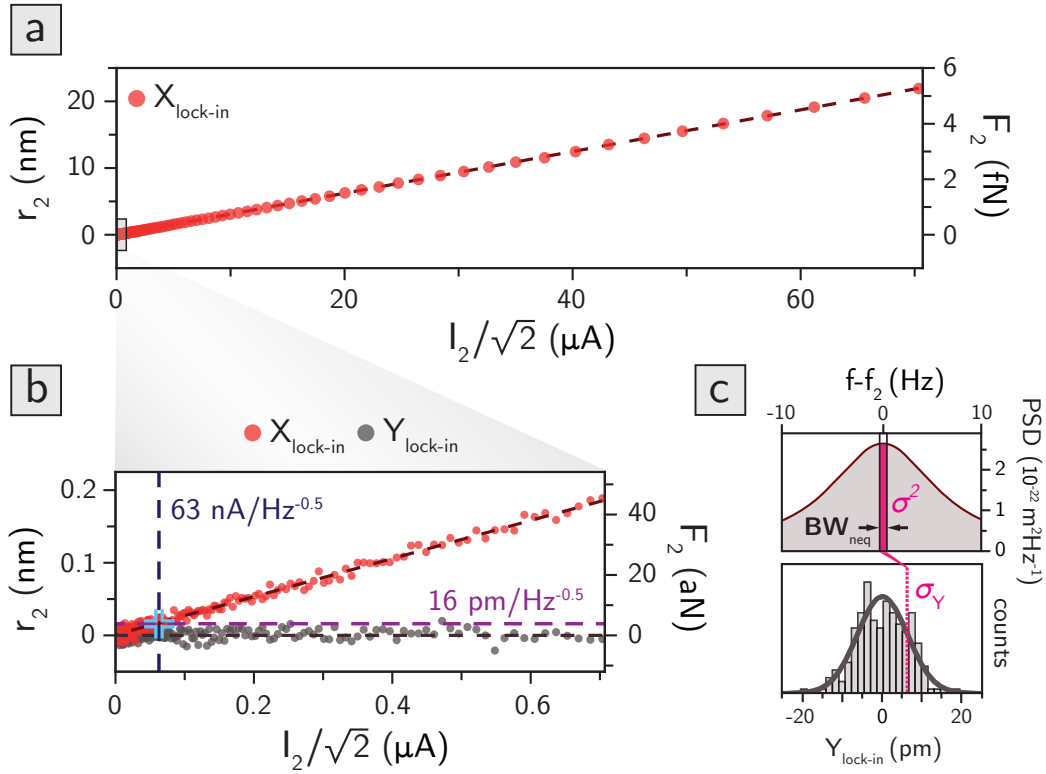


FIGURE 4.11 | **NW2 sensitivity to a resonant current drive at distance $d_z = 250 \text{ nm}$.**

(a) Plot of the oscillation amplitude r_2 for each value of the current amplitude I_2 , both quantities are root mean squared. (b) Plot of in-phase response to the drive (X) and quadrature signal (Y) for a finer current sweep from $I_2 = 1 \mu\text{A}$ to $I_2 = 1 \text{ nA}$. The lock-in demodulator low-pass filter noise equivalent bandwidth was set to $\text{BW}_{\text{neq}} = 0.156 \text{ Hz}$ and each point was averaged for 2.5 sec. Both signals are linearly fit (dark dashed lines). The intersection (light blue cross) between the linearly fit signal \tilde{X} and the displacement sensitivity (dashed purple line), shows a current sensitivity of $63 \text{ nA}/\sqrt{\text{Hz}}$ (dashed blue line). (c) Noise analysis on the quadrature channel Y. On top, a close-up of the second mode's PSD fit and the noise power $\sigma^2 = 4.2 \times 10^{-23} \text{ m}^2$ within the measurement bandwidth BW_{neq} . Below, the histogram of the noise measured on quadrature channel (Y) in (b), fitted by a Gaussian $\mathcal{N}(0, \sigma_Y)$ with $\sigma_Y = 6.5 \text{ pm} \sim \sqrt{\sigma^2}$, confirming the thermally limited nature of the sensitivity measurement.

where $S_{r_2}(\omega)$ is a fit to the second mode's thermal PSD shown in Fig. 4.11 (c), ω_2 is the resonant angular frequency of the second mode, and BW_{neq} is the lock-in's equivalent noise bandwidth. As shown in Fig. 4.11 (c) for Y, the mode's thermal PSD is assumed constant around its value at resonance $S_{r_2}(\omega_2) = 4k_B T \frac{Q_2}{k_2 \omega_2}$, due to the narrow measurement bandwidth. Therefore, the NW's second mode has a thermally-limited displacement sensitivity of $\sqrt{S_{r_2}(\omega_2)} = 16 \text{ pm}/\sqrt{\text{Hz}}$, equivalent to a force sensitivity of $\sqrt{S_{r_2}(\omega_2)} k_2 / Q_2 = 4 \text{ aN}/\sqrt{\text{Hz}}$. Given the measured current transduction factor β at the working tip-sample spacing $d_z = 250 \text{ nm}$, we obtain a sensitivity to current flowing through the wire of $63 \text{ nA}/\sqrt{\text{Hz}}$.

4.5 Discussion and outlooks

The measured sensitivity to electrical current compares favorably to that of other microscopies capable of imaging current through Biot-Savart fields, including scanning Hall microscopy, magneto-optic microscopy, scanning SQUID microscopy, microwave impedance microscopy, and scanning nitrogen-vacancy magnetometry [162, 163].

Because of the dipole-like character of the MnAs tip, this transduction of current into displacement is dominated by the effect of the time-varying magnetic field gradient generated by the current: $F_i \approx \nabla(\mathbf{m} \cdot \mathbf{B}_{\text{AC}}) \cdot \hat{\mathbf{r}}_i = \mathbf{m} \cdot \nabla(\mathbf{B}_{\text{AC}} \cdot \hat{\mathbf{r}}_i)$. Although the torque resulting from the time-varying magnetic field produces an effective force, T_i , as seen in Figs. 4.10 (a) and (b), this term is typically secondary. Therefore, from *COMSOL* simulations of the field produced by current flowing through the wire, we find this current sensitivity to correspond to a magnetic field gradient sensitivity of $11 \text{ mT}/(\text{m}\sqrt{\text{Hz}})$ at the position of the tip's effective point probe, i.e. $d_z + d = 350 \text{ nm}$ above the surface. The direction of this gradient sensitivity depends on the direction of the mode used.

Having quantified the NW's response to magnetic field gradients, we can calculate its sensitivity to other magnetic field sources, including a magnetic moment (dipole field), a superconducting vortex (monopole field), or an infinitely long and thin line of current [162]. In particular, following to the calculations carried out in Appendix E, we expect a moment sensitivity of $54 \mu_B/\sqrt{\text{Hz}}$, a flux sensitivity of $1.3 \mu\Phi_0/\sqrt{\text{Hz}}$, and line-current sensitivity of $9 \text{ nA}/\sqrt{\text{Hz}}$. These values show the capability of magnet-tipped NWs as probes of weak magnetic field patterns and the huge potential for improvement if tips sizes and tip-sample spacings can be reduced. Smaller magnetic tips may be produced using optimized growth processes or Focused Ion Beam (FIB) milling. Alternatively, the production of different types of magnet-tipped NWs could be attempted, through the evaporation of magnetic caps on sharp non-magnetic NWs [75] or by Focused Electron Beam Induced Deposition (FEBID) [164].

In addition to improved sensitivity, NW MFM provides other potential advantages compared to conventional MFM. First, scanning in the pendulum geometry with the NW oscillating in the plane of the sample has the characteristics of lateral MFM. This technique, which is realized with the torsional mode of a conventional cantilever, distinguishes itself from the more commonly used tapping-mode MFM in its ability to produce magnetic images devoid of spurious topography-related contrast and in a demonstrated improvement in lateral spatial resolution of up to 15% [165]. Second, the nanometer-scale magnetic particle at the apex of the NW force sensor minimizes the size of the MFM tip, allowing for optimal spatial resolution and minimal perturbation of the investigated sample. In fact, the stray field from small magnetic tips falls off more rapidly in space than for large tips and therefore produces less field at the sample than a large tip at the same spacing. In this way, smaller tips are less invasive and are less likely to alter the sample magnetization or current distribution. Since the

NWs are much more sensitive forces sensors than conventional cantilevers, they will respond mechanically even for such small interaction forces.

The prospect of increased sensitivity and resolution, combined with few restrictions on operating temperature, make NW MFM ideally suited to investigate nanometer-scale spin textures, skyrmions, superconducting and magnetic vortices, as well as ensembles of electronic or nuclear spins. Such magnetic tips may also open opportunities to study current flow in 2D materials and topological insulators. The ability of a NW sensor to map all in-plane spatial force derivatives [23, 33] should provide fine detail of stray field profiles above magnetic and current carrying samples, in turn revealing information on the underlying phenomena and anisotropies. Directional measurements of dissipation may also prove useful for visualizing domain walls and other regions of inhomogeneous magnetization. As shown by Grutter et al., dissipation contrast, which maps the energy transfer between the tip and the sample, strongly depends on the sample's nanometer-scale magnetic structure [166].

Chapter 5

Conclusions and future directions

The study of nano-mechanical resonators represents a central aspect of several rapidly expanding and promising areas of research and it is boosted by continuous advances in nanotechnology and material science. In fact, nano-mechanical devices do not only stand out for their exquisite force sensitivity but also offer a versatile platform to interface with other physical systems. Upon functionalization, such sensitive force detectors can respond to electric, magnetic and optical forces leading to a widespread number of applications down to the quantum regime, where they can provide a read-out of static and dynamic properties of the quantum systems or mediate interactions between physically distinct systems [167]. Moreover, ‘bottom-up’ fabrication techniques of nano-structures have given the possibility to further reduce the resonators’ size, maintaining a high level of quality and control of their chemical structure and opening up new possibilities for integrated functionalization. As a proof of the potential of ‘bottom-up’ resonators, a thermally limited force resolution close to $1 \text{ zN}/\sqrt{\text{Hz}}$ has been demonstrated for a doubly-clamped suspended CNT [18], i.e. more than 100 times better the record using ‘top-down’ transducers. However, despite their outstanding properties, CNTs oscillators can exhibit non-linear behavior even under low-temperature thermal excitation and require elaborated detection schemes which make them extremely difficult to use as scanning force sensors. NWs oscillators, on the other hand, show a wide linear dynamic range and have a more versatile and controllable structure, which offers an advantageous trade-off between low masses (high sensitivity) and ease of use as scanning force sensors. In fact, their singly clamped geometry can be arranged as pendulum cantilever and allows for a ‘straightforward’ optical detection of their motion.

Inspired by *Nichol et al.* seminal works [24, 29], in this thesis we have explored some of the opportunities given by *as-grown* NWs in the field of scanning force sensing. First, we have built a cryogenic scanning probe microscope setup capable to detect and characterize NW force sensors directly from their original growth substrate. The fiber-based confocal reflection microscope allows to navigate the sample by imaging individual NWs and to measure their displacement with a noise floor of $0.4 \text{ pm}/\sqrt{\text{Hz}}$ for $25 \text{ }\mu\text{W}$ of incident power. In addition, interferometry ensures highly sensitive motion detection along the optical axis and precise displacement calibration. By controlling the position of the NW respect to the focus or by detuning the laser wavelength, the projective measurement of its 2D motion can be acquired along arbitrary directions, spatially mapping the two orthogonal polarization directions of the first flexural mode. In direct analogy with lateral AFM, we demonstrated a highly sensitive vectorial force microscopy technique using the NW’s nearly degenerate modes as a bi-dimensional force transducers, capable to simultaneously map planar force gradients [33]. A complete study of the static tip-sample interaction force gradients has been carried out by using the thermal force noise as a broadband isotropic driving force and the 2D

force field has been calculated via numerical integration. Then, we showed the capabilities of dynamic vectorial sensing by recording the response of each mode to a resonant voltage signal to map force fields generated by NW spurious surface charges and polarizability. The universality of the vectorial force detection scheme with a NW enriches the surface imaging techniques with an extra dimension and provides a sensitivity several order of magnitudes better than commercial AFM, which could be employed to study very weak proximity forces at the nanoscale, such as Casimir forces. Higher force sensitivity translates into more sensitive measurements of dissipation and non-contact friction, which could in principle shed light on concepts such as superlubricity and atomic-scale friction by mapping the directional dependence of dissipation.

In the last part of the thesis, as evidence of the great potential of NWs functionalization, we described the use of a MBE grown GaAs NW with integrated crystalline MnAs tip as a magnetic force sensor. By monitoring each mode in a static magnetic field, we characterized the MnAs nano-magnet at the tip via dynamic torque magnetometry, showing excellent agreement with micro-magnetic simulations. Such NWs resulted to be promising probes for dynamic current sensing showing a sensitivity of $63 \text{ nA}/\sqrt{\text{Hz}}$, which could be used to study current flow in 2D materials and topological insulators. Due to the strong hard-axis anisotropy of ferromagnetic MnAs, most of the tips displayed an extended dipole configuration of the remanent net magnetization lying in the easy-plane, which would permit to achieve higher spatial resolution compared to the usual monopole-like interaction of standard MFM tips [168]. In fact, for future improved MFM setups, one frequently discussed approach is to place nano-magnets directly on the apex of cantilever tips [162]. This would serve three goals: improved spatial resolution, improved spin sensitivity and improved interpretability, since the magnetic moment of the deposited nano-magnets would have a narrow distribution. In this direction, our NWs tipped with a self-assembled MnAs tip represent an ideal candidate, although the magnet size needs to be further reduced. We have conducted preliminary experiments in this regard by milling with a focused ion beam (FIB) the tips to less than half their volume and increasing at the same time their aspect ratio in order to introduce an additional shape anisotropy term in the easy-plane to further stabilize the dipole orientation. The dynamic torque magnetometry measurements of the modified NWs, reported in Appendix F, show a lower asymptotic value and a smoother behavior of the frequency shifts as a function of the applied field, confirming a reduction in the magnetic volume ($\Delta f_{\text{asym}} \propto V$) and in the complexity of the magnetization states, respectively. We aim to take advantage of the high force sensitivity of these NWs to detect very small interactions between a tiny magnetic volume at the tip and samples such as nanometer-scale spin textures, skyrmions, superconducting and magnetic vortices. To do so, it will be necessary to implement a calibration method for a quantitative measurement of the magnetostatic potential detected by the 2D NW sensor, based on a tip's transfer function model in Fourier space [159, 168]. Additionally, the magnetic vortex remanent state shown by few of the MnAs tips (see Fig. 4.6), can also have interesting implications in MFM applications. In fact, the net contribution to the MFM signal is just given by the central vortex core, leading to an effective increase of the spacial resolution. This is confirmed by the results presented in Appendix G, where the NW with a 'vortex' tip is scanned at room temperature over permalloy micro-disk in a remanent vortex state itself, producing features with much smaller width respect to the physical extension of the tip. Most notably, the disk's center core is resolved with a width of 75 nm, in contrast with a tip size of 230 nm. Despite the fascinating possible developments of such vortex-MFM mode which needs deeper investigation, the technique is limited

by the mobility of the vortex core in the tip at low temperatures, induced by the interaction with the sample's stray field. It is important to remark that a strong stray field emerging from a tip can affect the sample's configuration, or viceversa, undermining the measurement interpretation. This limitation could be overcome by using NWs with 'soft' tips made of paramagnetic/superparamagnetic material with a large magnetic susceptibility such as iron oxide.

Furthermore, the use of alternative types of magnetic-tipped nanomechanical resonators could be attempted. In particular, focused electron beam induced deposition (FEED) is a powerful technique to grow NWs with high aspect ratios being able to freely combine magnetic material such as cobalt or iron and non-magnetic such as platinum [164]. In this respect, we have performed preliminary dynamic torque magnetometry measurements on both cobalt and iron FEED grown NWs, confirming their magnetism and good force sensitivity of about $10 \text{ aN}/\sqrt{\text{Hz}}$ (at 4.2 K), although limited by a modest mechanical $Q \sim 1000$. Interestingly, it has been shown that a high temperature annealing of these NWs improves both their magnetic purity and nanocrystalline structure, which could lead to an enhancement of their mechanical properties [169]. FEED is also a versatile tool to functionalize NWs and CNTs allowing to grow a magnetic nano-particle at arbitrary positions on the mechanical resonator and opening up new intriguing possibilities for the creation of ultra-sensitive magnetic scanning probes.

Appendix A

Low temperature nanowire microscope

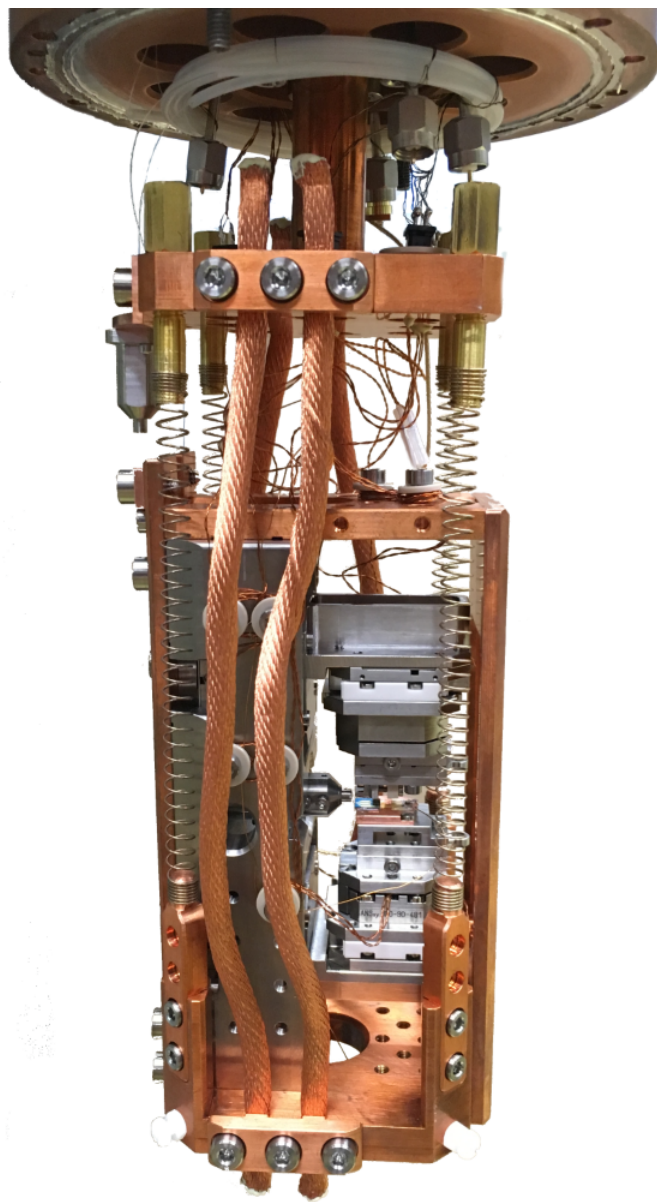


FIGURE A.1 | **Photograph of the actual microscope.**
Side view

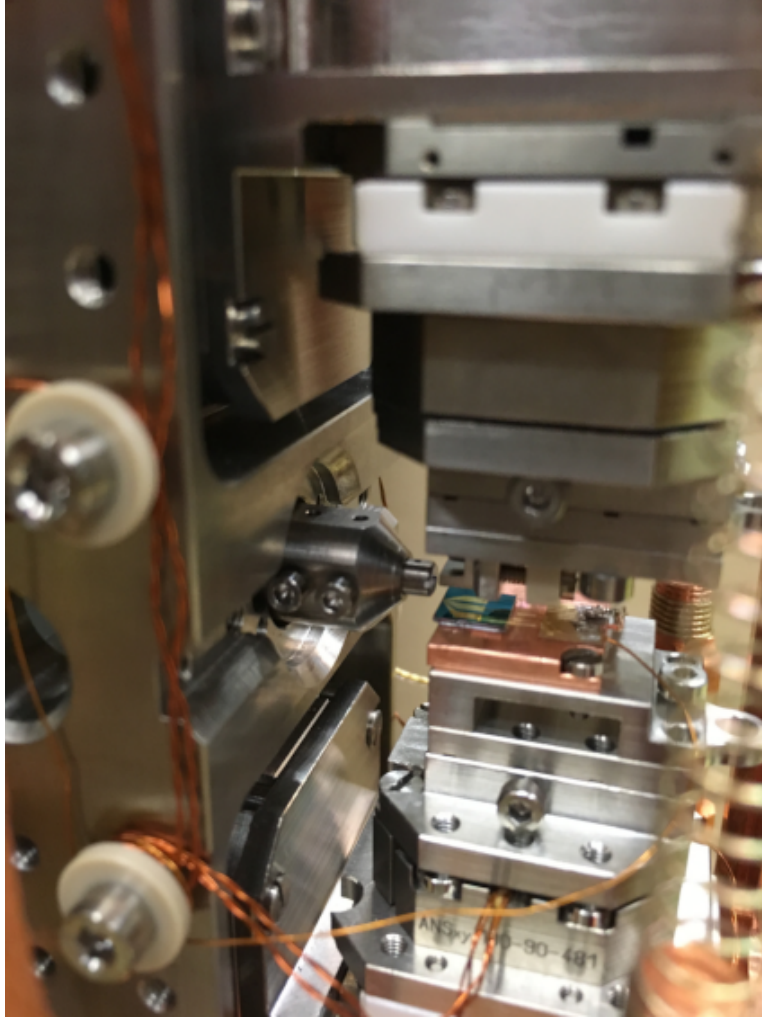


FIGURE A.2 | **Zoom on the central sample region**

The photograph has been taken after focusing the laser on a single NW from the chip (not visible) glued on the L-shaped holder on the upper piezo stack. The focal length $f_1 = 1.45$ mm of the focusing lens guarantees enough room for safely approaching and scanning the bottom sample against the NW sensor.

On the bottom piezo-stack is visible the silicon chip with the gold microwire used for the generation of an AC magnetic field in the experiment presented in Chapter 4.

Appendix B

NWs sample fabrication procedure

The scanning NWs sample preparation aims to minimize unnecessary steps involving manipulation and gluing of the NWs, in order not to spoil their mechanical properties. For this reason, MBE grown NWs are kept on their original growth substrate taking advantage of their singly clamped geometry, epitaxially registered to the substrate. We measured quality factor about 5 times higher than the ones obtained for similar NWs, when individually glued on a sharp edge [34].

Here below are summarized the main steps of the fabrication procedure:

1. the wafer is fixed on a glass slide with double sided carbon tape to obtain a smaller piece of about $1 \times 2 \text{ mm}^2$. After locating an area of moderate NWs density (e.g. Fig B.1(a)), the substrate is cleaved laterally by marking the side with a fine manual diamond scribe and then applying pressure with a sharp scalpel blade. The tape helps to keep the wafer's fragments in place, while lateral cleaving prevents substrate debris from contaminating the sample;

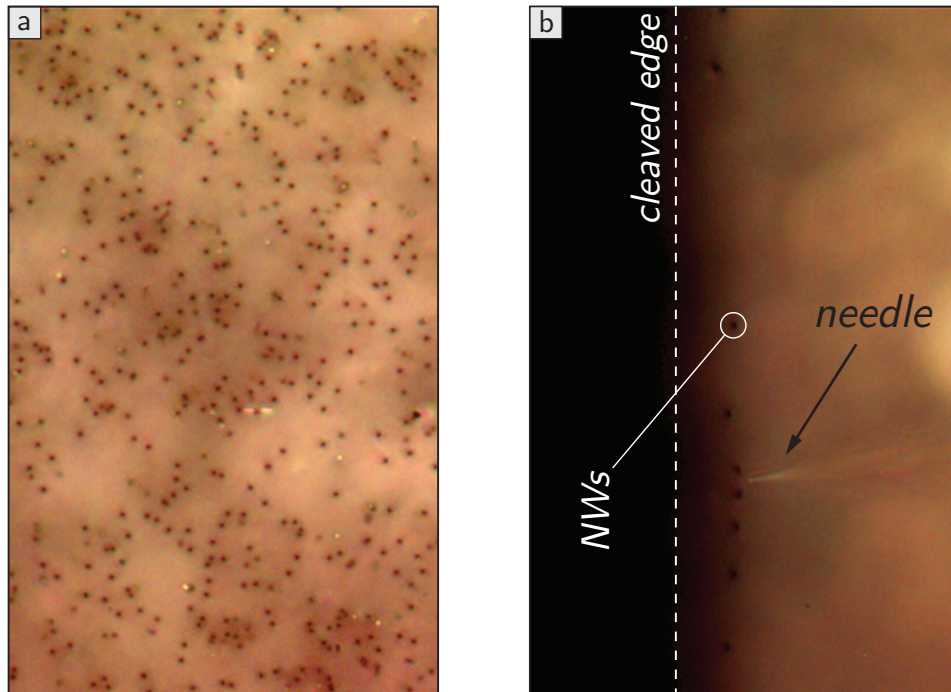


FIGURE B.1 | **Scanning NWs sample preparation under an optical microscope.**

(a) Initial stage: top view of the original growth wafer (b) Final stage: individual removal of unwanted NWs along the cleaved edge by means of the micro-manipulator's needle.

2. the obtained small chip is fixed with carbon tape on a new glass slide and mounted on a system of manual micro-metric stages which allows to approach a very sharp blade perpendicularly to the substrate and remove the excess of NWs within around 10 μm distance from the chosen reference edge. Operations are performed under a microscope with very large working distance;
3. remaining shorter and tilted NWs are individually removed by using a micro-manipulator station under an optical microscope with a high magnification objective. When a single row of NWs standing along the chip edge is obtained (Fig. [B.1\(b\)](#)), the sample is imaged at the SEM for more detailed NWs selection. Further unwanted NWs are then removed.
4. The final chip is glued with a low outgassing epoxy on the L-shaped titanium mount in Fig. [2.2\(c\)](#).

Appendix C

Micromagnetic simulations for NW magnetometry

The core of the simulation is the calculation of the magnetic energy of the MnAs tip for each value of the applied external field and for small tilt angles around the oscillation axis of each NW mode ($\hat{\mathbf{r}}_1, \hat{\mathbf{r}}_2$). To define the problem's geometry, every vectorial quantity is expressed in spherical coordinates and referred to a orthogonal coordinate system formed by the direction of the two modes of oscillation $\hat{\mathbf{r}}_i$ and the NW axis $\hat{\mathbf{n}} = \hat{\mathbf{r}}_1 \times \hat{\mathbf{r}}_2$. As sketched in Fig. C.1, for each NW we consider the hard axis direction $\hat{\mathbf{k}}$ (θ_K, ϕ_K), a small misalignment between $\hat{\mathbf{n}}$ and the external magnetic field $\hat{\mathbf{B}}$ (θ_B, ϕ_B) and the orientation axis of the tip itself $\hat{\mathbf{t}}$ (θ_t, ϕ_t) with respect to the NW axis.

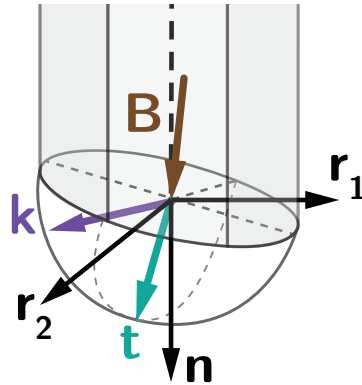


FIGURE C.1 | Geometry of MnAs tip's simulation parameters

| | $\hat{\mathbf{k}} (\theta_K, \phi_K)$ | $\hat{\mathbf{B}} (\theta_B, \phi_B)$ | $\hat{\mathbf{t}} (\theta_t, \phi_t)$ |
|-----|---------------------------------------|---------------------------------------|---------------------------------------|
| NW1 | (4.2°, 45.5°) | (2.5°, 160.5°) | (4.7°, 170°) |
| NW2 | (8°, -9.5°) | (2.5°, 110.5°) | (0°, 0°) |
| NW3 | (68.3°, 142.2°) | (5°, 137°) | (20°, 210°) |

TABLE C.1 | Angles giving the best fit to data for each NW.

The deviation of the magnetic field with respect to the NW axis accounts for an imperfect perpendicular growth of each NW with respect to the substrate and for a small tilt angle of 2° along the optical axis $\hat{\mathbf{y}}$ of the NWs' chip holder. Such design

of the holder ensures that the NWs on the edge of the chip are the first objects on the chip to approach the bottom sample, avoiding any unwanted contact due to an imperfect parallelism between the two.

Appendix D

Microwire's magnetic field

In order to calibrate the NW magnetic response over the line scan, the monopole and dipole terms (q_0 and \mathbf{m} respectively) are extracted from the complete driving force expression for each mode: $F_i = q_0 \mathbf{B}_{AC} \cdot \hat{\mathbf{r}}_i + \nabla(\mathbf{m} \cdot \mathbf{B}_{AC}) \cdot \hat{\mathbf{r}}_i + l_e^{-1}(\hat{\mathbf{n}} \times (\mathbf{m} \times \mathbf{B}_{AC})) \cdot \hat{\mathbf{r}}_i$. The Biot-Savart field \mathbf{B}_{AC} , generated by a current oscillating at the modes' frequencies in the golden microwire, is calculated by the finite element simulation program *COMSOL*.

The (x, y) coordinates of the line scan with respect to the center of the wire are estimated by the direct imaging of the sample's topography, as shown in Chapter 3. Conversely, along $\hat{\mathbf{z}}$, the distance $d_z = 250$ nm between the wire and NW's tip is determined with a soft-touch onto the sample and consequent retraction by the desired amount with the z -axis piezo scanner (the absence of a direct calibration for this open-loop might introduce an error in the distance estimation around $\pm 10\%$).

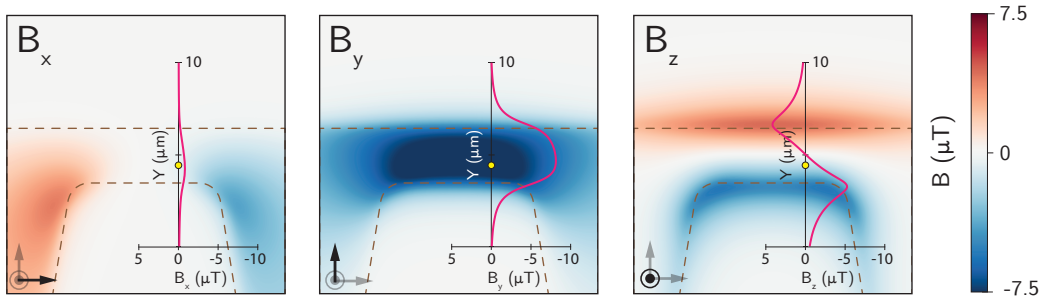


FIGURE D.1 | **Simulated magnetic stray field of the current carrying wire.**

The field is calculated at the point model's distance from the wire ($d_z + d = 350$ nm) and for a current $I_{DC} = 50/\sqrt{2}$ μA flowing in $+x$ direction, used to fit the measured driving forces F_i for NW2. The field components are individually color plotted over a $15 \mu\text{m} \times 15 \mu\text{m}$ area centered above the Au wire constriction (dashed brown line contour). Each inset plots the value of the field component in correspondence of the acquired $10 \mu\text{m}$ -long line scan reported in Fig. 4.10. The sensitivity measurement has been performed at $y = 4.5 \mu\text{m}$, as indicated by the yellow circles.

Given the μm -sized dimension of the wire and the modest frequencies around 500 kHz, the impedance of the wire is frequency independent, with a negligible reactive part; this fact allows us to approximate the problem with the static case where a DC current $I_{DC} = I_{AC}/\sqrt{2}$ flows in the wire. Following our point-probe approximation of the magnetic tip behavior, the best fit with the data is obtained by taking the stray field calculated at a distance $d = 100$ nm from the tip's apex.

Appendix E

Sensitivity to different types of magnetic field sources

In the experiments described in Chapter 4, we find that our magnet-tipped NW has a thermally-limited displacement (force) sensitivity of $16 \text{ pm}/\sqrt{\text{Hz}}$ ($4 \text{ aN}/\sqrt{\text{Hz}}$) at $T = 4.2 \text{ K}$. Given the measured current transduction factor $\beta = 0.26 \text{ nm}/\mu\text{A}$ at the working distance $d_z = 250 \text{ nm}$, we obtain a sensitivity to current flowing through our lithographically patterned wire of $63 \text{ nA}/\sqrt{\text{Hz}}$. Because of the dipole-like character of the MnAs tip, this transduction of current into displacement is dominated by the effect of the time-varying magnetic field gradient generated by the current at the position of the tip: $F_i \approx \nabla(\mathbf{m} \cdot \mathbf{B}_{\text{AC}}) \cdot \hat{\mathbf{r}}_i = \mathbf{m} \cdot \nabla(\mathbf{B}_{\text{AC}} \cdot \hat{\mathbf{r}}_i)$. As discussed in the main text, the torque resulting from the time-varying magnetic field acting on the tip also produces an effective force, $T_i = l_e^{-1}(\hat{\mathbf{n}} \times (\mathbf{m} \times \mathbf{B}_{\text{AC}})) \cdot \hat{\mathbf{r}}_i$, but this term is typically secondary. Therefore, in the following analysis we restrict ourselves to considering the role of the magnetic field gradient. From the field profile simulations in Appendix D, that the measured current sensitivity translates into a sensitivity to magnetic field gradient of $G_{\text{min}} = 11 \text{ mT}/(\text{m}\sqrt{\text{Hz}})$ at the position of the tip's effective point probe, i.e. $d_z + d = 350 \text{ nm}$ above the surface and $y = 4.5 \mu\text{m}$, as indicated in Fig. D.1.

As a result, in addition to knowing the sensitivity to the specific current distribution flowing through our lithographically defined wire, we can now calculate the NW's sensitivity to other sources of magnetic field. We simply need to calculate the appropriate magnetic field gradient for each field source at the position of the probe and compare it to the demonstrated gradient sensitivity. For a tip with both its dipole moment and one of its modes oriented along $\hat{\mathbf{x}}$, the relevant component of the field gradient is $\hat{\mathbf{x}} \cdot \nabla(\mathbf{B}_{\text{AC}} \cdot \hat{\mathbf{x}}) = \partial B_{\text{AC},x}/\partial x$. Then, following a similar treatment by Kirtley [162] for magnetic scanning probes, we calculate the NW's expected sensitivity to a magnetic moment (dipole field), a superconducting vortex (monopole field), and an infinitely long and thin line of current (Biot-Savart field).

Magnetic dipole field. A magnetic moment \mathbf{M} generates a magnetic field,

$$\mathbf{B}_M(\mathbf{r}) = \frac{\mu_0}{4\pi} \frac{3\hat{\mathbf{r}}(\hat{\mathbf{r}} \cdot \mathbf{M}) - \mathbf{M}}{r^3}, \quad (\text{E.1})$$

where \mathbf{r} is the distance from the moment to the position of the probe and μ_0 is the permeability of free space. If \mathbf{M} is made to flip up and down along the $\hat{\mathbf{z}}$ direction, e.g. using magnetic resonance pulses as in magnetic resonance force microscopy [170], it generates a time-varying gradient, $\partial B_{\mathbf{M},x}/\partial x$. The amplitude of this gradient component is maximum directly above or below the magnetic moment ($x = y = 0$) and

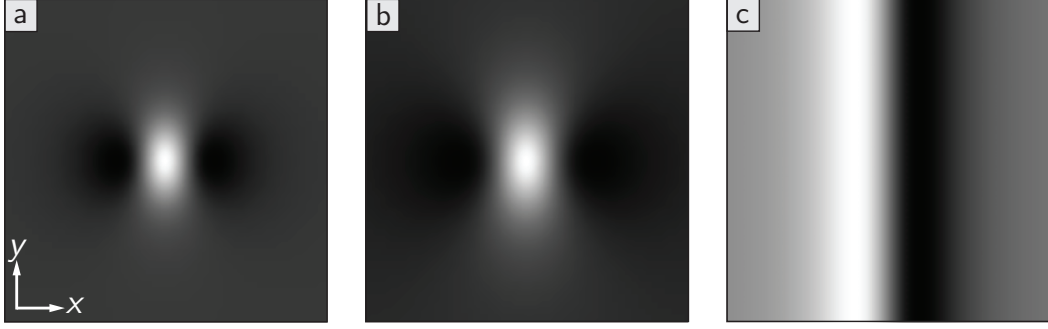


FIGURE E.1 | **In-plane magnetic field gradient due to different sources**
 (a) $\partial B_{M,x}/\partial x$ resulting from a single electron at the origin with moment $\mu_B \hat{\mathbf{z}}$. (b) $\partial B_{\Phi_0,x}/\partial x$ resulting from a single superconducting vortex at the origin. (c) $\partial B_{I,x}/\partial x$ for $I = 1$ A of current flowing through an infinitely long and thin wire along $\hat{\mathbf{y}}$. All plots show the gradient component in gray-scale in the $z = 350\text{nm}$ plane over a range of $2 \times 2 \mu\text{m}$.

has the following dependence on the vertical distance z :

$$\left(\frac{\partial B_{M,x}}{\partial x} \right)_{\text{max}} = \frac{3\mu_0}{4\pi} \left(\frac{M}{z^4} \right). \quad (\text{E.2})$$

We now take the maximum gradient component generated by a single electron, whose moment is given by the Bohr magneton μ_B . By comparing this term to our measured gradient sensitivity G_{min} , we find a sensitivity to magnetic moment in terms of $\mu_B/\sqrt{\text{Hz}}$:

$$M_{\text{min}} = G_{\text{min}} \left/ \left(\frac{\partial B_{\mu_B,x}}{\partial x} \right)_{\text{max}} \right. = \frac{4\pi}{3\mu_0} \left(\frac{G_{\text{min}}}{\mu_B} \right) z^4. \quad (\text{E.3})$$

If we assume the same tip-sample spacing as in our measurements of current flowing through our lithographically patterned wire, $z = d_z + d = 350 \text{ nm}$, we find $M_{\text{min}} = 54 \mu_B/\sqrt{\text{Hz}}$.

Magnetic monopole field. A superconducting vortex is modeled as a magnetic monopole and generates a field,

$$\mathbf{B}_{\Phi_0}(\mathbf{r}) = \frac{\Phi_0}{2\pi r^2} \hat{\mathbf{r}}, \quad (\text{E.4})$$

where \mathbf{r} is the distance from the vortex to the position of the probe and $\Phi_0 = h/(2e)$ is the magnetic flux quantum. If the position of this vortex is modulated, it will generate a time-varying gradient, $\partial B_{\Phi_0,x}/\partial x$. As before, the amplitude of this component is maximum directly above or below the vortex ($x = y = 0$) and has the following dependence on the vertical distance z :

$$\left(\frac{\partial B_{\Phi_0,x}}{\partial x} \right)_{\text{max}} = \frac{\Phi_0}{2\pi} \left(\frac{1}{z^3} \right). \quad (\text{E.5})$$

The sensitivity to magnetic flux in terms of $\Phi_0/\sqrt{\text{Hz}}$ is then given by,

$$\Phi_{\text{min}} = G_{\text{min}} \left/ \left(\frac{\partial B_{\Phi_0,x}}{\partial x} \right)_{\text{max}} \right. = 2\pi \left(\frac{G_{\text{min}}}{\Phi_0} \right) z^3. \quad (\text{E.6})$$

Again, by assuming the same tip-sample spacing as in our measurements, $z = d_z + d = 350$ nm, we find $\Phi_{\min} = 1 \mu\Phi_0/\sqrt{\text{Hz}}$.

Infinite 1D current line Finally, we calculate the expected sensitivity to an infinite line of current \mathbf{I} generating a field,

$$\mathbf{B}_I(\mathbf{r}) = \frac{\mu_0}{2\pi} \frac{\mathbf{I} \times \hat{\mathbf{r}}}{|\hat{\mathbf{I}} \times \mathbf{r}|}, \quad (\text{E.7})$$

where \mathbf{r} is the distance from the current line to the probe position and $\mathbf{I} \parallel \hat{\mathbf{y}}$. By modulating I , one can generate a time-varying gradient, $\partial B_{I,x}/\partial x$. The amplitude of this component is maximum in the planes defined by $x = \pm z/\sqrt{3}$. In those planes, I produces a maximum gradient amplitude with the following dependence on z :

$$\left(\frac{\partial B_{I,x}}{\partial x}\right)_{\max} = \frac{3\sqrt{3}\mu_0}{16\pi} \left(\frac{I}{z^2}\right). \quad (\text{E.8})$$

The resulting sensitivity to a line of infinite current in terms of $\text{A}/\sqrt{\text{Hz}}$ is given by,

$$I_{\min} = G_{\min} \left/ \left(\frac{\partial B_{I,x}}{\partial x}\right)_{\max} \right. = \frac{16\pi}{3\sqrt{3}\mu_0} \left(\frac{G_{\min}}{I}\right) z^2, \quad (\text{E.9})$$

where $I = 1$ A. Assuming the same tip-sample spacing as in our measurements, $z = d_z + d = 350$ nm, we find $I_{\min} = 9 \text{ nA}/\sqrt{\text{Hz}}$.

Note the better sensitivity of the NW to an infinitely long and thin line of current than to the test currents of our experiments, which are distributed across a wider wire. It is also interesting to note the different scaling exponents of the tip-sample spacing in the expressions for the sensitivity to the difference field sources. The magnetic moment, superconducting vortex, and current line sensitivity scale with the 4th, 3rd, and 2nd power of z , respectively. In particular, sensitivity to magnetic moment could be greatly improved by smaller tip-sample spacing. The gain in the magnetic field gradient ($\propto z^{-4}$) should more than compensate for the reduction of the effective tip moment interacting with the sample moment (roughly $\propto z^3$).

Appendix F

Magnetometry of GaAs NW with FIBbed MnAs tips

In order to study the behavior of smaller magnetic tips we have milled the MnAs nano-crystal with a focused ion beam (FIB) to less than half their volume. The FIB milling scheme in Fig. F.1(c) aims to increase the aspect ratio by leaving a slab ~ 70 nm thick of the previous round magnetic crystal, in order to introduce an additional shape anisotropy term in the easy-plane to further stabilize the dipole orientation. The dynamic torque magnetometry measurements of the modified NWs (e.g. Fig. F.1(a,b)) show a lower asymptotic value of the frequency shift due to the proportionality between Δf_{asyn} and magnetic volume in the high field limit. Since the typical asymptotic shift is reduced of about 5 times, we suppose a deterioration of the tip magnetism on the outer volume caused by the FIB milling process. The frequency shift curves show a smoother behavior with a reduced number of discontinuities confirming a reduced complexity of the magnetization states, during the magnetization reversal process.

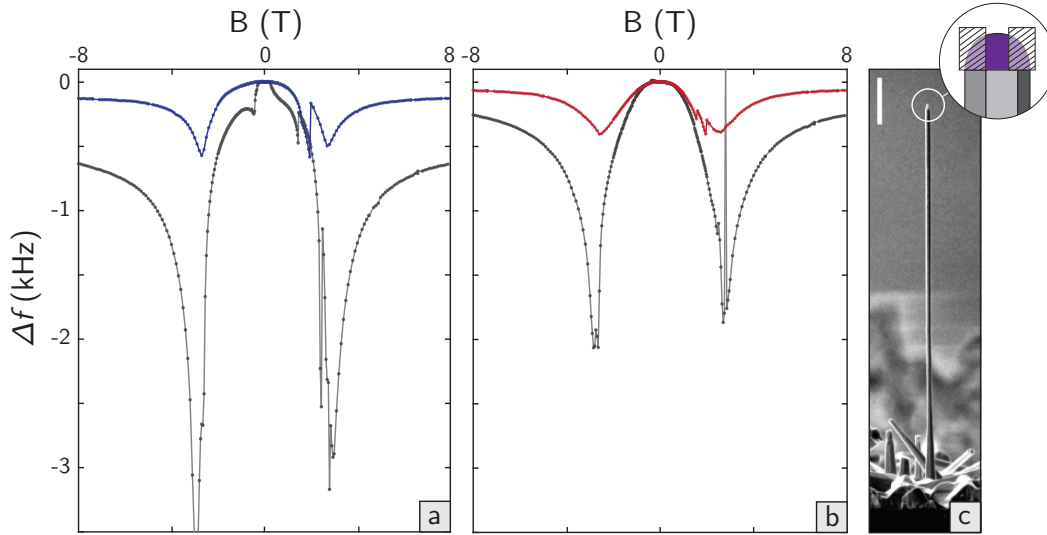


FIGURE F.1 | **Dynamic torque magnetometry of a FIBbed MnAs tip.**

First (a) and second (b) mode frequency shift as a function of the applied external magnetic field swept from -8 T to $+8$ T. The previous magnetometry results, measured for the as-grown MnAs tip, are plotted in gray for comparison. The first (second) mode's frequency $f_{0,1}$ ($f_{0,2}$) at zero field has been red shifted, as expected for a mass loss, from 693 kHz to 673 kHz (741 kHz to 725 kHz). The asymptotic frequency shift values are result reduced by 5 and 4 times, respectively. (c) SEM micrograph of the FIBbed NW. In the sketch are shown the two selected milling areas on the side of the tip. Scale bar 2 μm .

We plan to fully characterized the remanent state of such tips with micromagnetic simulations and to evaluate their sensing performance on calibration samples with known stray field and/or magnetization such as current micro-loops or thin magnetic multi-layer structures.

Appendix G

Room temperature NW MFM

The chosen test sample for these preliminary measurement are ferromagnetic permalloy (Py) disks, $1\ \mu\text{m}$ in diameter and $40\ \text{nm}$ thick, fabricated by Berezovsky's group at Case Western Reserve University, Cleveland. These structures are theoretically predicted to adopt a magnetic vortex configuration with a spot of perpendicular magnetization at the center of the vortex (i.e. vortex core). Experimental evidence for this magnetization spot has been provided by several techniques such as MFM [171] and magneto-optical Kerr effect (MOKE) microscopy [172]. The core magnetization singularity represents an interesting magnetic feature to be detected. A GaAs NW with MnAs tip is approached to the sample in Fig. G.1(a) at room temperature and zero external field, using a PLL to track the evolution of the first mode resonance frequency and a PID feedback loop to keep the oscillation amplitude constant ($r_1 = 5\ \text{nm}$), by controlling the driving voltage $V_{\text{drive},1}$ on the dither piezo. Due to the NW high sensitivity, the topography contribution given by the disks edge, superimposed to the magnetic contrast, is clearly visible at $200\ \text{nm}$ distance and shows the direction of oscillation of the first mode few degrees off the y -axis (Fig. G.1(b,c)). A refined scan of the first disk over a $1 \times 1\ \mu\text{m}^2$ window in Fig. G.1(d,e) shows radially disposed

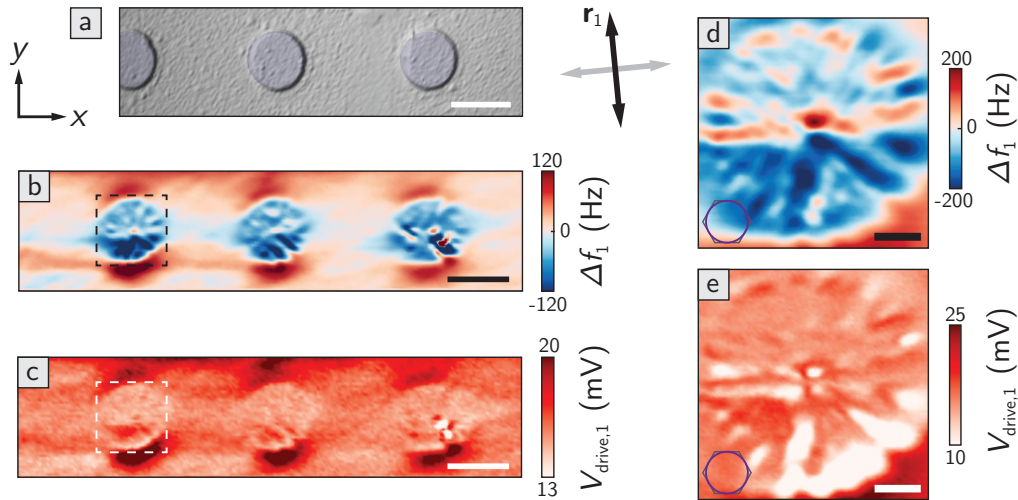


FIGURE G.1 | **Permalloy disks scanned with a magnetic-vortex tipped NW.** (a) Commercial AFM image of three permalloy disks (false colored), $1\ \mu\text{m}$ diameter and $40\ \text{nm}$ thick, on Au substrate. Scale bar $1\ \mu\text{m}$. (b,c) Frequency shift and dissipation scan, monitoring the first mode of oscillation. Tip-sample separation of $100\ \text{nm}$. Scale bar $1\ \mu\text{m}$. (d,e) Refined scan of the first disk (dashed lines contour in (b,c)) at tip-sample distance of $100\ \text{nm}$. The inset in the bottom left corners represent the NW tip physical extension. Scale bar $200\ \text{nm}$.

features on the disk edge, indicating a modulation of the stray field at the boundary with higher contrast for directions orthogonal to $\hat{\mathbf{r}}_1$. As expected, a double (due to the dipolar nature of compact magnetic tips) peak is measured in correspondence of the vortex core at the center of the disk, for both frequency and dissipation signals [171]. Most interestingly, the detected features present a much smaller width respect to the physical extension of the tip of ~ 230 nm; in particular, the disk's center core is resolved with a width of 75 nm. This spacial resolution enhancement can be explained by the significant reduction in net magnetic volume given by a MnAs tip in a vortex configuration by itself. We have confirmed this assumption by simulating the a full MFM scan scenario with the micromagnetics package *MuMax*³ (Fig. G.2(a)). At each point, is calculated the magnetic energy second derivative along the oscillation direction of a MnAs tip over a Py disk, in order to extract the frequency shift value with Eq. (4.5) (Fig. G.2(b)). Note that, for other NWs tips more commonly in a dipole-like remanent state the obtained space resolution is worse than for the magnetic vortex case.

Additional efforts have to be dedicated to the perform further experiments in this direction to improve interpretation of the data and verify the potential of such MFM imaging using a single magnetic vortex.

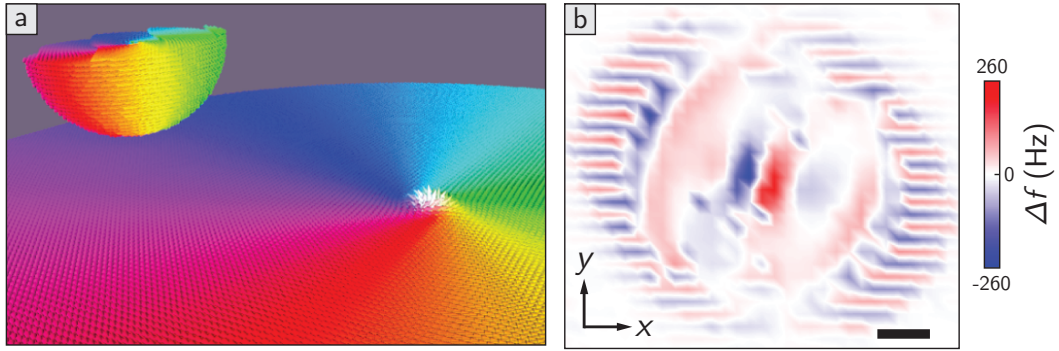


FIGURE G.2 | **Micromagnetic simulation of a MnAs tip over Py disk.**

(a) Schematic representation of the simulated problem. The planar orientation of the magnetization for each cell is color-coded over the full color spectrum. White cells indicate perpendicular magnetization (vortex core). (b) Frequency shift along x is derived through Eq. (4.5) by calculating the magnetic energy of a regular MnAs tip (parameters in Table 4.1), at 65 nm over the Py disk, with $\theta_K = 5^\circ$ and $\phi_K = 45^\circ$.

Bibliography

- [1] C. A. Coulomb et al. *Mémoires sur l'électricité et la magnétisme*. Mémoires de l'Académie Royale Des Sciences de Paris, 1789 cited in [viii](#)
- [2] Cavendish Henry. "XXI. Experiments to Determine the Density of the Earth", *Philosophical Transactions of the Royal Society of London* **88** (1798) . cited in [viii](#)
- [3] E. F. Nichols and G. F. Hull. "A Preliminary Communication on the Pressure of Heat and Light Radiation", *Physical Review (Series I)* **13**, 5 (1901) . cited in [viii](#)
- [4] G. Binnig, C. F. Quate, and C. Gerber. "Atomic Force Microscope", *Physical Review Letters* **56**, 9 (1986) . cited in [viii](#), [43](#)
- [5] F. J. Giessibl et al. "Subatomic Features on the Silicon (111)-(7x7) Surface Observed by Atomic Force Microscopy", *Science* **289**, 5478 (2000) . cited in [ix](#), [43](#)
- [6] L. Gross et al. "The Chemical Structure of a Molecule Resolved by Atomic Force Microscopy", *Science* **325**, 5944 (2009) . cited in [ix](#)
- [7] A. K. Naik et al. "Towards Single-Molecule Nanomechanical Mass Spectrometry", *Nature Nanotechnology* **4**, 7 (2009) . cited in [ix](#)
- [8] A. Mehlin et al. "Stabilized Skyrmion Phase Detected in MnSi Nanowires by Dynamic Cantilever Magnetometry", *Nano Letters* **15**, 7 (2015) . cited in [ix](#), [68](#), [69](#)
- [9] B. Gross et al. "Dynamic Cantilever Magnetometry of Individual CoFeB Nanotubes", *Physical Review B* **93**, 6 (2016) . cited in [ix](#), [68](#), [70](#)
- [10] A. C. Bleszynski-Jayich et al. "Persistent Currents in Normal Metal Rings", *Science* **326**, 5950 (2009) . cited in [ix](#), [68](#)
- [11] U. Gysin et al. "Low Temperature Ultrahigh Vacuum Noncontact Atomic Force Microscope in the Pendulum Geometry", *Review of Scientific Instruments* **82**, 2 (2011) . cited in [ix](#), [43](#)
- [12] M. Langer et al. "Giant Frictional Dissipation Peaks and Charge-Density-Wave Slips at the NbSe₂ Surface", *Nature Materials* **13**, 2 (2014) . cited in [ix](#)
- [13] D. Rugar et al. "Single Spin Detection by Magnetic Resonance Force Microscopy", *Nature* **430**, 6997 (2004) . cited in [ix](#), [31](#)
- [14] C. L. Degen et al. "Nanoscale Magnetic Resonance Imaging", *Proceedings of the National Academy of Sciences* **106**, 5 (2009) . cited in [ix](#), [62](#)
- [15] D. Rugar. "Improved Fiber-optic Interferometer for Atomic Force Microscopy", *Applied Physics Letters* **55**, 25 (1989) . cited in [ix](#), [31](#), [34](#)
- [16] H. J. Mamin and D. Rugar. "Sub-Attonewton Force Detection at Millikelvin Temperatures", *Applied Physics Letters* **79**, 20 (2001) . cited in [ix](#)
- [17] J. Moser et al. "Ultrasensitive Force Detection with a Nanotube Mechanical Resonator", *Nature Nanotechnology* **8**, 7 (2013) . cited in [ix](#), [31](#)

- [18] S. L. de Bonis et al. “Ultrasensitive Displacement Noise Measurement of Carbon Nanotube Mechanical Resonators”, *Nano Letters* **18**, 8 (2018) . cited in ix, 83
- [19] J. Chaste et al. “A Nanomechanical Mass Sensor with Yoctogram Resolution”, *Nature Nanotechnology* **7**, 5 (2012) . cited in ix
- [20] Y. Tao et al. “Permanent Reduction of Dissipation in Nanomechanical Si Resonators by Chemical Surface Protection”, *Nanotechnology* **26**, 46 (2015) . cited in ix, x, 8
- [21] M. H  ritier et al. “Nanoladder Cantilevers Made from Diamond and Silicon”, *Nano Letters* **18**, 3 (2018) . cited in x, 25
- [22] A. Gloppe et al. “Bidimensional Nano-Optomechanics and Topological Back-action in a Non-Conservative Radiation Force Field”, *Nature Nanotechnology* **9**, 11 (2014) . cited in x, xi, 9, 24, 27, 31, 41, 43, 48, 62
- [23] L. M. de L  pinay et al. “A Universal and Ultrasensitive Vectorial Nanomechanical Sensor for Imaging 2D Force Fields”, *Nature Nanotechnology* **12**, 2 (2017) . cited in x, xi, 31, 51, 62, 82
- [24] J. M. Nichol et al. “Displacement Detection of Silicon Nanowires by Polarization-Enhanced Fiber-Optic Interferometry”, *Applied Physics Letters* **93**, 19 (2008) . cited in x, 9, 22, 31, 34, 39, 43, 67, 83
- [25] N. Rossi et al. “Magnetic Force Sensing Using a Self-Assembled Nanowire”, *Nano Letters* **19**, 2 (2019) . cited in x, xi, 9, 61, 74
- [26] A. Tavernarakis et al. “Optomechanics with a Hybrid Carbon Nanotube Resonator”, *Nature Communications* **9**, 1 (2018) . cited in x, 9
- [27] B. C. Stipe et al. “Noncontact Friction and Force Fluctuations between Closely Spaced Bodies”, *Physical Review Letters* **87**, 9 (2001) . cited in x, 43, 52
- [28] S. Kuehn, R. F. Loring, and J. A. Marohn. “Dielectric Fluctuations and the Origins of Noncontact Friction”, *Physical Review Letters* **96**, 15 (2006) . cited in x, 52
- [29] J. M. Nichol et al. “Nanomechanical Detection of Nuclear Magnetic Resonance Using a Silicon Nanowire Oscillator”, *Physical Review B* **85**, 5 (2012) . cited in x, 43, 62, 83
- [30] F. R. Braakman and M. Poggio. “Force Sensing with Nanowire Cantilevers”, *Nanotechnology* (2019) . cited in xi
- [31] R. Garcia and E. T. Herruzo. “The Emergence of Multifrequency Force Microscopy”, *Nature Nanotechnology* **7**, 4 (2012) . cited in xi
- [32] E. Gil-Santos et al. “Nanomechanical Mass Sensing and Stiffness Spectrometry Based on Two-Dimensional Vibrations of Resonant Nanowires”, *Nature Nanotechnology* **5**, 9 (2010) . cited in xi, 9, 43
- [33] N. Rossi et al. “Vectorial Scanning Force Microscopy Using a Nanowire Sensor”, *Nature Nanotechnology* **12**, 2 (2017) . cited in xi, 9, 62, 82, 83
- [34] M. Montinaro. “Coupling of Nanomechanical Resonators to Controllable Quantum Systems”. Thesis. University_of_Basel, 2014 cited in xi, 35, 88
- [35] J. Hubmann et al. “Epitaxial Growth of Room-Temperature Ferromagnetic MnAs Segments on GaAs Nanowires via Sequential Crystallization”, *Nano Letters* **16**, 2 (2016) . cited in xi, 27, 63, 77
- [36] W. J. Bottega. *Engineering Vibrations*. 2 edition. Boca Raton: CRC Press, 2014 cited in 2, 4, 6

- [37] B. D. Hauer et al. “A General Procedure for Thermomechanical Calibration of Nano/Micro-Mechanical Resonators”, *Annals of Physics* **339** (2013) .
cited in 4, 7
- [38] L. Meirovitch. *Fundamentals of Vibrations*. Waveland Press, 2010
cited in 5
- [39] S. S. Rao. *Vibration of Continuous Systems*. John Wiley & Sons, 2019
cited in 5
- [40] A. N. Cleland and M. L. Roukes. “Noise Processes in Nanomechanical Resonators”, *Journal of Applied Physics* **92**, 5 (2002) .
cited in 7
- [41] M. Imboden and P. Mohanty. “Dissipation in Nanoelectromechanical Systems”, *Physics Reports* **534**, 3 (2014) .
cited in 7, 8
- [42] Y. Chen et al. “Effect of a High Density of Stacking Faults on the Young’s Modulus of GaAs Nanowires”, *Nano Letters* **16**, 3 (2016) .
cited in 8
- [43] K. Y. Yasumura et al. “Quality Factors in Micron- and Submicron-Thick Cantilevers”, *Journal of Microelectromechanical Systems* **9**, 1 (2000) .
cited in 8
- [44] J. M. Gere and B. J. Goodno. *Mechanics of Materials*. Cengage Learning, 2008
cited in 9
- [45] S. M. Tanner et al. “High-Q GaN Nanowire Resonators and Oscillators”, *Applied Physics Letters* **91**, 20 (2007) .
cited in 9, 31
- [46] M. Montinaro et al. “Quantum Dot Opto-Mechanics in a Fully Self-Assembled Nanowire”, *Nano Letters* **14**, 8 (2014) .
cited in 9
- [47] D. Cadeddu et al. “Time-Resolved Nonlinear Coupling between Orthogonal Flexural Modes of a Pristine GaAs Nanowire”, *Nano Letters* **16**, 2 (2016) .
cited in 9, 12
- [48] A. P. Foster et al. “Tuning Nonlinear Mechanical Mode Coupling in GaAs Nanowires Using Cross-Section Morphology Control”, *Nano Letters* **16**, 12 (2016) .
cited in 9, 12
- [49] S. Pairis et al. “Shot-Noise-Limited Nanomechanical Detection and Radiation Pressure Backaction from an Electron Beam”, *Physical Review Letters* **122**, 8 (2019) .
cited in 9
- [50] O. Malvar et al. “Tapered Silicon Nanowires for Enhanced Nanomechanical Sensing”, *Applied Physics Letters* **103**, 3 (2013) .
cited in 9
- [51] I. Tsioutsios et al. “Real-Time Measurement of Nanotube Resonator Fluctuations in an Electron Microscope”, *Nano Letters* **17**, 3 (2017) .
cited in 9, 31
- [52] W. A. Brantley. “Calculated Elastic Constants for Stress Problems Associated with Semiconductor Devices”, *Journal of Applied Physics* **44**, 1 (1973) .
cited in 10
- [53] T. B. Gabrielson. “Mechanical-Thermal Noise in Micromachined Acoustic and Vibration Sensors”, *IEEE Transactions on Electron Devices* **40**, 5 (1993) .
cited in 13
- [54] M. C. Wang and G. E. Uhlenbeck. “On the Theory of the Brownian Motion II”, *Reviews of Modern Physics* **17**, 2-3 (1945) .
cited in 13, 15
- [55] R. Kubo. “The Fluctuation-Dissipation Theorem”, *Reports on Progress in Physics* **29**, 1 (1966) .
cited in 13
- [56] M. Plancherel and M. Leffler. “Contribution À L’Étude de la représentation D’une fonction arbitraire par des intégrales définies”, *Rendiconti del Circolo Matematico di Palermo (1884-1940)* **30**, 1 (1910) .
cited in 14

- [57] M. V. Salapaka et al. “Multi-Mode Noise Analysis of Cantilevers for Scanning Probe Microscopy”, *Journal of Applied Physics* **81**, 6 (1997) . cited in 14
- [58] H. B. Callen and T. A. Welton. “Irreversibility and Generalized Noise”, *Physical Review* **83**, 1 (1951) . cited in 15
- [59] H. Nyquist. “Thermal Agitation of Electric Charge in Conductors”, *Physical Review* **32**, 1 (1928) . cited in 16
- [60] P. R. Saulson. “Thermal Noise in Mechanical Experiments”, *Physical Review D* **42**, 8 (1990) . cited in 16
- [61] M. Poot and H. S. J. van der Zant. “Mechanical Systems in the Quantum Regime”, *Physics Reports* **511**, 5 (2012) . cited in 17
- [62] M. Poggio et al. “Feedback Cooling of a Cantilever’s Fundamental Mode below 5 mK”, *Physical Review Letters* **99**, 1 (2007) . cited in 17
- [63] M. Aspelmeyer, T. J. Kippenberg, and F. Marquardt. “Cavity Optomechanics”, *Reviews of Modern Physics* **86**, 4 (2014) . cited in 17
- [64] P. R. Wiecha et al. “Strongly Directional Scattering from Dielectric Nanowires”, *ACS Photonics* **4**, 8 (2017) . cited in 18, 19
- [65] D. Ramos et al. “Silicon Nanowires: Where Mechanics and Optics Meet at the Nanoscale”, *Scientific Reports* **3** (2013) . cited in 18
- [66] L. Cao et al. “Engineering Light Absorption in Semiconductor Nanowire Devices”, *Nature Materials* **8**, 8 (2009) . cited in 18
- [67] G. Pavlovic, G. Malpuech, and N. A. Gippius. “Dispersion and Polarization Conversion of Whispering Gallery Modes in Nanowires”, *Physical Review B* **82**, 19 (2010) . cited in 19
- [68] T. Rother, S. Havemann, and K. Schmidt. “Scattering of Plane Waves on Finite Cylinders with Non-Circular Cross-Sections”, *Progress In Electromagnetics Research* **23** (1999) . cited in 19
- [69] C. F. Bohren and D. R. Huffman. *Absorption and Scattering of Light by Small Particles*. John Wiley & Sons, 2008 cited in 19–22
- [70] S. Adachi. “Optical Dispersion Relations for GaP, GaAs, GaSb, InP, InAs, InSb, Al_xGa_{1-x}As, and In_{1-x}Ga_xAs_yP_{1-y}”, *Journal of Applied Physics* **66**, 12 (1989) . cited in 24
- [71] B. Sanii and P. D. Ashby. “High Sensitivity Deflection Detection of Nanowires”, *Physical Review Letters* **104**, 14 (2010) . cited in 24, 31, 34, 61
- [72] Y. Tao et al. “Single-Crystal Diamond Nanomechanical Resonators with Quality Factors Exceeding One Million”, *Nature Communications* **5** (2014) . cited in 25
- [73] R. S. Wagner and W. C. Ellis. “Vapor-liquid-solid Mechanism of Single Crystal Growth”, *Applied Physics Letters* **4**, 5 (1964) . cited in 25
- [74] C. Colombo et al. “Ga-Assisted Catalyst-Free Growth Mechanism of GaAs Nanowires by Molecular Beam Epitaxy”, *Physical Review B* **77**, 15 (2008) . cited in 26, 63
- [75] W. Kim et al. “Bistability of Contact Angle and Its Role in Achieving Quantum-Thin Self-Assisted GaAs Nanowires”, *Nano Letters* **18**, 1 (2018) . cited in 27, 61, 81

- [76] G. Meyer and N. M. Amer. “Novel Optical Approach to Atomic Force Microscopy”, *Applied Physics Letters* **53**, 12 (1988) . cited in 31
- [77] K. Karrai and R. D. Grober. “Piezoelectric Tip-sample Distance Control for near Field Optical Microscopes”, *Applied Physics Letters* **66**, 14 (1995) . cited in 31
- [78] F. J. Giessibl. “High-Speed Force Sensor for Force Microscopy and Profilometry Utilizing a Quartz Tuning Fork”, *Applied Physics Letters* **73**, 26 (1998) . cited in 31
- [79] C. A. Regal, J. D. Teufel, and K. W. Lehnert. “Measuring Nanomechanical Motion with a Microwave Cavity Interferometer”, *Nature Physics* **4**, 7 (2008) . cited in 31
- [80] T. Faust et al. “Microwave Cavity-Enhanced Transduction for Plug and Play Nanomechanics at Room Temperature”, *Nature Communications* **3** (2012) . cited in 31
- [81] V. Sazonova et al. “A Tunable Carbon Nanotube Electromechanical Oscillator”, *Nature* **431**, 7006 (2004) . cited in 31, 43
- [82] A. Niguès, A. Siria, and P. Verlot. “Dynamical Backaction Cooling with Free Electrons”, *Nature Communications* **6** (2015) . cited in 31
- [83] A. Högele et al. “Fiber-Based Confocal Microscope for Cryogenic Spectroscopy”, *Review of Scientific Instruments* **79**, 2 (2008) . cited in 32
- [84] L. Novotny and B. Hecht. *Principles of Nano-Optics*. Cambridge University Press, 2006 cited in 33
- [85] D. Rugar et al. “Force Microscope Using a Fiber-optic Displacement Sensor”, *Review of Scientific Instruments* **59**, 11 (1988) . cited in 34
- [86] S. Kozaki. “Scattering of a Gaussian Beam by a Homogeneous Dielectric Cylinder”, *Journal of Applied Physics* **53**, 11 (1982) . cited in 34
- [87] L. M. de Lépinay et al. “Eigenmode Orthogonality Breaking and Anomalous Dynamics in Multimode Nano-Optomechanical Systems under Non-Reciprocal Coupling”, *Nature Communications* **9**, 1 (2018) . cited in 41, 51
- [88] F. Fogliano et al. “Cavity Nano-Optomechanics in the Ultrastrong Coupling Regime with Ultrasensitive Force Sensors”, *arXiv:1904.01140 [quant-ph]* (2019). cited in 41
- [89] F. J. Giessibl. “Advances in Atomic Force Microscopy”, *Reviews of Modern Physics* **75**, 3 (2003) . cited in 43
- [90] F. J. Giessibl. “Atomic Resolution of the Silicon (111)-(7x7) Surface by Atomic Force Microscopy”, *Science* **267**, 5194 (1995) . cited in 43
- [91] M. Poggio. “Nanomechanics: Sensing from the Bottom Up”, *Nature Nanotechnology* **8**, 7 (2013) . cited in 43
- [92] J. S. Bunch et al. “Electromechanical Resonators from Graphene Sheets”, *Science* **315**, 5811 (2007) . cited in 43
- [93] S. Perisanu et al. “High Q Factor for Mechanical Resonances of Batch-Fabricated SiC Nanowires”, *Applied Physics Letters* **90**, 4 (2007) . cited in 43
- [94] M. Li et al. “Bottom-up Assembly of Large-Area Nanowire Resonator Arrays”, *Nature Nanotechnology* **3**, 2 (2008) . cited in 43

- [95] M. Belov et al. “Mechanical Resonance of Clamped Silicon Nanowires Measured by Optical Interferometry”, *Journal of Applied Physics* **103**, 7 (2008) .
cited in 43
- [96] J. M. Nichol. “Nanoscale Magnetic Resonance Imaging Using Silicon Nanowire”. PhD thesis. Urbana-Champaign: University_of_Illinois, 2013
cited in 43
- [97] M. Nonnenmacher, M. P. O’Boyle, and H. K. Wickramasinghe. “Kelvin Probe Force Microscopy”, *Applied Physics Letters* **58**, 25 (1991) .
cited in 43, 61
- [98] O. Pfeiffer et al. “Lateral-Force Measurements in Dynamic Force Microscopy”, *Physical Review B* **65**, 16 (2002) .
cited in 43, 52
- [99] F. J. Giessibl, M. Herz, and J. Mannhart. “Friction Traced to the Single Atom”, *Proceedings of the National Academy of Sciences* **99**, 19 (2002) .
cited in 43
- [100] S. Kawai et al. “Dynamic Lateral Force Microscopy with True Atomic Resolution”, *Applied Physics Letters* **87**, 17 (2005) .
cited in 43
- [101] S. Kawai, N. Sasaki, and H. Kawakatsu. “Direct Mapping of the Lateral Force Gradient on Si(111)-7x7”, *Physical Review B* **79**, 19 (2009) .
cited in 43
- [102] S. Kawai et al. “Ultrasensitive Detection of Lateral Atomic-Scale Interactions on Graphite (0001) via Bimodal Dynamic Force Measurements”, *Physical Review B* **81**, 8 (2010) .
cited in 43, 61
- [103] E. Uccelli et al. “Three-Dimensional Multiple-Order Twinning of Self-Catalyzed GaAs Nanowires on Si Substrates”, *Nano Letters* **11**, 9 (2011) .
cited in 44
- [104] E. Russo-Averchi et al. “Suppression of Three Dimensional Twinning for a 100% Yield of Vertical GaAs Nanowires on Silicon”, *Nanoscale* **4**, 5 (2012) .
cited in 44
- [105] M. Heigoldt et al. “Long Range Epitaxial Growth of Prismatic Heterostructures on the Facets of Catalyst-Free GaAs Nanowires”, *Journal of Materials Chemistry* **19**, 7 (2009) .
cited in 44
- [106] T. R. Albrecht et al. “Frequency Modulation Detection Using High-Q Cantilevers for Enhanced Force Microscope Sensitivity”, *Journal of Applied Physics* **69**, 2 (1991) .
cited in 46
- [107] T. Faust et al. “Nonadiabatic Dynamics of Two Strongly Coupled Nanomechanical Resonator Modes”, *Physical Review Letters* **109**, 3 (2012) .
cited in 48, 57
- [108] F. J. Giessibl. “A Direct Method to Calculate Tip–Sample Forces from Frequency Shifts in Frequency-Modulation Atomic Force Microscopy”, *Applied Physics Letters* **78**, 1 (2000) .
cited in 53
- [109] J. Rieger et al. “Frequency and Q Factor Control of Nanomechanical Resonators”, *Applied Physics Letters* **101**, 10 (2012) .
cited in 55, 59
- [110] T. Faust et al. “Coherent Control of a Classical Nanomechanical Two-Level System”, *Nature Physics* **9**, 8 (2013) .
cited in 57
- [111] H. Okamoto et al. “Coherent Phonon Manipulation in Coupled Mechanical Resonators”, *Nature Physics* **9**, 8 (2013) .
cited in 57
- [112] I. I. Rabi. “Space Quantization in a Gyating Magnetic Field”, *Physical Review* **51**, 8 (1937) .
cited in 57
- [113] M. J. Seitner et al. “Classical Stückelberg Interferometry of a Nanomechanical Two-Mode System”, *Physical Review B* **94**, 24 (2016) .
cited in 57

- [114] B. H. Schneider et al. “Observation of Decoherence in a Carbon Nanotube Mechanical Resonator”, *Nature Communications* **5** (2014) . cited in 57
- [115] L. Novotny. “Strong Coupling, Energy Splitting, and Level Crossings: A Classical Perspective”, *American Journal of Physics* **78**, 11 (2010) . cited in 57
- [116] F. R. Braakman et al. “Coherent Two-Mode Dynamics of a Nanowire Force Sensor”, *Physical Review Applied* **9**, 5 (2018) . cited in 58
- [117] M. Frimmer and L. Novotny. “The Classical Bloch Equations”, *American Journal of Physics* **82**, 10 (2014) . cited in 59
- [118] R. J. C. Spreeuw et al. “Classical Realization of a Strongly Driven Two-Level System”, *Physical Review Letters* **65**, 21 (1990) . cited in 61
- [119] G. D. Fuchs et al. “Gigahertz Dynamics of a Strongly Driven Single Quantum Spin”, *Science* **326**, 5959 (2009) . cited in 61
- [120] K. R. K. Rao and D. Suter. “Nonlinear Dynamics of a Two-Level System of a Single Spin Driven beyond the Rotating-Wave Approximation”, *Physical Review A* **95**, 5 (2017) . cited in 61
- [121] J. E. Stern et al. “Deposition and Imaging of Localized Charge on Insulator Surfaces Using a Force Microscope”, *Applied Physics Letters* **53**, 26 (1988) . cited in 61
- [122] C. Schönenberger and S. F. Alvarado. “Observation of Single Charge Carriers by Force Microscopy”, *Physical Review Letters* **65**, 25 (1990) . cited in 61
- [123] I. Schmid et al. “Exchange Bias and Domain Evolution at 10 Nm Scales”, *Physical Review Letters* **105**, 19 (2010) . cited in 62
- [124] Z. Deng et al. “Metal-Coated Carbon Nanotube Tips for Magnetic Force Microscopy”, *Applied Physics Letters* **85**, 25 (2004) . cited in 62
- [125] A. Winkler et al. “Magnetic Force Microscopy Sensors Using Iron-Filled Carbon Nanotubes”, *Journal of Applied Physics* **99**, 10 (2006) . cited in 62
- [126] F. Wolny et al. “Iron Filled Carbon Nanotubes as Novel Monopole-like Sensors for Quantitative Magnetic Force Microscopy”, *Nanotechnology* **21**, 43 (2010) . cited in 62
- [127] Y. Lisunova et al. “Optimal Ferromagnetically-Coated Carbon Nanotube Tips for Ultra-High Resolution Magnetic Force Microscopy”, *Nanotechnology* **24**, 10 (2013) . cited in 62
- [128] L. Rondin et al. “Stray-Field Imaging of Magnetic Vortices with a Single Diamond Spin”, *Nature Communications* **4** (2013) . cited in 62
- [129] J.-P. Tetienne et al. “Nanoscale Imaging and Control of Domain-Wall Hopping with a Nitrogen-Vacancy Center Microscope”, *Science* **344**, 6190 (2014) . cited in 62
- [130] J.-P. Tetienne et al. “The Nature of Domain Walls in Ultrathin Ferromagnets Revealed by Scanning Nanomagnetometry”, *Nature Communications* **6** (2015) . cited in 62
- [131] Y. Dovzhenko et al. “Imaging the Spin Texture of a Skyrmion Under Ambient Conditions Using an Atomic-Sized Sensor”, *arXiv:1611.00673 [cond-mat]* (2016). cited in 62
- [132] L. Thiel et al. “Quantitative Nanoscale Vortex Imaging Using a Cryogenic Quantum Magnetometer”, *Nature Nanotechnology* **11**, 8 (2016) . cited in 62

- [133] M. Pelliccione et al. “Scanned Probe Imaging of Nanoscale Magnetism at Cryogenic Temperatures with a Single-Spin Quantum Sensor”, *Nature Nanotechnology* **11**, 8 (2016) . cited in 62
- [134] J.-P. Tetienne et al. “Quantum Imaging of Current Flow in Graphene”, *Science Advances* **3**, 4 (2017) . cited in 62
- [135] D. Rugar et al. “Proton Magnetic Resonance Imaging Using a Nitrogen–Vacancy Spin Sensor”, *Nature Nanotechnology* **10**, 2 (2015) . cited in 62
- [136] T. Häberle et al. “Nanoscale Nuclear Magnetic Imaging with Chemical Contrast”, *Nature Nanotechnology* **10**, 2 (2015) . cited in 62
- [137] M. Poggio and C. L. Degen. “Force-Detected Nuclear Magnetic Resonance: Recent Advances and Future Challenges”, *Nanotechnology* **21**, 34 (2010) . cited in 62
- [138] A. Siria and A. Niguès. “Electron Beam Detection of a Nanotube Scanning Force Microscope”, *Scientific Reports* **7**, 1 (2017) . cited in 62
- [139] J. Hubmann. “GaAs Nanowires: Epitaxy, Crystal Structure-Related Properties and Magnetic Heterostructures”. Phd. 2016 cited in 64
- [140] F. Heusler. “Über Manganbronze Und Über Die Synthese Magnetisierbarer Legierungen Aus Unmagnetischen Metallen”, *Angewandte Chemie* **17**, 9 (1904) . cited in 63
- [141] S. Hilpert and T. Dieckmann. “Über Arsenide. I. (Eisen- Und Manganarsenide.)”, *Berichte der deutschen chemischen Gesellschaft* **44**, 3 (1911) . cited in 63
- [142] B. Jenichen et al. “Structural and Magnetic Phase Transition in MnAs(0001) / GaAs(111) Epitaxial Films”, *Physical Review B* **68**, 13 (2003) . cited in 64
- [143] R. Engel-Herbert et al. “Micromagnetic Properties of MnAs(0001)/GaAs(111) Epitaxial Films”, *Applied Physics Letters* **88**, 5 (2006) . cited in 64, 65
- [144] M. Tanaka. “Ferromagnet (MnAs)/III V Semiconductor Hybrid Structures”, *Semiconductor Science and Technology* **17**, 4 (2002) . cited in 64
- [145] M. Kästner, L. Däweritz, and K. H. Ploog. “Surface Reconstruction, Screw Dislocations and Anisotropic Step Flow Growth of MnAs on GaAs(111)B Substrates”, *Surface Science* **511**, 1 (2002) . cited in 64, 65
- [146] D. H. Mosca, F. Vidal, and V. H. Etgens. “Strain Engineering of the Magnetocaloric Effect in MnAs Epilayers”, *Physical Review Letters* **101**, 12 (2008) . cited in 65
- [147] R. W. De Blois and D. S. Rodbell. “Magnetic First-Order Phase Transition in Single-Crystal MnAs”, *Physical Review* **130**, 4 (1963) . cited in 65, 70
- [148] Y. Burenkov et al. “Temperature Dependences of the Elastic Constants of Gallium Arsenide”, *Sov. Phys. Solid State* **15**, 6 (1973). cited in 67
- [149] B. C. Stipe et al. “Magnetic Dissipation and Fluctuations in Individual Nanomagnets Measured by Ultrasensitive Cantilever Magnetometry”, *Physical Review Letters* **86**, 13 (2001) . cited in 68, 70
- [150] D. P. Weber et al. “Cantilever Magnetometry of Individual Ni Nanotubes”, *Nano Letters* **12**, 12 (2012) . cited in 68, 70
- [151] A. Buchter et al. “Reversal Mechanism of an Individual Ni Nanotube Simultaneously Studied by Torque and SQUID Magnetometry”, *Physical Review Letters* **111**, 6 (2013) . cited in 68

- [152] J. Jang, R. Budakian, and Y. Maeno. “Phase-Locked Cantilever Magnetometry”, *Applied Physics Letters* **98**, 13 (2011) . cited in 68
- [153] T. Fischbacher et al. “A Systematic Approach to Multiphysics Extensions of Finite-Element-Based Micromagnetic Simulations: Nmag”, *IEEE Transactions on Magnetics* **43**, 6 (2007) . cited in 71
- [154] A. Vansteenkiste et al. “The Design and Verification of MuMax3”, *AIP Advances* **4**, 10 (2014) . cited in 71
- [155] D. G. Ramlan et al. “Ferromagnetic Self-Assembled Quantum Dots on Semiconductor Nanowires”, *Nano Letters* **6**, 1 (2006) . cited in 77
- [156] K. Kabamoto, R. Kodaira, and S. Hara. “Magnetization in Vertical MnAs/InAs Heterojunction Nanowires”, *Journal of Crystal Growth* **464**, Supplement C (2017) . cited in 77
- [157] J. Lohau et al. “Quantitative Determination of Effective Dipole and Monopole Moments of Magnetic Force Microscopy Tips”, *Journal of Applied Physics* **86**, 6 (1999) . cited in 77
- [158] T. Kebe and A. Carl. “Calibration of Magnetic Force Microscopy Tips by Using Nanoscale Current-Carrying Parallel Wires”, *Journal of Applied Physics* **95**, 3 (2004) . cited in 77
- [159] C. Schönenberger and S. F. Alvarado. “Understanding Magnetic Force Microscopy”, *Zeitschrift für Physik B Condensed Matter* **80**, 3 (1990) . cited in 79, 84
- [160] H. J. Hug et al. “Quantitative Magnetic Force Microscopy on Perpendicularly Magnetized Samples”, *Journal of Applied Physics* **83**, 11 (1998) . cited in 79
- [161] P. J. A. van Schendel et al. “A Method for the Calibration of Magnetic Force Microscopy Tips”, *Journal of Applied Physics* **88**, 1 (2000) . cited in 79
- [162] J. R. Kirtley. “Fundamental Studies of Superconductors Using Scanning Magnetic Imaging”, *Reports on Progress in Physics* **73**, 12 (2010) . cited in 81, 84, 93
- [163] K. Chang et al. “Nanoscale Imaging of Current Density with a Single-Spin Magnetometer”, *Nano Letters* **17**, 4 (2017) . cited in 81
- [164] J. Pablo-Navarro et al. “Tuning Shape, Composition and Magnetization of 3D Cobalt Nanowires Grown by Focused Electron Beam Induced Deposition (FEVID)”, *Journal of Physics D: Applied Physics* **50**, 18 (2017) . cited in 81, 85
- [165] A. Kaidatzis and J. M. García-Martín. “Torsional Resonance Mode Magnetic Force Microscopy: Enabling Higher Lateral Resolution Magnetic Imaging without Topography-Related Effects”, *Nanotechnology* **24**, 16 (2013) . cited in 81
- [166] P. Grütter et al. “Magnetic Dissipation Force Microscopy”, *Applied Physics Letters* **71**, 2 (1997) . cited in 82
- [167] P. Treutlein et al. “Hybrid Mechanical Systems”. In: *Cavity Optomechanics: Nano- and Micromechanical Resonators Interacting with Light*. Ed. by M. Aspelmeyer, T. J. Kippenberg, and F. Marquardt. Berlin, Heidelberg: Springer Berlin Heidelberg, 2014 cited in 83
- [168] P. J. A. van Schendel et al. “A Method for the Calibration of Magnetic Force Microscopy Tips”, *Journal of Applied Physics* **88**, 1 (2000) . cited in 84

- [169] J. Pablo-Navarro, C. Magén, and J. M. de Teresa. “Purified and Crystalline Three-Dimensional Electron-Beam-Induced Deposits: The Successful Case of Cobalt for High-Performance Magnetic Nanowires”, *ACS Applied Nano Materials* **1**, 1 (2018) . cited in 85
- [170] M. Poggio and B. E. Herzog. “Force-Detected Nuclear Magnetic Resonance”. In: *Micro and Nano Scale NMR*. Wiley-Blackwell, 2018 cited in 93
- [171] T. Shinjo et al. “Magnetic Vortex Core Observation in Circular Dots of Permalloy”, *Science* **289**, 5481 (2000) . cited in 98, 99
- [172] R. Badea, J. A. Frey, and J. Berezovsky. “Magneto-Optical Imaging of Vortex Domain Deformation in Pinning Sites”, *Journal of Magnetism and Magnetic Materials* **381** (2015) . cited in 98

Nicola Rossi | Curriculum Vitæ

Department of Physics - Klingelbergstrasse 82 – 4056 Basel – Switzerland

✉ nicola.rossi@unibas.ch

Education

University of Basel

PhD in Experimental Physics

2014–2019

- Thesis title: *Force sensing with nanowires*
- Advisor: Prof. M. Poggio

University of Genoa

M.Sc. in Electronic Engineering

2010–2013

- Thesis title: *Modelling improvements in an embedded control system for LHC collimators at CERN*
- Advisor: Prof. M. Storace, Ing. Dr. A. Masi

University of Genoa

B.Sc. in Electronic Engineering

2007–2010

- Thesis title: *Development and testing of a software package for non-linear dynamical systems analysis*
- Advisor: Prof. M. Storace

Publications

“Magnetic Force Sensing Using a Self-Assembled Nanowire”,
N. Rossi, B. Gross, F. Dirnberger, D. Bougeard, and M. Poggio
in: *Nano Letters* 19.2 (2019).

“Imaging pinning and expulsion of individual superconducting vortices in amorphous MoSi thin films”,
L. Ceccarelli, D. Vasyukov, M. Wyss, G. Romagnoli, N. Rossi, L. Moser, and M. Poggio
in: *Physical Review B* 100.10 (2019).

“Coherent Two-Mode Dynamics of a Nanowire Force Sensor”,
F. R. Braakman, N. Rossi, G. Tütüncüoglu, A. Fontcuberta i Morral, and M. Poggio
in: *Physical Review Applied* 9.5 (2018).

“Imaging Stray Magnetic Field of Individual Ferromagnetic Nanotubes”,
D. Vasyukov, L. Ceccarelli, M. Wyss, B. Gross, A. Schwarb, A. Mehlin, N. Rossi, G. Tütüncüoglu, F. Heimbach, R. R. Zamani, A. Kovács, A. Fontcuberta i Morral, D. Grundler, and M. Poggio
in: *Nano Letters* 18.2 (2018).

“Vectorial scanning force microscopy using a nanowire sensor”,
N. Rossi, F. R. Braakman, D. Cadeddu, D. Vasyukov, G. Tütüncüoglu, A. Fontcuberta i Morral, and M. Poggio
in: *Nature Nanotechnology* 12.2 (2017).

“Electric-Field Sensing with a Scanning Fiber-Coupled Quantum Dot”,
D. Cadeddu, M. Munsch, N. Rossi, J. Gérard, J. Claudon, R. Warburton, and M. Poggio
in: *Physical Review Applied* 8.3 (2017).

Presentations

APS March Meeting, Boston, USA

March 2019

Magnetic force sensing using a self-assembled GaAs nanowire with a MnAs tip (Oral)

Spintech IX, Fukuoka, Japan

June 2017

Torque magnetometry of individual GaAs nanowires with ferromagnetic MnAs tips (Oral)

Frontiers of Nanomechanical Systems, La Thuille, Italy

February 2017

Vectorial scanning force microscopy using a nanowire sensor (Poster)

Workshop on Nanomechanical Sensing, Delft, The Netherlands

June 2016

Vectorial scanning force microscopy using a nanowire mechanical resonator (Oral)

Acknowledgements

The work presented in this thesis, not only summarizes the scientific outcome of my PhD project, but it also represents the result of a collective effort in which many collaborators took part during all these years, and that now I have the chance to acknowledge.

In the first place, the most fundamental thanks goes to Martino Poggio, who gave an engineer the opportunity to explore the world of experimental physics. His insightful and deep physical intuition, determination and motivation guided me through all difficulties and challenges, being my constant source of inspiration.

Thanks to Prof. Adrian Bachtold for promptly accepting to be part of my defense committee, dedicating time to the evaluation of this work.

A needful acknowledgment goes to our external collaborators, which grew the nanowires samples at the heart of our experiments. Namely, the group of Prof. Anna Fontcuberta i Morral at EPFL, Lausanne and the group of Prof. Dominique Bougeard at the University of Regensburg.

In equal measure, none of these experiments would have taken place without the amazing support of our in-house mechanical and electronic workshop. In particular, a special thanks goes to Sascha Martin for his careful and patient correction of sloppy - or even unrealistic - CAD designs.

Coming to the PoggioLab members, a special mention goes to Denis Vasyukov, who backed me up in the first months of my PhD, giving me a broadband ‘no-frills’ introduction to all possible technical aspects of a physics laboratory’s everyday life.

Starting from the elders, thanks to Michele and Dennis for welcoming me to the lab - without notice - on a random Saturday of quite some years ago. Thanks Arne for enabling dark humor in the group and letting me use his postbox at the German border for records smuggling. Thanks Ben for sharing Metropol Kurier facilities for some critical sofa-moving business. Thanks Andrea for keeping in check the entropy rate in our lab (and the water pressure) and taking over all the bureaucratic issues with great sense of responsibility.

Thanks to Dr. Floris and Dr. Boris for helping me navigate my way through the experimental results with their scientific insights and precious numerical simulations. Thanks to Marcus, my passepartout for the Basler outer world: from the provision of Muttentzerkurve tickets, to delicate negotiations with the local natives, led with impeccable diplomatic skills.

A premium dedication goes to Davide, I had the great pleasure to work together with and with whom I also shared - sadly for him - most of the pain, joy and concerns of these PhD years, condensed in an everflowing stream of complaints. Getting to fresher newcomers, thanks to Lorenzo for his unrivaled listening skills and our endless discussions about whatever - among them also some scientific ones. Thanks to our sportsman Giulio for boosting my motivation for wintry early morning bike rides and for being always up to watch every single sport event.

Furthermore, I want to sincerely thank all the other colleagues who joined the group, for the enjoyable time spent together, which greatly enriched my PhD experience. Namely, my thanks go to Thibaud, Panos, Simon, David, Estefani and, in

particular, to Hinrich, who joined our research on nanowire sensors bringing scientific enthusiasm and some proper Python scripting.

More in general, during these year at University of Basel, I had the fortune of crossing paths with several special people. Among them, I want to mention Claudia, Marta, the menino prodígio Alex and the source of unconventional life visions Ehud.

Outside university, the bike rides with the Kleinhüningen Ghetto Boys | KGB club members have provided great fun and important help for mental stability, in particular the crazy ones with my good friend Bruno.

Outside Switzerland, I am truly grateful to all my friends which constantly support and inspire me. Big thanks to my old friend Davide, for the great moments shared together despite him changing country every two years. Thanks to Fabrizio for his last minute advice on optics, and for his empathy and willingness to share our occasional bitterness about PhD life. Thanks to Salvatore, Riccardo and Rosario to keep the Geneva core together even after we parted ways.

Going back to Liguria every now and then, thanks to my friends who always made me feel home; specially to Michele and Emanuela, for making sure I did not lose contact with local traditions and life style. Thanks to Olmo for always finding some time - despite him being a popstar - for listening to some dusty records together, sipping chamomile tea in Barletti Alley.

A distinct mention goes to my artisan of reference Paolo, for giving me the opportunity to tackle ‘real life’ technical problems not covered by textbooks, while taking the first steps in the (home-made) world of scanning probe microscopy.

In conclusion, but above everything, I want to acknowledge with unconditional gratitude Χριστίνα, for being on my side every day with love and infinite patience, and my parents, for really making all this possible with their constant support and wise advice.